

TEST OF BOUND STATE QED  
HIGHER ORDER CORRECTION :  
PRECISION MEASUREMENT OF  
ORTHOPOSITRONIUM DECAY RATE

PH. D. THESIS

Yousuke Kataoka

March 2007

Department of Physics  
Faculty of Science, University of Tokyo

---

## Abstract

This thesis reports a new measurement of the ortho-positronium decay rate  $\lambda_{o\text{-Ps}}$ . The improvements of the setup and the analytic techniques solve the crucial systematic errors previously suffered. The obtained result is  $\lambda_{o\text{-Ps}} = 7.0401 \pm 0.0006(\text{stat.})_{-0.0009}^{+0.0007}(\text{sys.}) \mu\text{s}^{-1}$ , where the first error is the statistical error, and the second represents the systematic error.

The measured value is consistent with the theoretical QED prediction and the recent measurements from 1995. In addition, the world average of the decay rate favors the  $O(\alpha^2)$ -corrected QED prediction rather than that of  $O(\alpha)$  correction.

# Acknowledgements

First, I would like to express my gratitude to Prof. Tomio Kobayashi (ICEPP Univ. of Tokyo) for providing me with this work. Without his continuous encouragement and supports, I could not have finished this study. I also wish to express my great appreciation to Shoji Asai (ICEPP Univ. of Tokyo) for his continuous assistance and guidance at this work. He is my collaborator in this experiment and heads a series of lifetime experiment from 1995. I would like to thank Osamu Jinnouchi (KEK) for many useful information and suggestions. This work bases on his previous measurement in 2001. I would also like to thank Toshio Namba (ICEPP Univ. of Tokyo) for his usefull suggestions and supports. I would like to thank all the students of our group, Mitiru Kaneda, Genta Koreki, Keiji Kishimoto, Kazuyuki Nishihara, Yusuke Tomishima. Sincere gratitude is expressed to Tetsuro Mashimo and Junichi Tanaka. They construct and maintain the computing system used in this analysis. I gratefully acknowledge Nippon Aerosil Ltd. for the generous supply of the silica powders and their valuable information. I would like to thank all the staffs and students of International Center for Elementary Particle Physics (ICEPP) at University of Tokyo,

# Contents

<b>Acknowledgements</b>	<b>ii</b>
<b>1 Introduction</b>	<b>1</b>
1.1 Properties of Positronium . . . . .	1
1.2 Theoretical Predictions of Orthopositronium Decay Rate . . .	2
1.2.1 The Lowest Order Decay Width . . . . .	3
1.2.2 The $O(\alpha)$ Correction . . . . .	3
1.2.3 $\alpha^2 \ln(\alpha^{-1})$ , $\alpha^3 \ln^2(\alpha^{-1})$ , $\alpha^3 \ln(\alpha^{-1})$ Contributions . .	3
1.2.4 $O(\alpha^2)$ Correction . . . . .	4
1.2.5 Summary of the QED Prediction . . . . .	5
1.3 Previous Measurements of Orthopositronium Decay Rate . .	5
1.3.1 Techniques of the Measurement . . . . .	6
1.3.2 History of the Measurement . . . . .	7
<b>2 Experiment</b>	<b>10</b>
2.1 Method of the Experiment . . . . .	10
2.1.1 Pick-off Annihilation . . . . .	10
2.1.2 Previous Extrapolation Method . . . . .	10
2.1.3 Direct Measurement of the Pick-off Rate . . . . .	11
2.1.4 Measurements in 1995 and 2001 . . . . .	13
2.2 New Features of the Present Measurement . . . . .	14
2.2.1 Introduction of Fast Inorganic Scintillator . . . . .	14
2.2.2 New Design of Ps Formation Assembly . . . . .	16
2.2.3 Geant4 Simulation and its Validation . . . . .	16
2.3 Description of Apparatus . . . . .	17
2.3.1 Positronium Formation Assembly . . . . .	17
2.3.2 Characteristics of SiO <sub>2</sub> Powders . . . . .	21
2.3.3 Detectors . . . . .	22
2.3.4 Timing system . . . . .	23
2.3.5 Electronics . . . . .	29
2.3.6 The CAMAC Data Acquisition System . . . . .	37
2.4 Monte Carlo Simulation . . . . .	38
2.4.1 Positron and Photon Simulation . . . . .	38

2.4.2	Response Function of the Ge Detector . . . . .	40
2.4.3	Response Function of the YAP Scintillator . . . . .	40
<b>3</b>	<b>Analysis</b>	<b>47</b>
3.1	Calibration and Time Walk Correction . . . . .	47
3.1.1	Data Sets . . . . .	47
3.1.2	Time and Energy Spectrum of the $\gamma$ -ray Detector . . . . .	48
3.1.3	Calibration . . . . .	49
3.1.4	Event Selection . . . . .	52
3.1.5	Time Walk Correction . . . . .	56
3.2	Determination of $\lambda_{pick}(t)/\lambda_{3\gamma}$ . . . . .	67
3.2.1	Time and Energy Spectra of the Ge Detectors . . . . .	67
3.2.2	Extraction of the Pick-off Contribution . . . . .	69
3.2.3	Determination of $\lambda_{pick}(t)/\lambda_{3\gamma}$ . . . . .	74
3.3	Decay Rate Fitting . . . . .	80
3.3.1	Time and Energy Spectrum of the YAP Scintillators . . . . .	80
3.3.2	Decay Rate Fitting . . . . .	82
3.4	Various Checks . . . . .	86
3.4.1	Energy Selection . . . . .	86
3.4.2	Base Cut . . . . .	86
3.4.3	Narrow-Wide Cut . . . . .	87
3.4.4	SRT Cut . . . . .	88
3.4.5	Data Sample . . . . .	88
3.5	Systematic Errors . . . . .	88
3.5.1	TDC Module Related Errors . . . . .	88
3.5.2	Contamination of the Pile-up Events . . . . .	91
3.5.3	Subtraction of $3\gamma$ Energy Spectrum . . . . .	91
3.5.4	Detection Efficiencies . . . . .	93
3.5.5	Other Sources of Systematic Errors . . . . .	96
3.5.6	Summary of the Systematic Errors . . . . .	97
3.6	Results of the Present Measurement . . . . .	97
<b>4</b>	<b>Discussion</b>	<b>100</b>
4.1	Experimental Meanings . . . . .	100
4.1.1	Solution of the Systematic Increase near the Prompt Peak . . . . .	100
4.1.2	Validation of the Fitting Start Time . . . . .	101
4.1.3	Improvements of the Monte Carlo Simulation . . . . .	102
4.1.4	Dependence on the Two Types of Silica Material . . . . .	104
4.2	Theoretical Implications . . . . .	104
<b>5</b>	<b>Conclusions</b>	<b>109</b>

<b>A Stark Shift</b>	<b>110</b>
A.0.1 Stark Effects on o-Ps Decay Rate . . . . .	110
A.0.2 Contribution of Charge on Primary Grains . . . . .	110
A.0.3 Contribution of Dipole Moment on the Surface of Grains	111
<b>B Expected Time Spectrum</b>	<b>115</b>
B.1 Probability of Accidental Events . . . . .	115
B.2 Expected Time Spectrum . . . . .	117
B.2.1 Pile-up by the Accidental Events $\sim \mathbf{X}(\bar{\mathbf{C}} + \mathbf{C})^\infty$ . .	118
B.2.2 Pile-up Events with the Prompt Signal $\sim \mathbf{AB}$ . . .	120
B.2.3 Contamination of Pile-up Events . . . . .	120
B.3 Time Spectrums of $\gamma$ -ray Detectors . . . . .	121
B.3.1 The Case of Ge Detector . . . . .	121
B.3.2 The Case of YAP Scintillator . . . . .	124

# List of Figures

1.1	The diagrams of one-loop corrections to o-Ps decay. . . . .	4
1.2	The energy spectrum with the $O(\alpha)$ correction . . . . .	5
1.3	The chronology of the o-Ps decay rate measurement. . . . .	9
2.1	Signal shapes of the various scintillators . . . . .	15
2.2	Schematic diagram of apparatus (side view). . . . .	18
2.3	Schematic diagram of apparatus (top view). . . . .	19
2.4	The level diagram of the $^{68}\text{Ge}$ isotope . . . . .	20
2.5	Internal structure of germanium detector. . . . .	22
2.6	The energy resolution of the Ge detectors as a function of the $\gamma$ -energy . . . . .	24
2.7	The relative peak efficiency of the germanium detectors. . . . .	25
2.8	Schematic diagram of Phase Locked Loop (PLL) . . . . .	27
2.9	Schematic diagram of Direct Digital Synthesis (DDS) . . . . .	28
2.10	Schematic diagram of the process data-flow. . . . .	30
2.11	Schematic diagram of electronics for trigger system. . . . .	32
2.12	Schematic diagram of electronics for YAP scintillator system. . . . .	34
2.13	Schematic diagram of electronics for Ge detector system. . . . .	36
2.14	Comparison of the measured Ge spectrum with the simulation using $^{85}\text{Sr}$ source . . . . .	41
2.15	The difference of the measured Ge spectrum and the simulation . . . . .	42
2.16	Pile-up events of Ge detector . . . . .	43
2.17	Comparison of the measured YAP spectrum with the simula- tion using $^{85}\text{Sr}$ source . . . . .	45
2.18	Collection efficiency of optical photon in YAP crystal . . . . .	46
3.1	Time and Energy spectrum of the YAP scintillator . . . . .	50
3.2	Time and Energy spectrum of the Ge detector . . . . .	51
3.3	The relative bin width . . . . .	53
3.4	The schematic of the Base cut . . . . .	54
3.5	Base spectra for Ge detectors . . . . .	54
3.6	Base spectra for YAP scintillator . . . . .	55
3.7	Base spectrum for the plastic scintillator . . . . .	56

3.8	The schematic of the Narrow-Wide (NW) cut . . . . .	57
3.9	Narrow-Wide spectra for Ge detectors . . . . .	57
3.10	Narrow-Wide spectra for YAP scintillators . . . . .	58
3.11	Time walk of YAP scintillator . . . . .	59
3.12	Time walk of plastic scintillator . . . . .	60
3.13	The rise-time of the Ge detectors . . . . .	61
3.14	Time walk of Ge detectors . . . . .	62
3.15	Time walk of the slow rise-time component . . . . .	64
3.16	Time spectra of Ge detectors without silica target . . . . .	65
3.17	Time spectra of Ge detectors . . . . .	66
3.18	$3\gamma$ SRT cut efficiency of Ge detectors . . . . .	66
3.19	Time spectrum of Ge detectors . . . . .	68
3.20	511 keV photoelectric peak of the prompt events . . . . .	69
3.21	Energy spectrum of the delayed region. . . . .	71
3.22	Subtraction of the $3\gamma$ spectrum . . . . .	72
3.23	Energy spectrum of the pick-off events . . . . .	73
3.24	Pick-off ratio $\lambda_{pick}(t)/\lambda_{3\gamma}$ . . . . .	76
3.25	Uncertainties of the parameters (RUN I) . . . . .	78
3.26	Uncertainties of the parameters (RUN II) . . . . .	79
3.27	Energy spectrum of YAP scintillator in the delayed region . .	80
3.28	Time spectrum of the YAP scintillators . . . . .	81
3.29	Fitted decay rate (RUNI) . . . . .	84
3.30	Fitted decay rate (RUNII) . . . . .	85
3.31	Decay rates of the four samples for RUN I. . . . .	89
3.32	Decay rates of the four samples for RUN II. . . . .	90
3.33	The pick-off spectrum with varied $3\gamma$ normalization . . . . .	92
3.34	$\xi$ -parameter with varied $3\gamma$ normalization . . . . .	94
3.35	The results of the two runs and the combined result . . . . .	99
4.1	The fitted decay rate with the fitting start time before 80 ns	103
4.2	The measured pick-off ratios with two types of silica material	105
4.3	The history of the o-Ps decay rate measurements including the present measurement . . . . .	107
4.4	The relation between the resent measurements and the theo- retical predictions . . . . .	108
A.1	Schematic diagram of SiO <sub>2</sub> grain. . . . .	112
A.2	A definition of the variables used for calculation in the context	113
B.1	Probability of accidental events around the trigger signal . . .	116
B.2	Time distribution of the the $\gamma$ -rays . . . . .	117
B.3	The suppression region in which accidental events spoil the event . . . . .	119
B.4	Suppression region of the pile-up cuts . . . . .	122

B.5	Suppression factor $S(t)$ for Ge detector . . . . .	123
B.6	Suppression factor $S(t)$ for YAP scintillator . . . . .	124

# List of Tables

1.1	The classification of Ps according to their quantum numbers.	1
1.2	The summary of the logarithmic contribution . . . . .	4
1.3	Summary of QED calculation for o-Ps decay rate . . . . .	6
1.4	The history of the o-Ps decay rate measurements . . . . .	7
2.1	Characteristics of two powders used in the measurement . . .	21
2.2	Crystal size of germanium detectors . . . . .	23
2.3	Properties of YAP scintillator . . . . .	26
2.4	Energy resolution of the YAP scintillator . . . . .	26
2.5	Quantities measured with ADCs . . . . .	38
2.6	Quantities measured with TDCs . . . . .	38
2.7	Specifications of the CAMAC modules . . . . .	39
3.1	Properties of the RUNs . . . . .	48
3.2	Energy resolution of the prompt events . . . . .	67
3.3	Typical stop rate of Ge detectors . . . . .	70
3.4	Compton factor $f_{\text{compton}}$ . . . . .	70
3.5	Peak value and resolution of the pick-off events . . . . .	74
3.6	Conversion factor $\mathcal{F}$ . . . . .	74
3.7	Definition of the time windows . . . . .	75
3.8	Summary of $\lambda_{\text{pick}}(t)/\lambda_{3\gamma}$ fitting result . . . . .	77
3.9	Uncertainties of the fitted parameter (RUN I) . . . . .	77
3.10	Ratio $\epsilon_{\text{pick}}/\epsilon_{3\gamma}$ of YAP scintillators . . . . .	82
3.11	Typical stop rate of YAP scintillators . . . . .	82
3.12	Summary of the $\xi$ -parameters . . . . .	93
3.13	The difference between the measured data and the Monte Carlo simulation . . . . .	95
3.14	The difference between the measured data and the Monte Carlo simulation . . . . .	96
3.15	Summary of the systematic errors . . . . .	98

# Chapter 1

## Introduction

The aim of this experiment is a test of bound state Quantum ElectroDynamics (QED). The predictions of the higher order corrections are verified by measuring the orthopositronium (o-Ps) decay rate precisely. As an introduction, properties of o-Ps are explained in the first section. Then the theoretical predictions of bound state QED and the previous measurements of o-Ps decay rate are summarized in the following sections.

### 1.1 Properties of Positronium

Positronium (Ps), the bound state of the electron ( $e^-$ ) and the positron ( $e^+$ ), is the lightest hydrogen-like atom bound by the electromagnetic interaction. Since Ps is a purely leptonic system and effectively free from hadronic and weak interaction effects, precision measurements of decay rate and energy levels give us direct information about bound state QED. Therefore, Ps is considered as the best testing ground for bound state formalism in quantum field theory.

A Ps consists of two fermions as hydrogen atom, and its wave functions are classified according to the principal quantum number  $n$ , a sum of the orbital angular momentum  $\ell$  and the spin angular momentum  $s$ , and its projection on a quantization axis  $m$ . In the case of the ground state, that is  $n = 1$  and  $\ell = 0$ , Ps can be simply classified to the total spin  $s$  as in Table 1.1.

Total Spin $s$	Projection $m$	State	$C$ parity	Name
0	0	singlet	even	parapositronium (p-Ps)
1	0, $\pm 1$	triplet	odd	orthopositronium (o-Ps)

Table 1.1: The classification of Ps according to their quantum numbers.

A fermion-antifermion system with orbital angular momentum  $\ell$  and spin

angular momentum  $s$  has a parity of  $(-1)^{\ell+s}$  under a charge-conjugation transformation ( $C$ ). Thus o-Ps and p-Ps have odd and even  $C$  parities respectively. Due to the  $C$ -invariance of the electromagnetic interaction, this difference plays a crucial role on the decay modes. In fact, o-Ps decays only into odd  $\gamma$ 's and p-Ps decays only into even  $\gamma$ 's since the the system consisting of  $n$  photons have a  $C$  parity of  $(-1)^n$ . In addition, single photon decay in vacuum is prohibited by energy-momentum conservation. Then, the decay modes of o-Ps and p-Ps are as follows.

$$\begin{aligned} \text{o-Ps} &\rightarrow n\gamma, \quad n = 3, 5, 7, 9 \dots \\ \text{p-Ps} &\rightarrow n\gamma, \quad n = 2, 4, 6, 8 \dots \end{aligned}$$

As a number of photon increses, a number of electromagnetic vertex increases and the width of the decay mode decreases by a factor of  $\alpha$ . Furthermore, the phase space of the final state is getting smaller as the number of final state photon increases. Thus, decay modes into many photons are highly suppressed. In fact, the dominant decay mode of o-Ps is  $3\gamma$ , and the contribution of the  $5\gamma$  decay is only a ppm level. The theoretical branching ratio of the  $5\gamma$  decay is as follows [1].

$$\begin{aligned} BR_{th}(\text{o-Ps} \rightarrow 5\gamma) &= \Gamma(\text{o-Ps} \rightarrow 5\gamma)/\Gamma(\text{o-Ps} \rightarrow \gamma\gamma\gamma) \\ &= 0.19(1) (\alpha/\pi)^2 \\ &\simeq 1.0 \times 10^{-6} \end{aligned} \tag{1.1}$$

The prediction has been confirmed by the measurement [2] within the experimental accuracy.

$$BR_{ex}(\text{o-Ps} \rightarrow 5\gamma) \simeq 2.2_{-1.8}^{+2.6} \times 10^{-6}. \tag{1.2}$$

Thus, the influence of the  $5\gamma$  decay contribution to the total width is negligible.

This relation also suggests that the decay rate of p-Ps is approximately  $10^3$  times higher than the decay rate of o-Ps. In fact, the measured lifetime of p-Ps is  $125.14 \pm 0.03$  ps [3] and 1130 times shorter than the o-Ps's. This facilitates the separation of o-Ps events from that of p-Ps in the experiment.

## 1.2 Theoretical Predictions of Orthopositronium Decay Rate

Theoretical expression for o-Ps decay rate can be written in the form of perturbation as follows,

$$\lambda_{\text{o-Ps}} = \lambda_o^{(0)} \left[ 1 + A_o \left( \frac{\alpha}{\pi} \right) + B_o \left( \frac{\alpha}{\pi} \right)^2 \right]$$

$$\left. +C_o \alpha^2 \ln \frac{1}{\alpha} + D_o \frac{\alpha^3}{\pi} \ln^2 \frac{1}{\alpha} + E_o \frac{\alpha^3}{\pi} \ln \frac{1}{\alpha} + \dots \right] \quad (1.3)$$

where  $\lambda_o^{(0)}$  is the lowest order decay width of o-Ps. The higher order terms, whose coefficients are expressed as  $A_o$ ,  $B_o$ ,  $C_o$ ,  $D_o$ ,  $E_o$ , will be discussed in the following sections. The ellipses denote unknown higher order terms which are neglected in this thesis.

### 1.2.1 The Lowest Order Decay Width

The lowest order calculation of o-Ps have been done by Öre and Powell [4], and confirmed later by other authors [5, 6]. The lowest order decay width is given as,

$$\lambda_o^{(0)} = \frac{2(\pi^2 - 9)m_e\alpha^6}{9\pi} = 7.211\,17 \mu s^{-1} \quad (138.67 \text{ ns}) \quad (1.4)$$

where  $m_e$  is the electron mass. In this formula, the three  $\gamma$ -vertexes contribute a factor of  $\alpha^3$ . The remaining  $\alpha^3$  factor is originated from the flux factor which is the probability that the distance between the electron and the positron is zero.

### 1.2.2 $O(\alpha)$ Correction

The  $O(\alpha)$  corrections come from the single photon exchange processes as shown in Fig. 1.1. Many authors have evaluated the one-loop contributions to the decay width of o-Ps, and they have obtained the consistent results with each other. The most accurate result of the  $O(\alpha)$  correction for o-Ps decay rate was obtained by Adkins [7] in an analytical form. The value is,

$$A_o = -10.286\,606(10) \quad (1.5)$$

which results in -2.389 % correction to the lowest order decay width.

The evaluation of the  $O(\alpha)$  correction on the energy spectrum of the emitted photon is carried out as well. This correction is almost flat over the photon energy, and the relative variation does not exceed 1 % around 511 keV as shown in Fig. 1.2. The variation of the energy spectrum due to the  $O(\alpha^2)$  correction is expected to be further small. Then, the  $O(\alpha)$  corrected matrix element is used in the Monte Carlo simulation.

### 1.2.3 $\alpha^2 \ln(\alpha^{-1})$ , $\alpha^3 \ln^2(\alpha^{-1})$ , $\alpha^3 \ln(\alpha^{-1})$ Contributions

The logarithmic corrections can be considered as the relativistic effects in the wave function of Ps. The logarithmic two-loop corrections and the leading logarithmic corrections at three-loop are already obtained by some authors in analytical forms. Since  $\ln(\alpha^{-1})$  is actually about 5, the  $O(\alpha^2 \ln(\alpha^{-1}))$  correction is as important as the  $O(\alpha^2)$  correction. The already known coefficients are summarized in Table 1.2

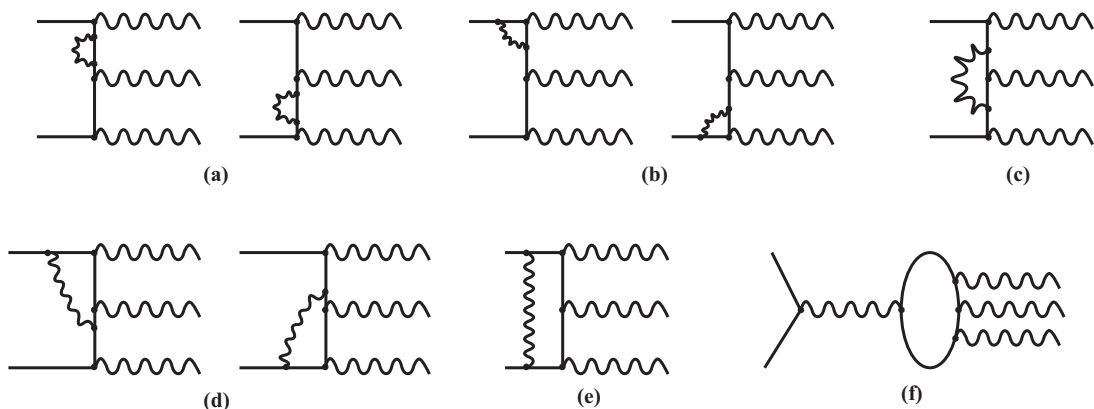


Figure 1.1: Graphs contributing to the o-Ps decay amplitudes through order- $\alpha$ . Each figure represents (a) self-energy, (b) outer-vertex, (c) inner-vertex, (d) double-vertex, (e) ladder, and (f) annihilation contributions.

	Coefficient	correction to $\Gamma^{(0)}$	reference
$C_o$	$-1/3$	$-87 \text{ ppm}$	[8, 9, 10]
$D_o$	$-3/2$	$-4.4 \text{ ppm}$	[11, 12]
$E_o$	$+5.517$	$+3.3 \text{ ppm}$	[13, 14]

Table 1.2: The summary of the logarithmic contribution

#### 1.2.4 $O(\alpha^2)$ Correction

The calculation of the  $O(\alpha^2)$  correction to the decay rate of Ps is so complicated if the traditional bound-state methods are employed such as *Bethe-Salpeter analysis*. This is because each term in a traditional expansion has contribution from both nonrelativistic and relativistic energy scales. To overcome this difficulty, a new procedure has been developed and applied to the calculations of the coefficient  $B_o$ .

The calculation is based on a rigorous nonrelativistic reformation of QED called *Nonrelativistic Quantum Electrodynamics* (NRQED). In this framework of the effective field theory, the  $O(\alpha^2)$  correction terms are separated into nonrelativistic (soft) parts and relativistic (hard) parts.

A complete calculation of  $B_o$  had not been carried out until quite recently. Only some partial results on the non-logarithmic  $O(\alpha^2)$  corrections had been carried out [15, 16, 17]. But, in recent theoretical efforts, a complete evaluation of this correction have been performed by Adkins [18]. The result is  $B_o = 45.06(26)$ , and its contribution to the lowest order calculation is  $243.1(1.4) \text{ ppm}$ .

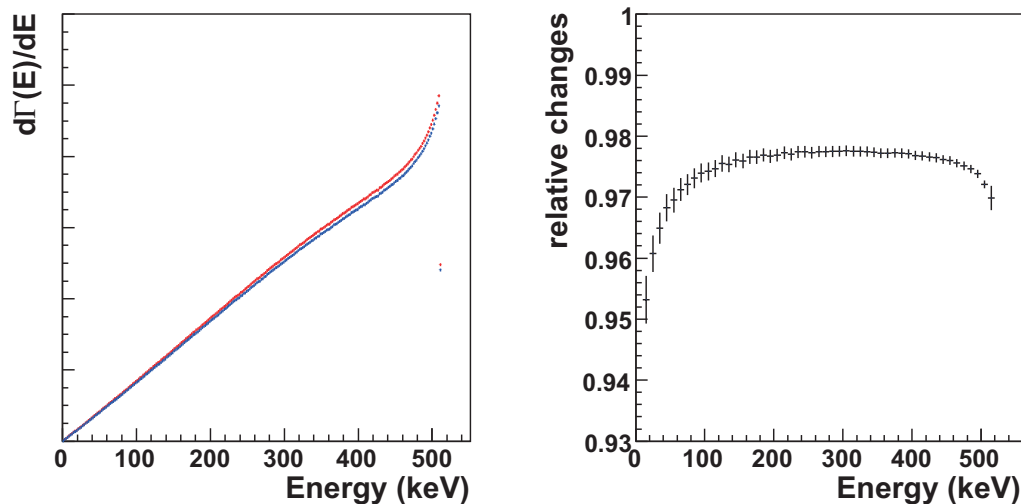


Figure 1.2: (a) The lowest order energy spectrum of  $3\gamma$  decay (red line) and the energy spectrum with the  $O(\alpha)$  correction (blue line). (b) The relative change of the energy spectrum by the  $O(\alpha)$  correction.

### 1.2.5 Summary of the QED Prediction

As described above, the higher order corrections are important for o-Ps decay rate. Table 1.3 shows the summary of the calculation for o-Ps decay rate. Except for the last line of the table, that is the non-logarithmic  $O(\alpha^2)$  term, the calculations are confirmed by several authors. On the other hand, the value  $B_o$  has just been obtained by the recent work, and it need to be verified by the other calculations. Thus it would be premature to accept the result now.

In this thesis, the following value is referred to as the  $O(\alpha^2)$  corrected QED prediction [19].

$$\Gamma_{o-Ps} = 7.039\,979 \mu s^{-1}. \quad (1.6)$$

Comparison between the theory and the experiments will be performed with this decay rate.

## 1.3 Previous Measurements of Orthopositronium Decay Rate

The situation is more complicated in the experiment. The significant discrepancy between the prediction and the measurement had existed since latter half of 1970's. But, the recent experiments reported the consistent results with the prediction. Before we discuss their results, we will review the

terms	correction ( <i>ppm</i> )	decay rate ( $\mu s^{-1}$ )	lifetime ( <i>ns</i> )
tree level	0.0	7.211 167	138.6738
$A_o (\frac{\alpha}{\pi})$	-23893.9	7.038 864	142.0684
$C_o \alpha^2 \ln(1/\alpha)$	-87.4	7.038 234	142.0811
$D_o (\alpha^3/\pi) \ln^2(1/\alpha)$	-4.4	7.038 202	142.0817
$E_o (\alpha^3/\pi) \ln(1/\alpha)$	+3.3	7.038 226	142.0813
$B_o (\frac{\alpha}{\pi})^2$	243.1	7.039 979	142.0459

Table 1.3: Summary of QED calculation for o-Ps decay rate

experimental techniques of o-Ps decay rate measurement in the next section.

### 1.3.1 Techniques of the Measurement

In all the previous measurements, a positron was injected into a target material to form o-Ps, and the time interval between the positron injection and the detection of  $\gamma$ -rays emitted from o-Ps was measured. This was a common idea in all the measurements, and only the target materials were altered in each measurement. The employed target materials are classified into three types, the gas, the surface of cavity which is coated by oxide material (e.g. MgO), and the powders of SiO<sub>2</sub>.

The *Gas experiments* are the most popular and the earliest techniques. In this technique, injected positrons form Ps in gases at various pressures. Then, the decay rate in vacuum is estimated by extrapolation to zero density of the gas.

In the *Cavity experiments*, Ps is formed in the vacuum container when the slow positron beam hits the MgO surface of the cavity. The intrinsic decay rate in vacuum was estimated by extrapolation to infinite cavity size. The extrapolated values, in this case, are the surface area of the cavity container divided by volume, ( $S/V$ ).

In the *Powder experiments*, positrons are injected from a radioactive source and Ps is formed in SiO<sub>2</sub> powders. Powder experiments are performed at various powder density, and the extrapolation to zero density yields o-Ps decay rate in vacuum.

Another type of powder experiment appeared in 1995 [20, 21]. This was quite different from all the previous experiments, because it no longer used extrapolation. In this experiment, the effect of target material, which is observed as a increase of the decay rate, is directly estimated by detecting the  $\gamma$ -rays from  $2\gamma$  annihilation on the target material. We will closely discuss this technique in the next chapter.

### 1.3.2 History of the Measurement

The history of the o-Ps decay rate measurements are summarized in Table 1.4 and plotted in Fig. 1.3 to see the historical changes of the measured value with its precision.

index	Year	Decay rate ( $\mu s^{-1}$ )	Total error		Method	Lifetime ( $ns$ )	Reference
			( $\mu s^{-1}$ )	( $ppm$ )			
1	1968	7.275	0.015	2062	gas(Freon)	137.70	[22]
2	1976	7.104	0.006	844	SiO <sub>2</sub> powder	140.77	[23]
3	1976	7.09	0.02	2821	cavity	141.04	[24]
4	1978	7.056	0.007	992	gas(Freon, isobutane)	141.72	[25]
5	1978	7.067	0.021	2972	SiO <sub>2</sub> powder	141.50	[25]
6	1978	7.050	0.013	1844	cavity	141.84	[26]
7	1978	7.121	0.012	1685	cavity	140.41	[27]
8	1978	7.045	0.006	852	gas	141.94	[28]
9	1982	7.051	0.005	709	gas(isobutane)	141.84	[29]
10	1987	7.031	0.007	996	cavity	141.22	[30]
11	1987	7.0516	0.0013	184	gas(isobutane, N <sub>2</sub> ,etc.)	141.81	[31, 32]
12	1989	7.0514	0.0014	199	gas(N <sub>2</sub> , Ne)	141.82	[33]
13	1990	7.0482	0.0016	227	cavity	141.88	[34, 35]
14	1995	7.0398	0.0029	412	SiO <sub>2</sub> powder	142.05	[20, 21]
15	2002	7.0404	0.0013	182	cavity	142.04	[36]
16	2003	7.0396	0.0016	230	SiO <sub>2</sub> powder	142.05	[37, 38]

Table 1.4: The history of the o-Ps decay rate measurements

#### *The first stage*

The first measurement of o-Ps decay rate was performed in 1968 [22]. In those days, theory and experiment agreed at 0.2 % level of accuracy. But in 1976, two experiments were performed and resulted in the large discrepancy between the theory and the experiments. This caused the reevaluation of both the theory and the experiments.

#### *The second stage*

After the new calculation in 1977 [39], the new experiments drastically improve the accuracy. In the group of Michigan, which is sometimes referred to as Ann Arbor, the cavity and the gas experiments were carried out and remarkable progress were made. Especially, the gas experiments were performed for various gases to check the gas independency. Here again, the discrepancy with the theory motivated a

further investigation on both the theory and experiments.

#### *The third stage*

The two types of measurements, the cavity [34] and the gas [31, 33] experiments was performed at around the beginning of 1990's. They achieved the accuracy of 200 *ppm* level and the discrepancy became definite. The results were consistently higher than the theoretical prediction by a 1000 *ppm* level. This discrepancies had been called *orthopositronium lifetime puzzle*, and aroused various discussions for the physical interpretations. Since most measurements resulted in the higher decay rate than the theoretical prediction, it was considered that there may be some unknown rare decay channels. Thus the exotic decay modes had been searched for in that period. However, no sign of the exotic decay has been observed by now [40].

#### *The fourth stage*

In 1995, a new measurement was performed in our laboratory (Tokyo group) using SiO<sub>2</sub> powder [20] and resulted in a consistent result with the QED prediction. Since the experiment employed the new technique which directly measured the effect of material, the systematic error accompanying the extrapolation method was considered as the main cause of the discrepancy. In 2001, Tokyo group improved the accuracy to the level of 200 *ppm* [37] and their results are in agreement with the prediction.

Ann Arbor group admitted the possibility that the incomplete thermalization in low-pressure gases distorted the measured value in their gas experiment. For their cavity experiment, they found main problem was caused by not fully thermalized Ps, which increased the observed decay rate through collision quenching and escapes from the detection area. In 2003, they reported the new measured value consistent with the theoretical prediction [36].

This thesis is organized as follows.

Chapter 2 describes the experiment. The experimental techniques and apparatus are explained in detail. The Monte Carlo simulation used in this experiment is also explained.

Chapter 3 provides the analysis of the measured data. All the procedures of the analysis are explained step by step. The systematic errors accompanying the measurement are also explained. Then, the final result is shown.

In Chapter 4, the experimental meanings and the theoretical implications of the obtained results are discussed.

Finally, Chapter 5 concludes this experiment.

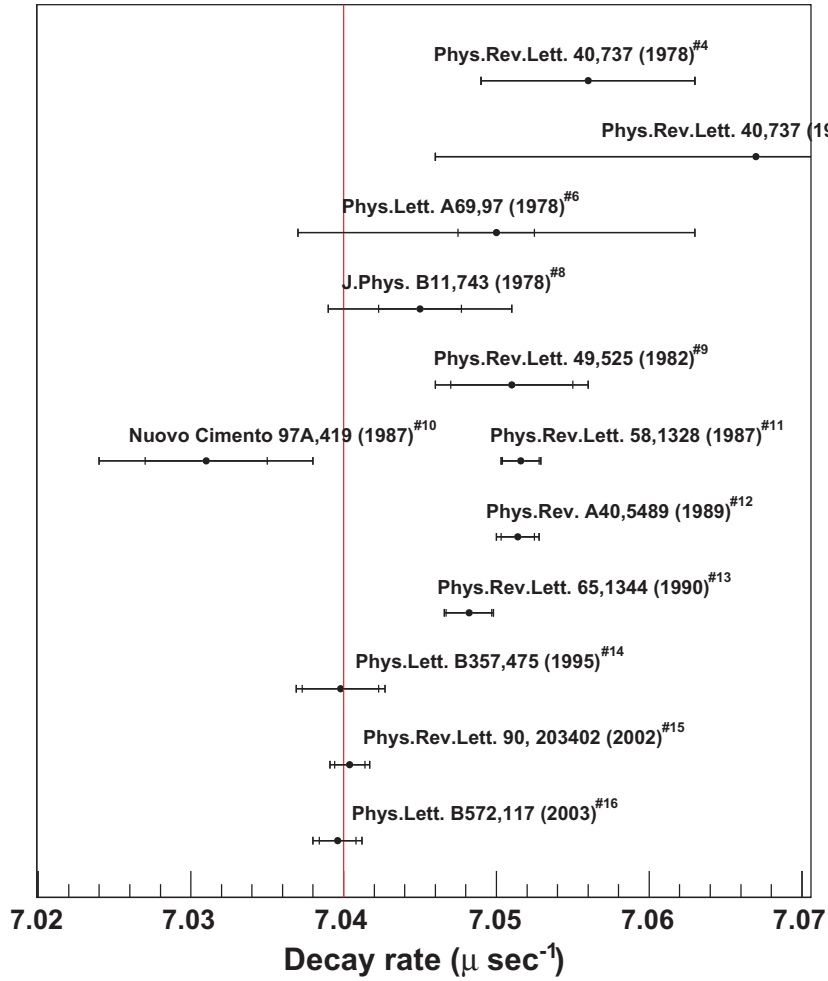


Figure 1.3: The chronology of the o-Ps decay rate measurement. The number on the right shoulder of each item indicates a corresponding index number in Table 1.4. Vertical band represents the  $O(\alpha^2)$ -corrected NRQED prediction of  $7.039979 \mu \text{ s}^{-1}$ . The inside line on each error bar represents a statistics error.

## Chapter 2

# Experiment

In this chapter, the details of the experiment are described. First of all, the method adopted in this measurement is explained. Then, the detailed descriptions on the experimental apparatus will follow.

### 2.1 Method of the Experiment

#### 2.1.1 Pick-off Annihilation

In all the o-Ps decay rate measurements, positrons from the  $\beta^+$  source are injected into the target materials to form Ps. These materials such as gases, oxide powders (e.g.  $\text{SiO}_2$ ) or cavities whose inside walls are coated by oxide materials ( $\text{MgO}$  or  $\text{Al}_2\text{O}_3$ ), serve as the source of electrons constituting the o-Ps. The o-Ps continues to collide with the surrounding target materials, and inevitably cause the pick-off annihilation with the atomic electrons inside the target materials. It also occurs that the electron of the o-Ps exchange its spin with the electrons of the target materials. This conversion from o-Ps to p-Ps results in the rapid annihilation into two photons, which is referred to as *spin-flip*.

In these circumstances, the observed decay rate is expressed as

$$\lambda_{obs}(t) = \lambda_{3\gamma} + \lambda_{pick}(t). \quad (2.1)$$

where  $\lambda_{3\gamma}$  is the intrinsic decay rate of o-Ps and  $\lambda_{pick}(t)$  is the contribution of the pick-off annihilation, which is generally dependent on time. Thus, how to deal with the pick-off annihilation is a main issue in all the measurements.

#### 2.1.2 Previous Extrapolation Method

Phenomenologically, the pick-off rate would be expressed as,

$$\lambda_{pick}(t) = n\sigma_a v(t), \quad (2.2)$$

where  $n$  is the density of the target materials,  $\sigma_a$  is the annihilation cross section, and  $v$  is the velocity of the o-Ps. Since the pick-off rate is proportional to the density of the target material, an extrapolation method is considered to be effective. In the extrapolation method, the decay rate was measured at some points varying the density of the target material and extrapolation to zero density yields the intrinsic decay rate. Indeed, the time dependency of the o-Ps velocity is a trouble at this stage. But, the velocity of the o-Ps must converge to a constant value corresponding to the room temperatures of 0.03 eV after some time from the o-Ps formation.

In fact, a number of experiments had been performed on the above assumptions by the early 90's. Unfortunately, they suffered from the large systematic error, that was known as *orthopositronium lifetime puzzle*. The reasons are as follows.

- It is difficult to determine the time when the o-Ps are fully thermalized. Since the number of o-Ps event decreases exponentially in the later decay time region, one cannot figure out the time when the decay rate will be constant. Therefore, the fitting start time inevitably has the large systematic uncertainty.
- The situation gets worse when the density of the target material is varied. The thermalization process is strongly dependent on the density of the material and the properties of the surface. Especially in the lower density, the o-Ps may not have been fully thermalized by its decay time which is several hundreds ns at most. This will disturb the assumption of the linear dependence on the density.
- The kinematic energy of the o-Ps in the apparatus obeys the Boltzmann equation in the large part. But especially in cavity experiment, there are some components which are not fully slowed down in the target material. They have the high probability of the pick-off annihilation on the cavity wall and sometimes escape from the detection area. Thus, the estimation of those component and understanding of their behavior are required.

### 2.1.3 Direct Measurement of the Pick-off Rate

In order to overcome the difficulty of the extrapolation method, the other method is employed in this experiment. The idea is that if the pick-off rate is directly measured with its time dependency, the intrinsic decay rate will be determined from the observed decay rate without the extrapolation procedures. In this case, no assumptions on the thermalization process and the behavior of the o-Ps are required.

For this purpose, high energy resolution germanium detectors are used in this experiment. They measure the energy of the  $\gamma$ -ray together with

its decay time. The energy distribution of the  $\gamma$ -rays from the pick-off annihilation is the monochromatic 511 keV peak and totally different from the continuous distribution of the  $3\gamma$ . Therefore, the ratio of the pick-off  $2\gamma$  to  $3\gamma$  is easily obtained from the energy spectrum of the germanium detector. Once the  $\lambda_{pick}(t)/\lambda_{3\gamma}$  has been determined, the observed time spectrum can be fitted with the function including the ratio to extract the intrinsic decay rate.

The steps to the function of the expected time spectrum is rather straightforward. The population of o-Ps at time  $t$ ,  $N(t)$ , is expected to obey the following differential equation,

$$\frac{d}{dt}N(t) = -(\lambda_{3\gamma} + \lambda_{pick}(t)) N(t), \quad (2.3)$$

the solution of this equation is,

$$N(t) = N_0 \exp\left(-\int_0^t (\lambda_{3\gamma} + \lambda_{pick}(t')) dt'\right). \quad (2.4)$$

Then, the measured time spectrum,  $N_{obs}(t)$  is expected to be,

$$\begin{aligned} N_{obs}(t) &= \varepsilon_{\lambda_{obs}}(t)N(t) \\ &= (\varepsilon_{3\gamma}\lambda_{3\gamma} + \varepsilon_{pick}\lambda_{pick}(t)) N(t) \\ &= \varepsilon_{3\gamma}\lambda_{3\gamma} \left(1 + \frac{\varepsilon_{pick}}{\varepsilon_{3\gamma}} \frac{\lambda_{pick}(t)}{\lambda_{3\gamma}}\right) \\ &\quad \times N_0 \exp\left(-\lambda_{3\gamma} \int_0^t \left(1 + \frac{\lambda_{pick}(t')}{\lambda_{3\gamma}}\right) dt'\right), \end{aligned} \quad (2.5)$$

where  $\varepsilon_{pick}$  and  $\varepsilon_{3\gamma}$  are the detection efficiencies for the pick-off annihilations and  $3\gamma$  decays respectively.

Finally we obtain the following form,

$$N_{obs}(t) = e^{-R_{stop}t} \left[ \left(1 + \frac{\varepsilon_{pick}}{\varepsilon_{3\gamma}} \frac{\lambda_{pick}(t)}{\lambda_{3\gamma}}\right) N_0 \exp\left(-\lambda_{3\gamma} \int_0^t \left(1 + \frac{\lambda_{pick}(t')}{\lambda_{3\gamma}}\right) dt'\right) + C \right]. \quad (2.6)$$

The constant term  $C$  comes from accidental hits whose stop signals do not correspond to the  $\beta$  trigger. Another factor  $\exp(-R_{stop}t)$  in Eq. (2.6) comes from the fact that the TDC always accept the first  $\gamma$  hit as a stop signal. The size of the term is determined by the random counting rate  $R_{stop}$ , which is proportional to a strength of the positron source.

In the end of this section, the pick-off rate in the thermalization process will be treated in a rather analytic manner. If the fractional energy loss of o-Ps per collision with the material and the collision rate are dependent on its energy, time dependence of the average kinetic energy of o-Ps at time  $t$ ,  $\overline{E}(t)$ , is derived from the Boltzmann equation as in [41, 42],

$$\frac{d}{dt}\overline{E(t)} = -\sqrt{2m_{Ps}\overline{E(t)}}\left(\overline{E(t)} - 3k_B T\right) \sum_{j=0}^{\infty} a_j \left(\frac{\overline{E(t)}}{k_B T}\right)^{j/2}, \quad (2.7)$$

where  $m_{Ps}$  is the mass of o-Ps,  $T$  is the room temperature, and the  $k_B$  is the Boltzmann constant. In the equation, the asymptotic value of  $\overline{E(t)}$  is  $3k_B T$  and the momentum transfer cross section of the SiO<sub>2</sub> is expanded in terms of  $\overline{E(t)}$ . Then, the coefficients  $a_j$  include all the information of the thermalization process of o-Ps.

Since the pick-off rate is proportional to the average velocity of the o-Ps as can be seen in Eq. (2.2), the ratio of the pick-off rate to the intrinsic o-Ps decay rate,  $\theta(t) \equiv \lambda_{pick}(t)/\lambda_{3\gamma}$ , obeys the following differential equation,

$$\frac{d}{dt}\theta(t) = -C\left(\theta(t)^2 - \theta_{\infty}^2\right) \sum_{j=0}^{\infty} a_j \theta(t)^j, \quad (2.8)$$

where  $\theta_{\infty} \equiv \theta(t \rightarrow \infty)$ ,  $a_j$  ( $j = 0, 1, 2, \dots$ ), and  $C$  are constant values.

It is well known from the previous measurements that it takes about 600 ns for o-Ps to be well thermalized in low-density SiO<sub>2</sub> powders.

#### 2.1.4 Measurements in 1995 and 2001

In 1995, the method which directly measures the pick-off rate was used for the first time [20, 21]. The result was consistent with the QED prediction.

In 2001, the more accurate experiment was performed by the same technique [37, 38]. In this experiment, the following progress was made.

- The two types of SiO<sub>2</sub> powder with quite different pick-off ratios were used for the systematic test of the direct pick-off correction method. The obtained values are consistent with each other.
- The timing system and the time walk correction were improved. In the end, the dependence of the decay rate on the fitting start time was disappeared by 100 ns fitting start time.
- The total error of about 230 ppm was achieved. The obtained decay rate was consistent with the  $O(\alpha^2)$ -corrected QED prediction.

However there were several remaining problems,

- The experimental error was still large for the test of  $O(\alpha^2)$  correction which account for 240 ppm of the decay rate.
- The fitting start time of 100 ns was used for the decay rate fitting because the decay rate was systematically increasing before 100 ns. The origin of this increase was not understood at that time, and clear explanation is needed to prove the validity of the method.

- The energy window was set to the Compton free region. But, the dependence on the energy window was rather large.
- Some systematic uncertainties were not fully understood. For example, the detection efficiency was only estimated by the Monte Carlo simulation.

## 2.2 New Features of the Present Measurement

In order to clear up the remaining problems (see Sec. 2.1.4), the following trials are performed in the present measurement and some improvements are made in the end.

### 2.2.1 Introduction of Fast Inorganic Scintillator

The previous measurements adopted NaI or CsI scintillators. These scintillators have the good energy resolution. However, they have the rather long time constants and the timing characteristics are not so good. Then, other fast inorganic scintillators such as YAP, GSO, YLSO are evaluated in the laboratory. The signal shapes measured with Flash ADC are shown in Fig. 2.1.

The main characteristics of the signal shapes are as follows.

#### **NaI scintillator**

The time constant is as long as 200 *ns*. In addition, the large tail is observed by several  $\mu s$ .

#### **YAP scintillator**

The time constant is about 30 *ns*. The long tail is also observed. But, the amount is a % level.

#### **GSO scintillator**

The time constant is about 60 *ns*. The second component with the time constant of about 300 *ns* is clearly seen.

#### **YLSO scintillator**

The time constant is about 40 *ns*. The long component is hardly observed. Unfortunately, the large  $\beta$  decay background is observed.

Thus, the YAP scintillator is found to be most suitable for the decay rate measurement. The detailed properties of the YAP scintillator are shown in Sec. 2.3.3.

The setup of the measurement are newly constructed on the base of the YAP scintillator. With the introduction of the YAP scintillator, the following improvements are made.

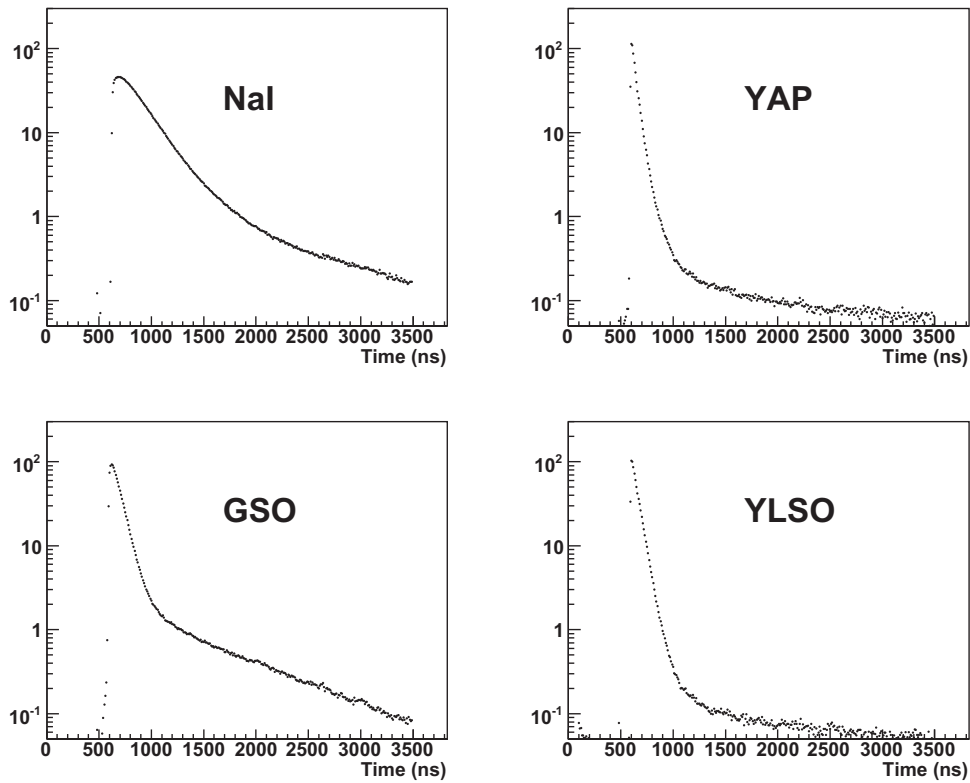


Figure 2.1: Signal shapes of the various scintillators. Signal shapes are measured with Flash ADC.

- The excellent time resolution is obtained. The resolution is less than 1 *ns* for the whole energy region.
- Due to the fast time constant of 30 *ns*, the effect of the pile-up is decreased by a factor of 10. It makes the system more tolerant to high event rate.

### 2.2.2 New Design of Ps Formation Assembly

The previous measurement adopted  $^{22}\text{Na}$  for positron source. But, it is found that the large part of positrons emitted from  $^{22}\text{Na}$  are absorbed in the trigger plastic scintillator. To increase the efficiency of the o-Ps formation, more energetic positron source  $^{68}\text{Ge}$  is introduced. Note that, as shown in Fig.2.4, positrons are emitted from the daughter nucleus  $^{68}\text{Ga}$ . In the case of  $^{68}\text{Ge}$ , about 80 % of the positrons path through the scintillator and the aluminized mylar without being absorbed. Then, the o-Ps formation assembly are designed to meet the change. The detailed descriptions are shown in Sec. 2.3.1 and the main structure is composed of the following two systems.

#### trigger system

The emission of positron is detected by the thin plastic scintillator, whose thickness is optimized to 200  $\mu\text{m}$ . The light of the trigger scintillator is collected by a mirror made of aluminized mylar.

#### anti-trigger system

Some positrons of  $^{68}\text{Ge}$  are too energetic to stop in the silica target, which is about 3 *cm* thick. The 1 *mm* thick plastic scintillator on the wall of the container detects these positrons and suppresses the trigger signal. The system is referred to as the anti-trigger.

### 2.2.3 Geant4 Simulation and its Validation

The previous measurement used a  $\gamma$ -ray simulation they developed for the experiment. The simulation is fast and correctly reproduces the absorption coefficients of  $\gamma$ -ray. But, the present measurement adopts the Geant4 simulation [43] for the following reasons. The detailed procedures of the simulation is shown in Sec. 2.4.

- The Geant4 packages are validated by many users and their functions are established at present.
- The Geant4 handles positron. The simulation of positron is needed to determine the decay point. In addition, the secondary particles of the emitted positron such as electrons, bremsstrahlung- $\gamma$ 's sometimes hit the detector or anti-trigger.

- The Geant4 simulates the secondary particles. The secondary electrons and bremsstrahlung- $\gamma$ 's sometimes enter the detector or escape from the detector. The effect is observed in the Compton free region.
- The Geant4 supports the various effects in the low energy region. For example, the Geant4 reproduces Pb X-rays and the broad Compton edge, which is caused by the electron's binding momentum.

The Geant4 correctly simulates all the physics interactions. But, some characteristics specific to the detector are not reproduced, such as charge collection efficiency and optical photon collection efficiency. Therefore, the response function of the detector is modified by the measured data (see Sec. 2.4). Consequently, the realistic response function suppresses the systematic uncertainty of the detection efficiency which leads to the error of the pick-off correction and the energy window dependence of the decay rate.

## 2.3 Description of Apparatus

In this experiment, two measurements are performed, that are referred to as 'RUN I' and 'RUN II'. Some properties of the experimental setup such as the target material, the number of detectors has been changed between the RUN's.

### 2.3.1 Positronium Formation Assembly

The positronium formation assembly used in this experiment is shown in Fig. 2.2. The  $^{68}\text{Ge}$  positron source (endpoint 1.9 MeV) is placed at the center of the assembly. The positrons are actually emitted from the daughter nucleus  $^{68}\text{Ga}$  as shown in Fig.2.4. The strength of the source is approximately  $0.3 \mu\text{Ci}$  for RUN I and  $0.2 \mu\text{Ci}$  for RUN II. Since the radioactive half-life of  $^{68}\text{Ge}$  is 271 days, the event rate is considered to be stable during a RUN. The expected  $\gamma$ -ray from the source is a 1077 keV  $\gamma$ -ray, whose emission ratio is about 1% of the  $\beta^+$  decays. The 1077 keV  $\gamma$ -rays are made use of to calibrate the energy scale of detectors.

The  $^{68}\text{Ge}$  source is sandwiched between two sheets of plastic scintillators (NE102). The scintillators are  $200 \mu\text{m}$  thick for each. The light of the scintillator is collected by a cone made of aluminized mylar ( $25 \mu\text{m}$  thick) and 1/2-inch photomultiplier (H3165P-10VT) to trigger the  $\beta^+$  events. Owing to the relatively high endpoint of the positron source, about 80 % of the positrons path through the scintillator and the aluminized mylar without being absorbed. On the other hand, half of the positrons are too energetic to stop in the target material and they will immediately annihilate on the wall of the assembly. To suppress these events, 1 mm thick cylindrical plastic

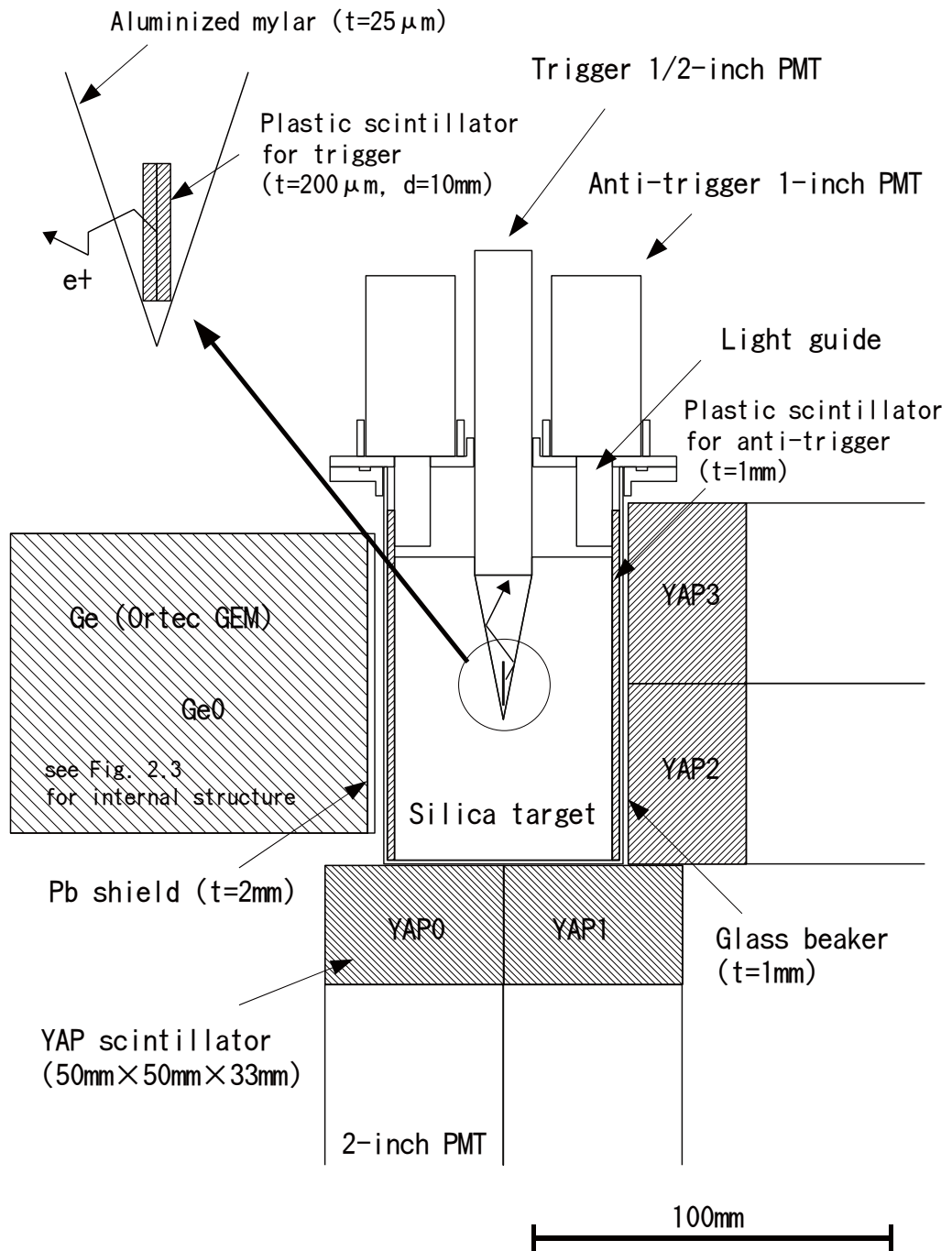


Figure 2.2: Schematic diagram of apparatus (side view).

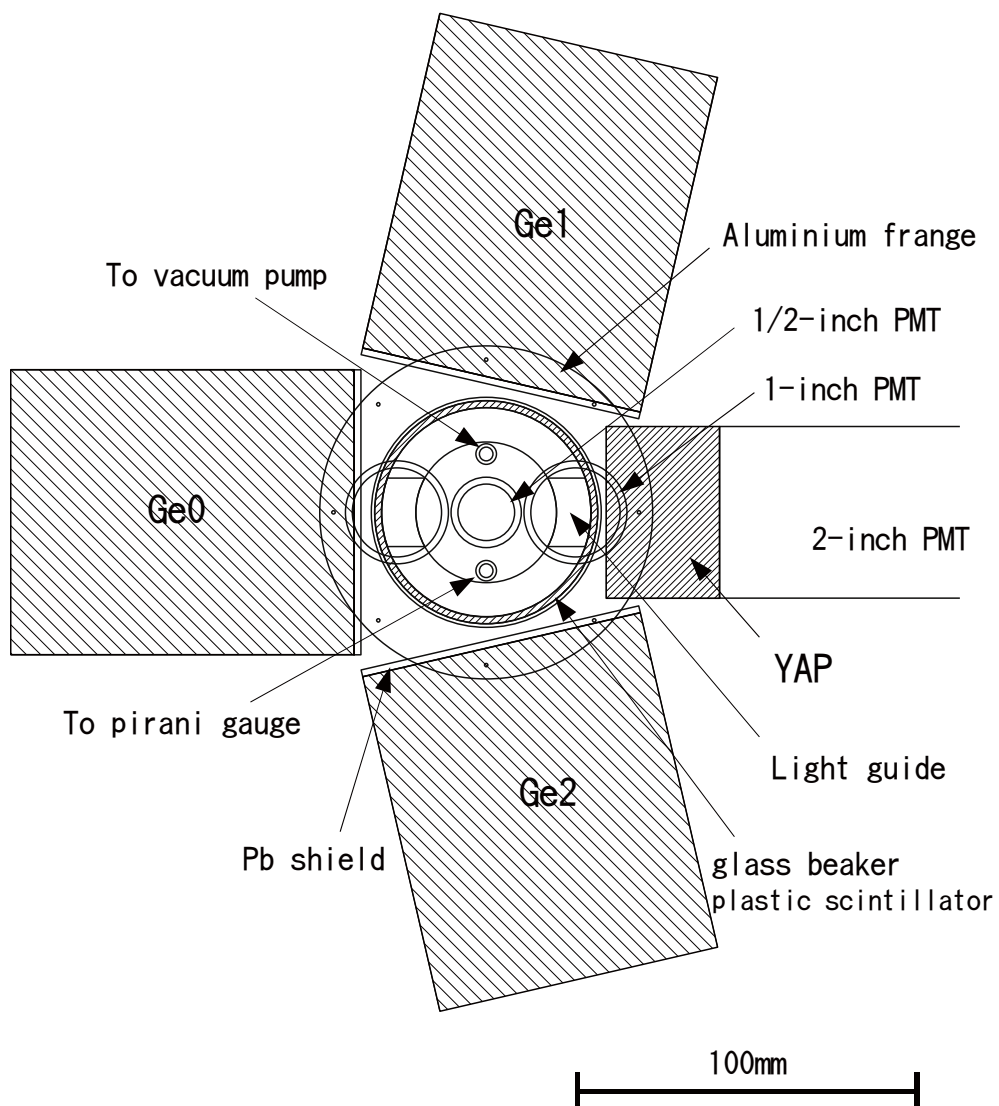


Figure 2.3: Schematic diagram of apparatus (top view).

scintillator is placed on the surface of the wall. The light of the scintillator is collected by the two 1-inch photomultiplier (R1924P) and gives the anti-trigger signal to kill the trigger signal.

The assembly container is made of a 1 *mm* thick glass beaker, whose diameter and height are 67 *mm* and 110 *mm* respectively. This container is filled with silica aerogel (RUN I) or silica powder (RUN II). The characteristics of these materials are discussed in the next section.

The assembly container is evacuated to  $6 \times 10^{-2}$  *mbar* by a rotary pump (EDWARDS E2M5), which is connected to the one of the two holes on top of the assembly. The other hole is connected to the pirani gauge to monitor the pressure of the container. Though  $O_2$  in the air has the unpaired electron spins and easily convert the o-Ps into the p-Ps by spin-exchange collisions, the effect is also corrected in the direct pick-off correction method. The pick-off rate of o-Ps in 1 *atm* of oxygen was observed to be about  $35 \mu s^{-1}$  [44], and one can expect  $4.2 \times 10^{-4} \mu s^{-1}$  increase of decay rate. This corresponds to  $\lambda_{pick}/\lambda_{3\gamma} = 0.006\%$ , which is much smaller than silica pick-off rate.

Due to the Zeeman effect, the mixing between the o-Ps and the p-Ps can occur in the presence of a magnetic field. The absolute strength of magnetic field around the positronium formation assembly is measured with 3-Axis Hall Gaussmeter [45] to be  $0.5 \pm 0.1$  *gauss*. This feeble field hardly contributes to the mixing of the two states, and estimated to be  $3 \times 10^{-11}$  [46].

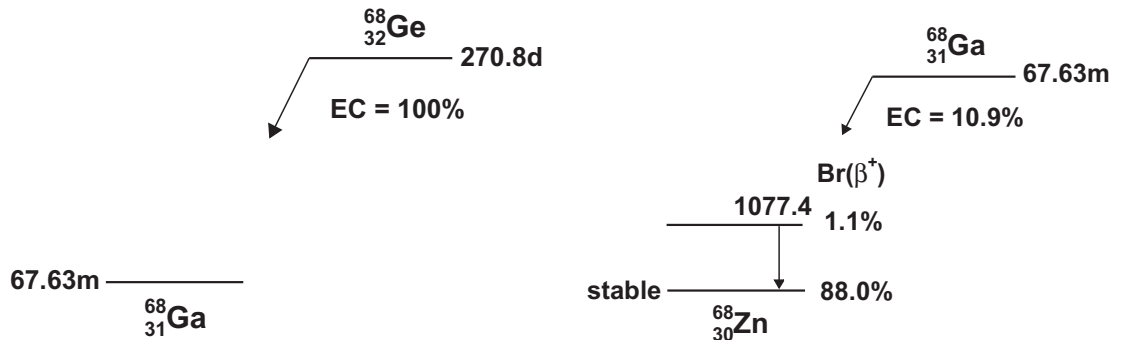


Figure 2.4: The level diagram of the  $^{68}\text{Ge}$  isotope. The  $^{68}\text{Ge}$  nucleus decays to the  $^{68}\text{Ga}$  nucleus through the electron capture (left diagram). Then, the  $^{68}\text{Ga}$  nucleus decays to the  $^{68}\text{Zn}$  nucleus through the  $\beta^+$  decay (right diagram).

### 2.3.2 Characteristics of SiO<sub>2</sub> Powders

In this experiment, two types of SiO<sub>2</sub> materials are used as a target. The one type is silica powder provided by Nippon Aerosil Ltd.. The silica powder consist of the primary silica grain, whose size is about 16nm. The primary grains generally form the group and the groups form the higher class of group. Then, the aggregate structure reached the size of several  $\mu\text{m}$ . The silica powder is originally hydrophilic and the grain is covered by the hydroxyl groups (-OH). But the company provides hydrophobic products whose hydroxyl groups are substituted with the tri-methyl-silyl groups (-Si - (CH<sub>3</sub>)<sub>3</sub>) in hydrophobic processing. it is better to use the hydrophobe rather than the hydrophile since the water on the surface of the grain surely increase the pick-off annihilation probability. In this experiment, to remove a water absorbed at the surface of grains, the SiO<sub>2</sub> powder is heated for 4 hours long in 130 °C just before evacuation of the container.

The other type of silica material is silica aerogel, which is a solid material and not powder state. In the silica aerogel, a chain-like aggregation of the silica makes 3-dimensional network structure. The 0.03g/cm<sup>3</sup> silica aerogel is provided by the Matsushita Electric Works Ltd.. The hydrophobic processing is also applied to the silica aerogel used in the measurement.

The characteristics of two silica materials are summarized in Table 2.1.

	Powder	Aerogel
Grade (code name)	R972CF	SP-7
primary grain size (nm)	16	10
surface area (m <sup>2</sup> /g)	110 ± 20	unknown
density (g/cm <sup>3</sup> )	0.035	0.03
mean distance (nm)	660	480
process	hydrophobe	hydrophobe

Table 2.1: Characteristics of two powders used in the measurement

The surface area of the grain is estimated by the BET (Brunauer, Emmett, and Teller) method which utilizes the physical adsorption of nitrogen gas on the surface of SiO<sub>2</sub> powders [47]. The mean distance between the grains  $\bar{L}$  has been calculated with the assumption of uniform size and spacial distributions of the grains as,

$$\bar{L} = \frac{4}{3} \left( \frac{\rho_0}{\rho} - 1 \right) R \quad (2.9)$$

where  $\rho_0$  is the bulk density of amorphous silica (2.20 g/cm<sup>3</sup>),  $\rho$  is the density of the powder, and  $R$  is the mean radius of the primary grains. Because the pick-off rate is proportional to the collisional frequency between the o-Ps and the grains, it strongly depends on the mean distance  $\bar{L}$ .

### 2.3.3 Detectors

In this experiment, two types of  $\gamma$ -ray detectors are used. One type is the germanium semiconductor detector (Ge), and the other is the YAP scintillator. Ge detectors, which has excellent energy resolution, are used to precisely determine the pick-off ratio  $\lambda_{pick}(t)/\lambda_{3\gamma}$  as a function of time. YAP scintillators, which have good time resolution, are used to obtain the time spectrum of the o-Ps decay. Three germanium detectors are used throughout two RUNs, while three (four) YAP scintillators are used for RUN I (II).

#### Germanium detectors

The germanium detectors used in the measurement are the P-type high-purity coaxial germanium detectors (Ortec GEM 38195-P-plus series).

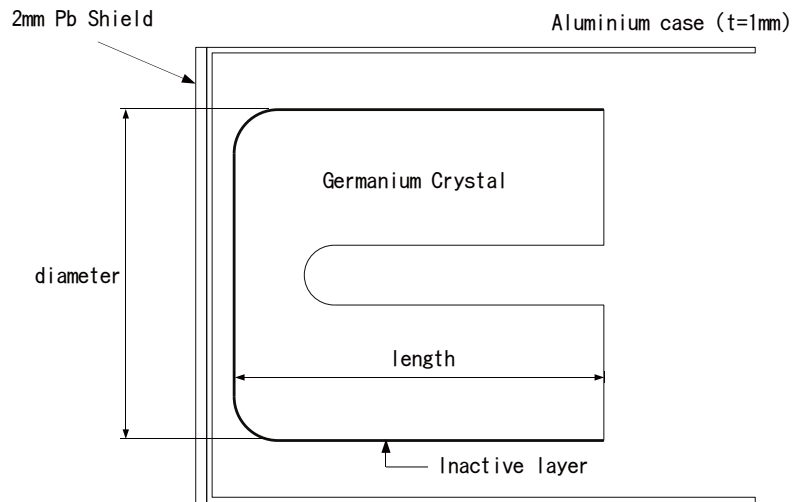


Figure 2.5: Internal structure of germanium detector.

The design of Ge detectors is shown in Fig. 2.5, where the size of crystals are bit different between the individuals and the values are summarized in Table 2.2. The lithium-diffused layer which is denoted as inactive volume in Fig. 2.5 has been formed over the outer surface of crystal. The layer is about  $700 \mu m$  thick. The arrangement of the three Ge detectors is shown in Fig. 2.2. From now on, they are referred to as Ge0, Ge1 and Ge2 as in the figure.

The energy resolutions are measured at several energy points by using line- $\gamma$  peaks from the  $\gamma$ -ray sources:  $^{152}\text{Eu}$ ,  $^{137}\text{Cs}$  and  $^{85}\text{Sr}$ . These values

	Ge 0	Ge 1	Ge 2
Serial Number	28-TP 10070	28-TP 10096	45-TP 22020A
Length(mm)	73.8	67.4	48.5
Diameter(mm)	58.3	60.3	68.5

Table 2.2: Crystal size of germanium detectors

are fitted with linear function as in Fig. 2.6, and used for smearing of the energy spectrum of the Monte Carlo simulation.

Throughout the measurement,  $2mm$  thick lead sheet is placed in front of the detector as seen in Fig. 2.5. It suppress the small energy photons, which pile up and disturb the energy spectrum around 511 keV.

The relative peak efficiencies with the lead shield are measured using  $^{152}\text{Eu}$ .  $^{152}\text{Eu}$  has various line- $\gamma$  peaks and their relative strength are well known and can be found in the data sheets [48]. On the other hand, the efficiencies are estimated by the Monte Carlo simulation implemented with the same geometry. As shown in Fig. 2.7, the measurement and the simulation shows a good agreement throughout the whole energy range.

The solid angles from the point source are about 3.4%, 3.5% and 4.7% (of  $4\pi$ ) for Ge0, Ge1 and Ge2 respectively.

### YAP scintillators

YAP ( $\text{YAlO}_3$ ) scintillator is a fast inorganic scintillator, whose characteristics are summarized in Table 2.3 [49, 50]. The YAP scintillators used in the measurement are  $50mm \times 50mm \times 33mm$  large crystal made in Czech Republic. The crystals are lapped by aluminized mylar and black sheet ( $200 \mu m$  thick). Then, they are connected 2-inch photomultipliers (R329-02). Four YAP detectors are arranged as in Fig. 2.2, though the YAP3 had not been deployed in RUN I. Their solid angles are 4.9%, 4.9%, 6.6% and 4.8% (of  $4\pi$ ).

The energy resolutions are measured using line- $\gamma$  peaks from several  $\gamma$ -ray sources:  $^{113}\text{Sn}$ ,  $^{85}\text{Sr}$ ,  $^{137}\text{Cs}$ . These values are summarized in Table 2.4.

### 2.3.4 Timing system

The timing system is an essential part of the experimental setup and the non-linearity of the TDC directly affects the final result.

Among the various types of TDC, the direct clock count type is suitable for this experiment. This is because,

- This type of TDC counts a constant frequency oscillator during the input time period. Then, the integral non-linearity (INL) is the order of the oscillator's precision and generally small ( $\sim 10^{-6}$ ).

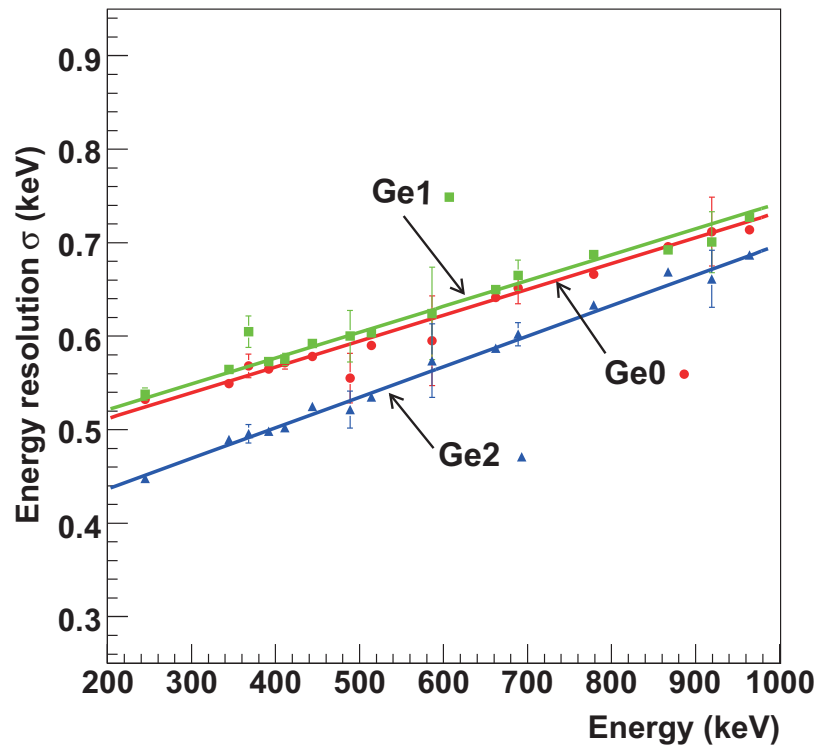


Figure 2.6: The energy resolution of the Ge detectors as a function of the  $\gamma$ -energy. Energy resolution is expressed as the one standard deviation in keV unit. Obtained functions are, for Ge 0 :  $\sigma = 0.457(1) + 0.276(2) \times 10^{-3} \times E(\text{keV})$ , for Ge 1 :  $\sigma = 0.466(1) + 0.276(3) \times 10^{-3} \times E(\text{keV})$ , for Ge 2 :  $\sigma = 0.371(1) + 0.327(2) \times 10^{-3} \times E(\text{keV})$

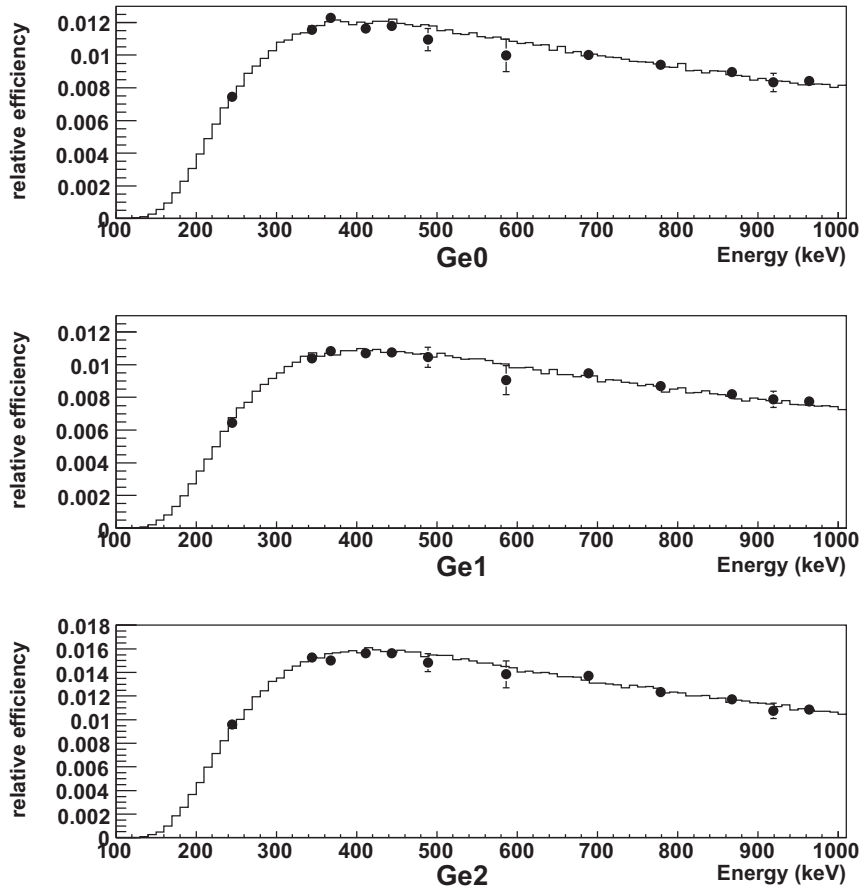


Figure 2.7: The relative peak efficiency of the germanium detectors. Measured data using the  $^{152}\text{Eu}$  source are plotted with closed circles as a function of  $\gamma$ -ray energy. The continuous line represent the relative efficiencies estimated with the Monte Carlo simulation. The data is normalized so as to fit the simulation.

name	YAP (YAlO <sub>3</sub> )
dope	cerium (Ce)
atomic number (Z)	39
density	5.37 g/cm <sup>3</sup>
emision peak	370 nm
light output	40 % of NaI
decay constant	30 ns
refractive index (n)	1.95
absorption length	15~20 cm

Table 2.3: Properties of YAP scintillator

Source	Energy (keV)	Resolution in $\sigma$ (keV)			
		YAP0	YAP1	YAP2	YAP3
<sup>113</sup> Sn	391.7	27.3	30.8	27.8	31.3
<sup>85</sup> Sr	514.0	33.3	33.0	34.3	34.9
<sup>137</sup> Cs	662.0	39.2	41.2	39.4	47.4

Table 2.4: Energy resolution of the YAP scintillator

- The differential non-linearity (DNL) is caused by the transitions of the flip-flops and typically the order of 1 %. But, the DNL has a periodical structure as  $2^n$  (n=1,2,3...) interval and rapidly decreases in the longer range.

Considering the above situation, the new direct clock count type TDC was developed at the previous measurement [38] with the exhaustive cooperation of the staffs of an Electronics Facility of High Energy Accelerator Research Organization (KEK). The main features of the new TDC are as follows.

- A direct clock count type TDC with 8 ch LEMO inputs. The TDC is a kind of 16 bit counter and the time range is determined by the external clock source, which is connected through a SMA connector on the front panel.
- The external clock source is a DDS-PLL synthesizer, DPL-2.5G (Digital Signal Technology Inc.). The DPL-2.5G utilize Direct Digital Synthesis (DDS) and Phase Locked Loop (PLL) techniques, which are explained below. For the present measurement, the frequency of the DPL-2.5G is adjusted to 2 GHz. Therefore, the time range of the 16 bit TDC is 32  $\mu$ s. The stability of the internal clock frequency is guaranteed as  $\pm 2.5$  ppm against the temperature  $-10$  °C  $\sim$  50 °C and  $\pm 3$  ppm against one year.

- The differential non-linearity of the TDC is  $0.4 \sim 0.5 \%$  for 2 bin width and  $0.1 \sim 0.2 \%$  for 4 bin width. But the time walk correction and the rebinning operation in the analysis totally smear the DNL.

### Phase Locked Loop (PLL)

The Phase Locked Loop (PLL) is a circuit whose output is locked (synchronized) on the input oscillator. The PLL consists of phase comparator, loop filter and voltage controlled oscillator (VCO) as shown in Fig. 2.8. At first, the phase comparator detects the phase difference between the input signal and the loop-backed signal. Then, the frequency of the output signal is adjusted in the VCO according to the detected phase difference. That is to say, the frequency of the output signal follows that of the input signal with some time constant. With this mechanism, the rapid change of the input frequency and the noise component is totally eliminated and the output frequency is highly stabilized. Another block, the loop filter is a low pass filter which eliminate a ripple on the signal and also determine the time constant of the PLL. The frequency of the output signal can be changed by the divider or the mixer inserted in the loop-backed circuit.

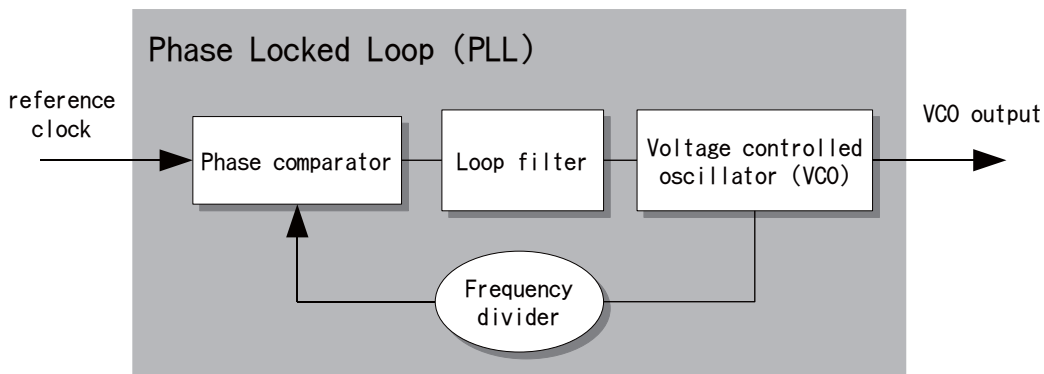


Figure 2.8: Schematic diagram of Phase Locked Loop (PLL).

### Direct Digital Synthesis

Though the frequency of the PLL is variable, the large factor of the division distorts the signal shape and the fine adjustment of the frequency is also difficult. To achieve the high purity and the fine adjustable frequency, the Direct Digital Synthesis (DDS) is

introduced. The DDS consists of the several parts as described in Fig. 2.9. The signal shape is prepared in advance as the Look up table on the memory. Then the Digital Analog Converter (DAC) and the some filters reconstruct the signal shape. The frequency is determined by the Accumulator which adds the adjusted value at every clocks. The output of the accumulator addresses the Look up table, which represents the phase of the signal.

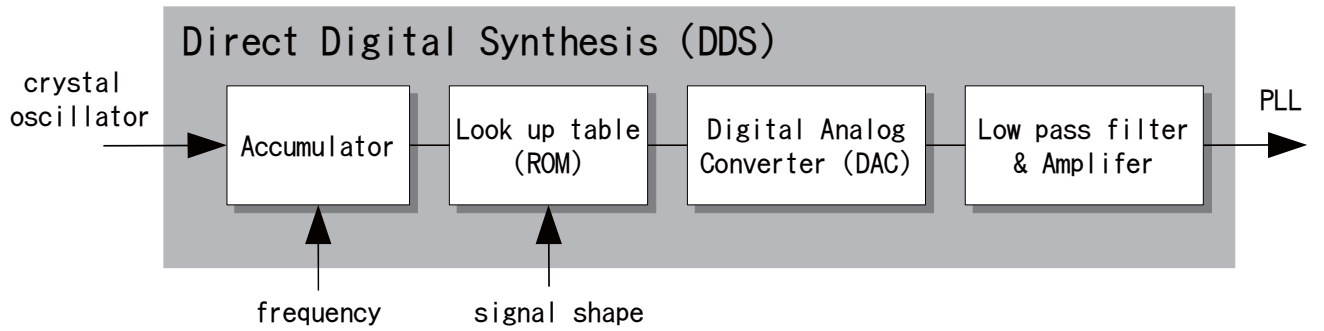


Figure 2.9: Schematic diagram of Direct Digital Synthesis (DDS)

The frequency of the clock is adjusted to 2 GHz within 1 *ppm* accuracy before the measurement. Since the TDC is a direct clock count type and principally miscount never occurs, the integral non-linearity is expected to be less than 15 *ppm* corresponding to the bin width.

### Effect of the smearing operation

The detector resolution and the analysis operation such as the time walk correction are considered to be smearing operation with the gaussian function. The exponential function and the flat distribution do not change its slope in the convolution operation with the gaussian function as,

$$\int_{-\infty}^{\infty} N \exp(-\lambda t') \cdot \frac{1}{\sigma\sqrt{2\pi}} \exp\left(-\frac{(t-t')^2}{2\sigma^2}\right) dt' = N \exp\left(-\frac{\sigma^2\lambda^2}{2}\right) \exp(-\lambda t) \quad (2.10)$$

Therefore, the smearing operation does not affect the measured decay rate. Note that the fast periodical structure such as the intrinsic differential non-linearity of the TDC is dropped in the smearing operation.

### Effect of the binning operation

When the exponential distribution is filled in the histogram, the content of the bin ( $t - \Delta t/2 \sim t + \Delta t/2$ ) is expressed as,

$$\int_{t-\Delta t/2}^{t+\Delta t/2} N \exp(-\lambda t') dt' = \frac{N}{\lambda} \left( e^{-\lambda(t-\Delta t/2)} - e^{-\lambda(t+\Delta t/2)} \right) \quad (2.11)$$

$$\sim N \exp(-\lambda t) \left( \Delta t + \frac{1}{24} \lambda^2 \Delta t^3 \right) \quad (2.12)$$

while the value of the function is  $N \exp(-\lambda t)$  at the center of the bin. Thus the binning operation is considered to be the change of the normalization, which is independent of the point  $t$ . Therefore, the binning operation does not affect the measured decay rate.

### 2.3.5 Electronics

#### Data flow

The data acquisition system of the experiment consists of the clusters of NIM standard modules and the CAMAC system. Fig. 2.10 shows the data-flow of the total system. The system mainly consists of three part, the trigger part, the YAP part, and the Ge part. Each part has a *latch veto* structure where the system accepts the first signal and immediately sets the latch by itself to block the second signal. Thus, only one trigger signal is produced for each event cycle. The latch of the trigger part, denoted as the *Main latch* in the figure, is released by a pulse from the output register module of CAMAC system. The latches of the YAP and Ge parts, denoted as the *Sub latch* in the figure, are released by the latch reset signals from the trigger part.

The trigger part also generates the start signal for the TDC and the each  $\gamma$ -ray detector stops the TDC to record the detection time. The energy information is also recorded with the ADCs for each detector. The gate signals for these ADCs are made by the corresponding detector signals, not by the trigger signal. The following three ADC gates are prepared for each signal.

- **Wide gate** which is enough wide to cover the signal. The energy information of the signal is measured with the Wide gate.
- **Base gate** which is set prior to the signal. The baseline condition is measured with the Base gate.
- **Narrow gate** which is narrower than the Wide gate and covers the peak of the signal. The energy difference of the Wide gate and Narrow gate is used to reject the pile-up events.

Details of the data-flows and the modules are described for each part.

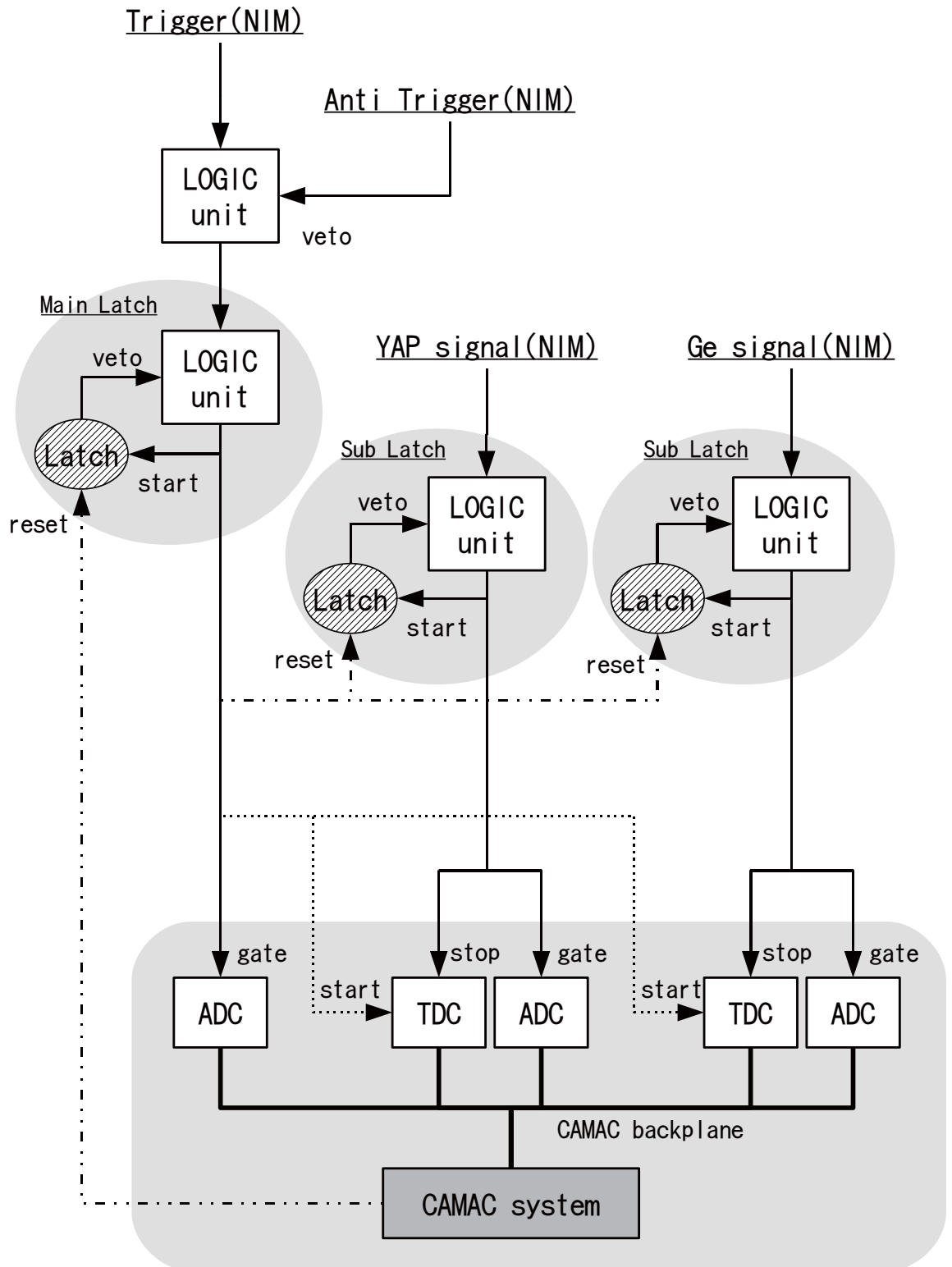


Figure 2.10: Schematic diagram of the process data-flow.

### Trigger system

A schematic diagram of electronics for the trigger part is shown in Fig. 2.11. The following explanations enumerated by the indices are corresponding to the label within Fig. 2.11.

- (t.0) The trigger PMT is operated at -1160V and the two anti-trigger PMT is operated at -1160V and -1110V respectively. These high voltages are supplied by a negative high voltage module Repic RPH-031.
- (t.1) The output of the trigger PMT are divided into three signals by a linear fanout module. One signal is sent to a discriminator to produce the trigger signal. The other two signals are fed into a charge sensitive ADC denoted as Trig ADC (LeCroy 2249A), through delay cables. The Trig ADC measures the amplitude of the trigger PMT signal and the baseline condition just before the signal, which is referred to as Wide and Base from now on.
- (t.2) The amplitude of the signal is about  $-50\text{ mV}$  for a typical energy deposit of 50 keV. The threshold value is fixed at  $-12\text{ mV}$  and more than 90 % of  $\beta^+$  events are triggered.
- (t.3) The outputs of the two anti-trigger PMTs are summed in a linear fanin fanout module and used as a veto signal for the trigger logic. The amplitude of the signal is about  $-150\text{ mV}$  for a typical energy deposit of 200 keV and the threshold value is fixed at  $-40\text{ mV}$ . About a half of the positrons pass through the silica target and almost all of them produced the anti-trigger signals. In fact, the counting rate is decreased by half at the logic unit.
- (t.4) Only when the veto signal is not imposed, the trigger signal passes through the logic unit. The margin of the timing between these two signals is  $20\text{ ns}$ .
- (t.5) One output signal of the logic unit is used to set the main latch to inhibits the succeeding trigger signals. This main latch is released by the CAMAC controller at the beginning of the event cycle. Another output is used as the start signal for the main TDC. This TDC is often called as KEK TDC since KEK and our group jointly developed it as the 2 GHz clock count type TDC.
- (t.6) One of the output signals from the logic unit provides the gate signal for the Trig ADC. The gate width is set to be as narrow as  $50\text{ ns}$ . This is required for the reason that the ADC value correlates the pile-up activity within the gate width, and the time walk correction or cut by this value results in disturbing the time spectrum of the accidental events.

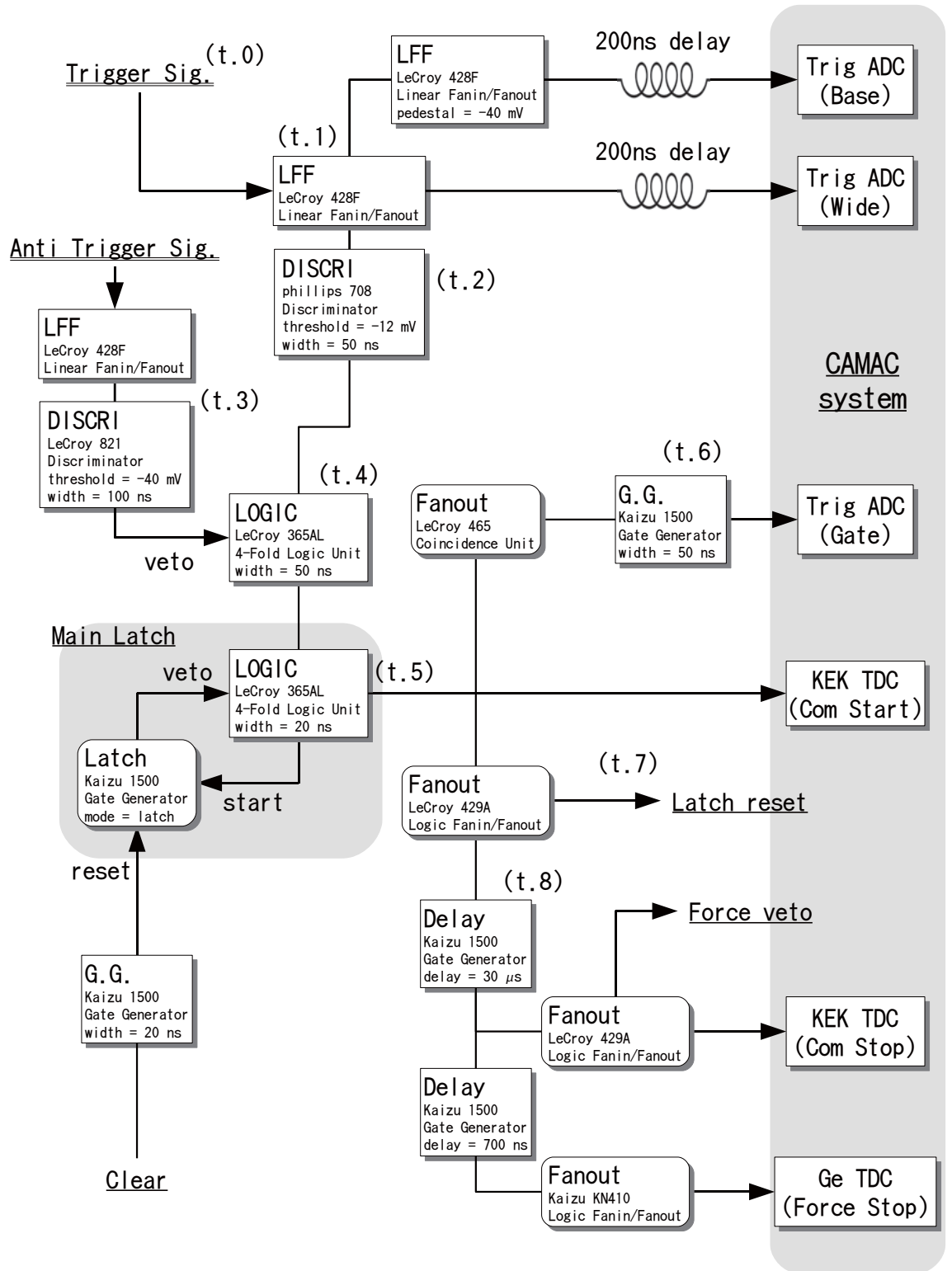


Figure 2.11: Schematic diagram of electronics for trigger system.

- (t.7) The trigger signals are distributed to all the systems as the latch reset signals. The latch reset signal is as narrow as 20 ns since the longer reset signal may block the latch set signal when the signal comes just after the release of the veto signal.
- (t.8) At the end of event cycle, the force veto signals are distributed to set all the latches by force. In addition, some other signals are distributed to stop all the TDCs.

### Electronics for the YAP scintillators

A schematic diagram of electronics for a YAP scintillator part is shown in Fig. 2.12. The logic described in the figure is for just one YAP system. Three systems are prepared for RUN I and four systems for RUN II corresponding to the number of YAP scintillators used. As in the description of the trigger part, the following indices are corresponding to the labels in Fig. 2.12.

- (y.0) The photomultipliers for the YAP scintillators are operated around -1.7kV. These high voltages are supplied by a negative high voltage module Repic RPH-031.
- (y.1) The output of the YAP PMT is divided into four lines by a linear fanout module. One of the divided signals is fed into a discriminator. The others are used to measure the amplitude of the signal (Wide) and the baseline condition (Base). The amplitude of the signal is also measured by the narrower gate, which is referred to as Narrow, since the difference to the longer gate is sensitive to the pile-up activity. For the measurements of YAP Narrow and YAP Wide, the charge sensitive ADC (phillips 7167) is used, which is denoted as YAP ADC in the figure.
- (y.2) The pulse-height of the 511 keV signal is about 0.5 V. The threshold value is set to 70 mV, which is enough high to reject after pulse signals. The noise level is far below the threshold.
- (y.3) The baseline condition of the signal line is measured at the time just before the YAP signal (Base), which is performed by the charge sensitive ADC denoted as Base ADC (phillips 7167). In addition, the baseline condition is also measured at the timing of the prompt ( $T_0$ ) by the Trig ADC. The signals for the baseline measurements are amplified by a factor of 2.5. This is because the resolution of the Base ADC value is originally as narrow as ADC bin width.
- (y.4) The output of the discriminator is delayed by 100 ns in order to wait the latch reset signal from the trigger part and fed into the logic unit. The force veto signal from the trigger part is ORed in the logic unit and the latch will be set by force at the end of event cycle.

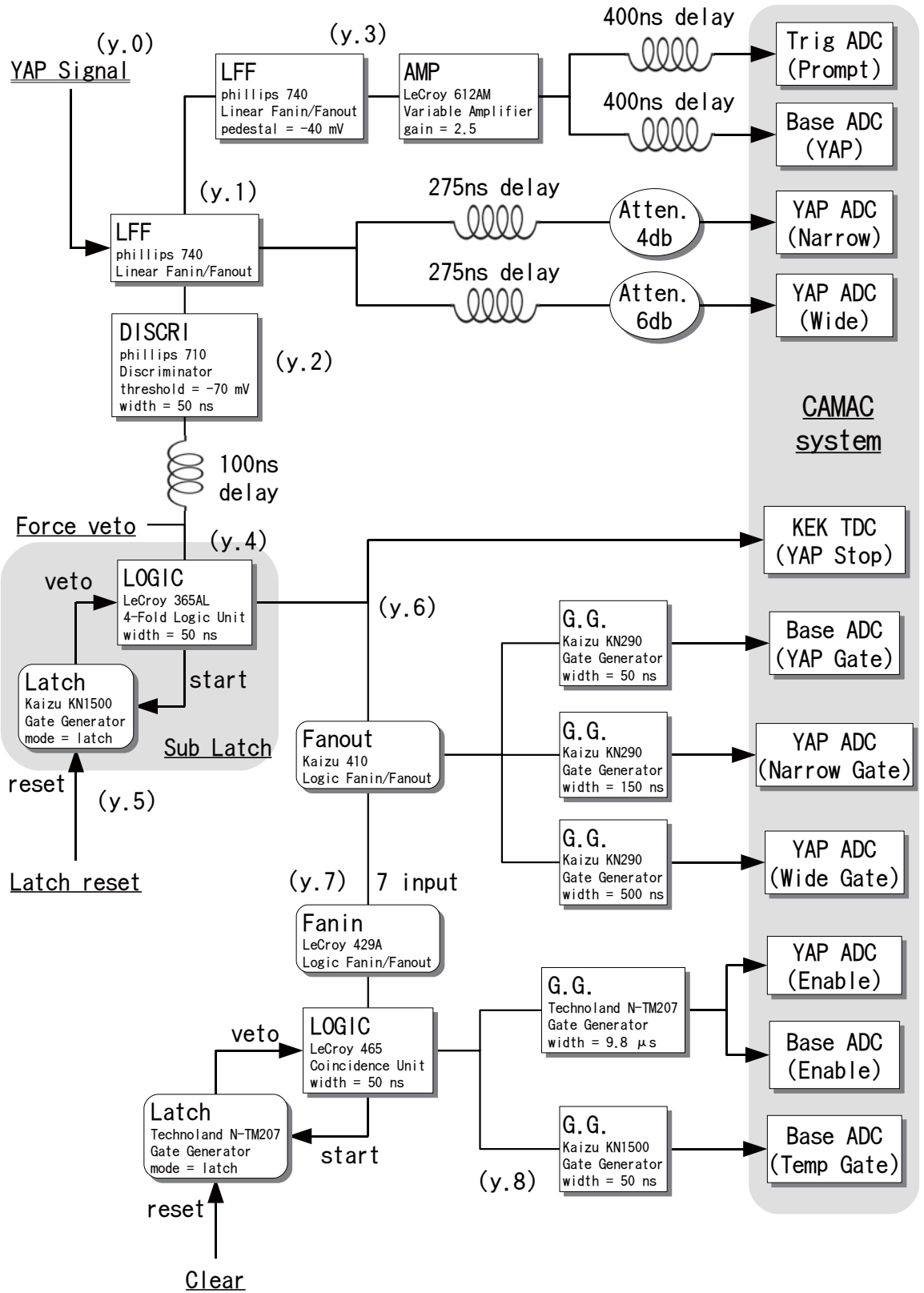


Figure 2.12: Schematic diagram of electronics for YAP scintillator system.

- (y.5) The YAP part has its latch mechanism which prevent the double trigger in a event cycle. This latch will be released by a logic signal from the trigger part.
- (y.6) One of the output from the logic unit provides the stop signal for the KEK TDC. The others are used to make the gate signals for the YAP ADC and the Base ADC. The gate widths of the Base, Narrow and Wide are 50 ns, 150 ns, and 500 ns respectively.
- (y.7) The phillips 7167 ADC has individual gate for the each input signal and the enable signal which covers all the gate signals is required to make the gates active. Therefore, the timing signals of all the detectors are fed into a fanin module and its output is used to produce the enable signal.
- (y.8) The enable signal is also used to generate the gate signal for the temperature measurement.

### Electronics for the germanium detectors

This section explains the electronics for a Ge detector section. The schematic diagram is shown in Fig. 2.13.

- (g.0) The bias voltages are supplied by the bias supply modules (EG&G ORTEC 459) through the HV buffers (SEIKO EG&G DS-1550). The HV values are +2600 V for Ge0, +2000 V for Ge1, and +3500 V for Ge2.
- (g.1) The pre-amplifier (or FET) of Ge detector provides the two identical signal outputs. The one of the pre-amplifier outputs is sent to a spectroscopy amplifier (EG&G ORTEC 673). The time constant of the shaping time is 6  $\mu s$ . The output of the amplifier is fed into a peak hold ADC (hoshin C011) for the measurement of the energy (Wide).
- (g.2) The another output is fed into a timing-filter amplifier (EG&G ORTEC 474). The time constants of the differentiation and integration are set to be 500 ns and 20 ns respectively. The analog outputs of the timing-filter amplifier are used for the measurements of the baseline condition (Base) and the amplitude (Narrow), and fed into the Base ADC and the Ge ADC (phillips 7167) respectively.
- (g.3) The outputs of the fanout module are fed into a discriminator to generate the timing signals. The three threshold values (30 mV, 50 mV, 150 mV) are imposed to measure the risetime of the Ge signal. These timing are recorded by the Ge TDC (Repic RPC-061) prepared for each Ge detector. The timing signal discriminated by 50 mV threshold is also sent to the logic unit as the trigger signal.

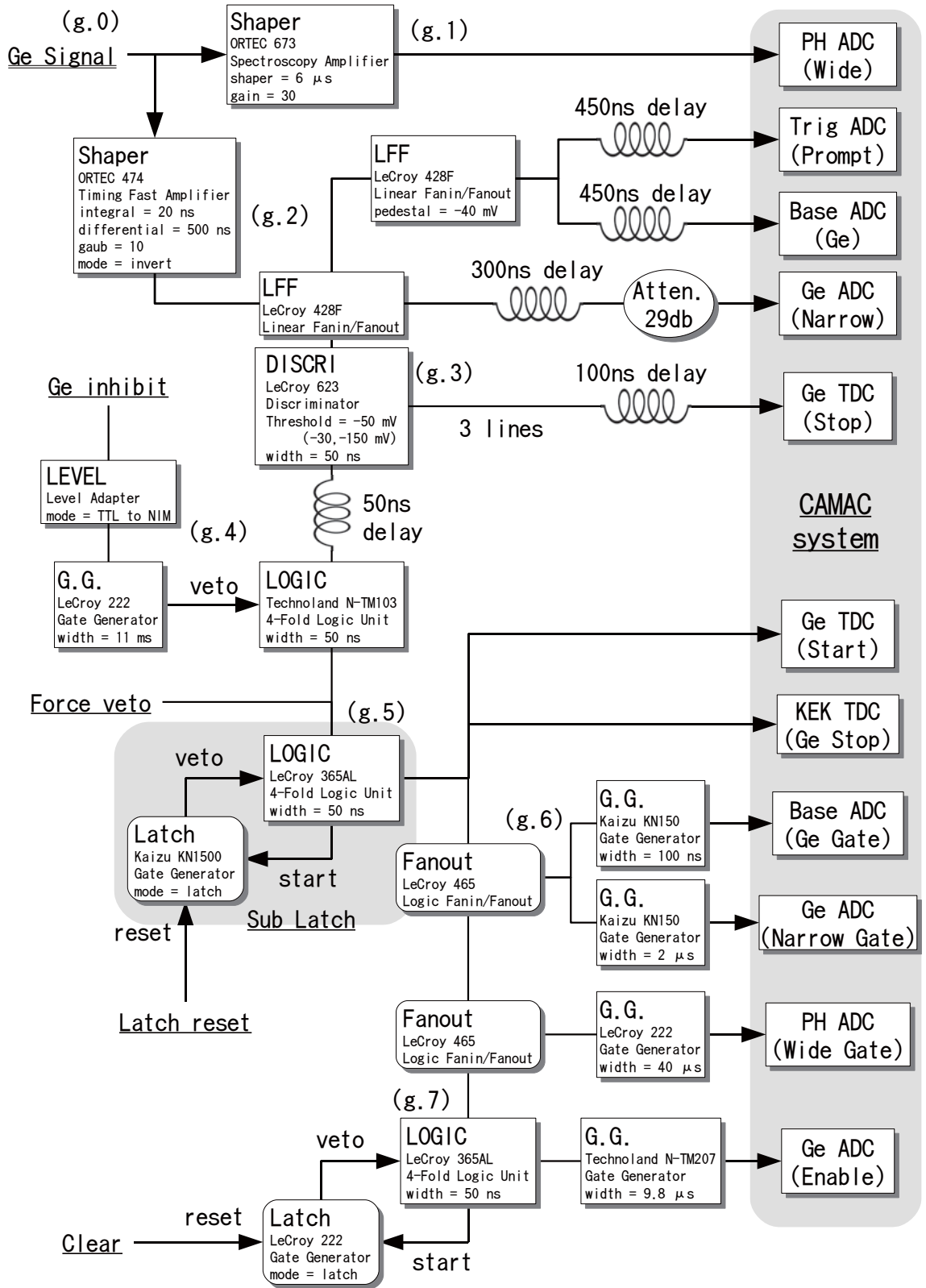


Figure 2.13: Schematic diagram of electronics for Ge detector system.

- (g.4) The pre-amplifier is a transistor reset type amplifier, which releases the collected charges periodically, and the timing of the transistor reset is provided as the transistor reset pulse (TRP). The TRP is about 10 Hz and it disturbs the signal lines for a while. Therefore, the inhibit signal is used to veto the electronics of the Ge systems for  $11ms$ .
- (g.5) The trigger logics such as the latch mechanism and the force veto are the same as in the YAP part. The one of the outputs provides the stop signal for the KEK TDC. The another output provides the start signal for the Ge TDC.
- (g.6) Just like the case in the YAP part, Base gate, Narrow gate, and Wide gate are prepared. The widths are  $100\text{ ns}$ ,  $2\ \mu s$  and  $40\ \mu s$  respectively.
- (g.7) The Ge ADC is also a individual gate type ADC and it requires the gate enable signal. Then, the timing signals of the Ge detectors are ORed in the logic unit and the output is provided as the enable signal.

### Electronics for the temperature measurement

The room temperature is measured with the temperature sensor IC (LM35DZ). The output of the sensor is connected to the ADC (phillips 7167). Then, the level of the voltage is measured with  $50\text{ ns}$  ADC gate as shown in Fig. 2.12 (y.8).

### 2.3.6 The CAMAC Data Acquisition System

Data acquisition is performed with the CAMAC system. The CAMAC system on the CAMAC Crate (Toyo Corp. PS7500) is controlled by the CAMAC Crate Controller CC/NET (Toyo Corp). The CC/NET is implemented as a single board computer where the Linux OS debian (ver. 3.1) is installed and the data taking program runs on it. The data read from the CAMAC modules are compressed and stored as ROOT files (ver. 5.04 [51]) on the other NFS host machine.

The procedures of data taking is as follows. At first, all the CAMAC modules are cleared by the logic signal from the output register (Technoland C-RP202), which is triggered by the controller. Then, the main latch is released by the reset signal in the same manner. This makes all the systems active and the controller waits the interrupt signal, so-called LAM (Look-At-Me) signal from the KEK TDC. The interrupt signal starts the data reading procedures for the KEK TDC. If no detector hits within the  $10\ \mu s$ , the data is simply discarded and the controller proceeds to the next event cycle. But if there is any hit, the controller read all the data from the ADCs and the TDCs. After the reading procedures, the controller starts the next

event cycle by distributing the clear and latch reset signals to the system, and then saves the data through NFS.

The measured quantities and the used CAMAC modules are summarized in Table 2.5, 2.6, 2.7.

conventional name	module	gate width
Pla Wide	LeCroy 2249A (AC)	50 <i>ns</i>
Pla Base	LeCroy 2249A (AC)	50 <i>ns</i>
Ge Wide	hoshin C011 (AC)	40 $\mu s$
Ge Narrow	phillips 7167 (AC)	2 $\mu s$
Ge Base	phillips 7167 (DC)	100 <i>ns</i>
YAP Wide	phillips 7167 (AC)	500 <i>ns</i>
YAP Narrow	phillips 7167 (AC)	150 <i>ns</i>
YAP Base	phillips 7167 (DC)	50 <i>ns</i>
temperature	phillips 7167 (DC)	50 <i>ns</i>

Table 2.5: Quantities measured with ADCs

conventional name	module
Ge Timing	KEK TDC
YAP Timing	KEK TDC
Ge $T_{30\ mV}$	Repic RPC-061
Ge $T_{50\ mV}$	Repic RPC-061
Ge $T_{150\ mV}$	Repic RPC-061
	phillips 7186 for Ge2

Table 2.6: Quantities measured with TDCs

## 2.4 Monte Carlo Simulation

### 2.4.1 Positron and Photon Simulation

A Monte Carlo simulation plays a crucial role in this experiment. Its main purposes are,

- The accurate  $3\gamma$  energy spectrum of the Ge detector is required to separate the pick-off contribution from the measured spectrum.
- The accurate detection efficiencies for both Ge detector and YAP scintillator are required. The ratio of the  $3\gamma$  detection efficiency ( $\epsilon_{3\gamma}$ ) and the pick-off  $2\gamma$  detection efficiency ( $\epsilon_{pick}$ ) is used in the analysis.

module	bits	full range	comments
KEK TDC	16	32 $\mu s$	direct clock count type (2 GHz)
Repic RPC-061	12	1 $\mu s$	successive comparison type
phillips 7166	12	800 $ns$	successive comparison type
LeCroy 2249A	11		Wilkinson type
phillips 7167	12		successive comparison type
hoshin C011	12		Wilkinson peak-holding type

Table 2.7: Specifications of the CAMAC modules

- Some of the systematic errors are estimated with the Monte Carlo simulation.

For the detector simulation, the Geant4 (ver. 8.0) package [43, 52] is used and the details of the present experimental setups are reproduced in the simulation. In this package, the interactions of the positron and the  $\gamma$ -ray in various materials are implemented. Practically, the Low Energy Electromagnetic Physics Library of the Geant4 package is used for the simulation. In this original library, binding effect of Compton scattering is not yet implemented. Therefore, the extra package called Low-Energy Compton Scattering package (G4LECS ver. 1.06) [53] is introduced.

The Monte Carlo simulation is proceeded as follows. At first, a positron is emitted from the source with the energy corresponding to the energy spectrum of  $^{68}\text{Ge}$ , which is reported in some articles [54, 55]. Then the interactions of the positron in the materials are simulated step by step, ionisation, bremsstrahlung, etc. The simulation of the secondary particles is also included in this process. Some of the positrons are absorbed in the trigger plastic scintillator or other materials in the positron formation assembly. But the positrons stopped in the silica target are selected as the candidate for o-Ps.

The next step is the simulation of the  $\gamma$ -rays emitted from o-Ps. For the simulation of the pick-off annihilation, two  $\gamma$ 's with the energy of 511 keV are emitted from the point where the positron stopped in the positron simulation. Three  $\gamma$ 's from the o-Ps decay are also generated in the same manner, but their direction and energy are calculated from the  $O(\alpha)$  matrix element [19]. Then, the interactions of all the  $\gamma$ -rays and their secondary particles are simulated step by step, photoelectric effect, Compton scattering, Rayleigh scattering, etc.

In the end, the energies deposited on various detectors are obtained for the o-Ps decay and the pick-off annihilation respectively. The effects of the anti-trigger and the trigger threshold is negligible, though the events where the positrons or their secondary electrons hit the anti-trigger have wider distribution of the decay point. The obtained energies are smeared by the measured resolutions and the response functions of the corresponding

detectors.  $3.6 \times 10^9$  events of the o-Ps  $3\gamma$  decay are generated for each RUN.

### 2.4.2 Response Function of the Ge Detector

The response function of Ge detector is measured by 514 keV single energy  $\gamma$ -ray of  $^{85}\text{Sr}$  source. The assembly beaker is replaced by the  $^{85}\text{Sr}$  source and the trigger signal is produced by the detector signal itself. The Fig. 2.14 is the comparison of the measured energy spectrum and the Monte Carlo simulation. The environmental background of the measured spectrum is subtracted by the spectrum taken without  $^{85}\text{Sr}$  source. The two spectra are in good agreement with each other except for the region around the photoelectric peak. The observed tail of the photoelectric peak comes from the charge incollection in the germanium crystal. The amount of the tail is about 1% of the photoelectric peak and depends on an individual crystal to be precise. Therefore, the response functions of three Ge detectors are individually measured as in Fig. 2.15. The difference is fitted with exponential function and the function is used for the smearing of the Monte Carlo data. Before the fitting, the slow rise-time events are eliminated by the SRT cut (see Sec. 3.1.5) with the same condition as in the analysis of the run. This is because these events are more likely to form the charge incollection tail.

Another factor that disturbs the energy spectrum is pile-up events. Since the pile-up effect is dependent on the event rate and the energy of the  $\gamma$ -ray, it is evaluated with the data taken for the decay rate measurement in this experiment. Fig. 2.16 shows the right side of the 511 keV photoelectric peak of the data. Since the Narrow-Wide cut, which is explained later, rejects the energy deviation beyond  $\pm 15$  keV, the pile-up tail of the photoelectric peak extends up to 525 keV. The amount of the tail is dependent on the detector hit rate and typically 1 % of the photoelectric peak. The pile-up tail is fitted with exponential plus flat function. The events used for the fitting is restricted within  $\pm 20$  ns, where the simultaneous hits of  $3\gamma$  is negligible and the background events are simply subtracted with the flat function. The obtained exponential function is used as a part of the response function.

### 2.4.3 Response Function of the YAP Scintillator

The response function of YAP scintillator is also measured by  $^{85}\text{Sr}$  source. The upper plot of the Fig. 2.17 is the comparison of the measured energy spectrum and the simulation. The background is subtracted by the spectrum taken without  $^{85}\text{Sr}$  source as in the Ge case. The difference comes from the non-uniform collection efficiency of optical photon in the YAP crystal. The non-uniformity of the efficiency is enhanced by the short absorption length of optical photon in the YAP crystal, which is reported as about 20 cm [49]. The relative collection efficiency is evaluated by the optical photon simulation using the Geant4 package. The simulation only consider

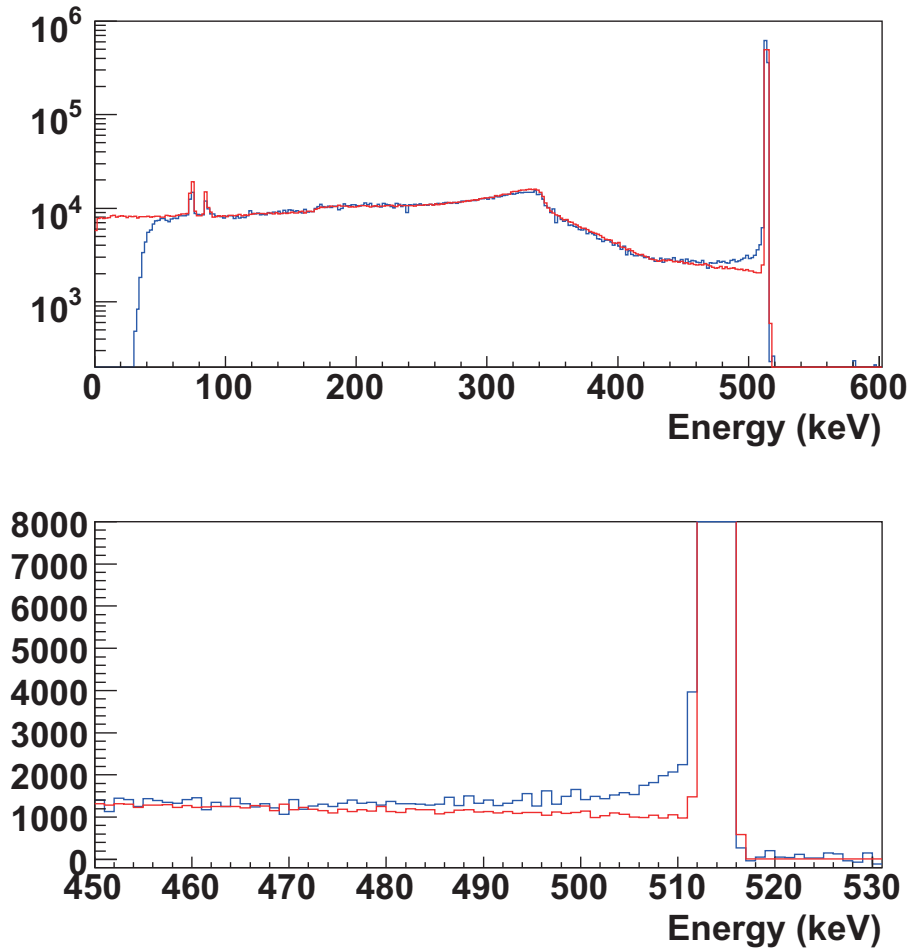


Figure 2.14: Comparison of the measured Ge spectrum with the simulation using  $^{85}\text{Sr}$  source. The blue line is the measured spectrum and the red line is the spectrum generated by the Monte Carlo simulation. The two spectra are in good agreement with each other except for the region around the photoelectric peak. The lower figure is the enlarged spectrum around the photoelectric peak. The exponential tail is observed below the photoelectric peak.

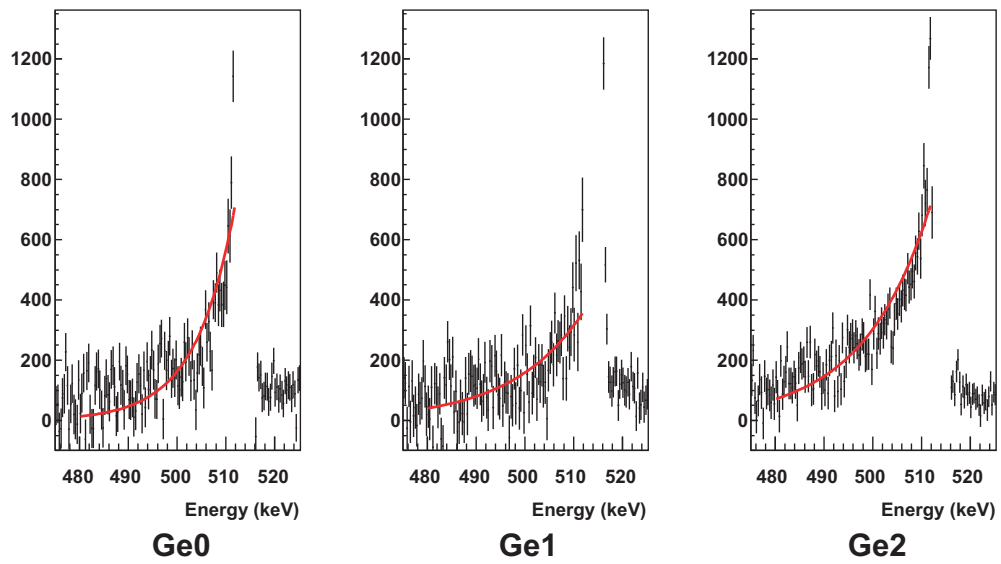


Figure 2.15: The difference of the measured Ge spectrum and the simulation. The tails of the photoelectric peaks are fitted with exponential functions. The amount of the tails are 1.1% for Ge0, 1.0% for Ge1, and 2.0% for Ge2.

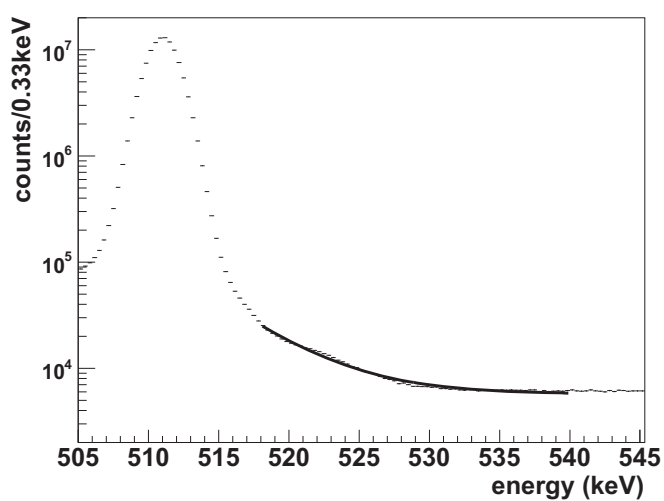


Figure 2.16: Pile-up events of Ge detector. The pile-up events disturb the energy spectrum of Ge detector. Since the Narrow-Wide cut rejects the energy deviation beyond  $\pm 15$  keV, the pile-up tail of the photoelectric peak extends up to 525 keV. The amount of the tail is dependent on the event rate and typically 1 % of the photoelectric peak. The pile-up tail is fitted with exponential plus flat function for each run. Then, the exponential function is used as a part of the response function.

---

the absorption in the crystal and the reflection on the surface of the crystal. The region in a crystal is divided into  $2mm \times 2mm \times 1.5mm$  regions and the collection efficiency is evaluated for each region. It is found that the collection efficiency at the corner of YAP crystal is rather low by 40% at most, as shown in Fig. 2.18. The obtained efficiency is incorporated into the  $\gamma$ -ray simulation and the non-gaussian response function is reproduced. In the end, the simulation is in good agreement with the measured spectrum as shown in the lower plot of the Fig. 2.17.

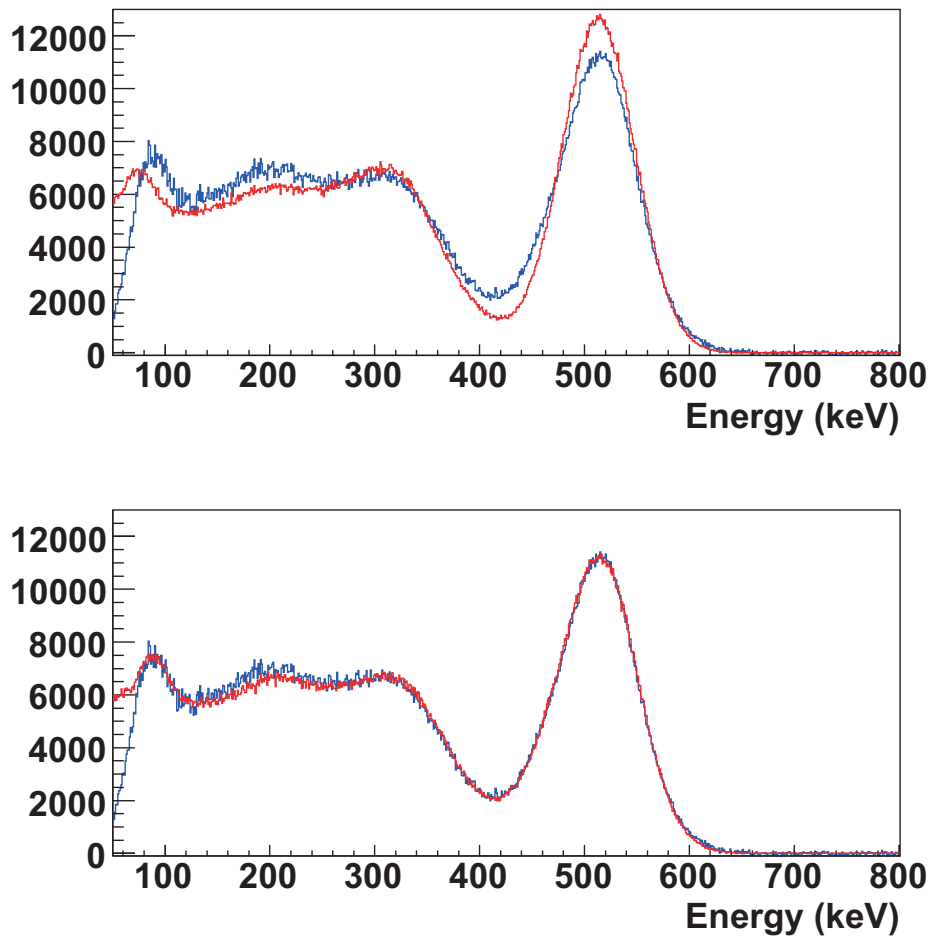


Figure 2.17: Comparison of the measured YAP spectrum with the simulation using  $^{85}\text{Sr}$  source. The blue line is the measured spectrum and the red line is the spectrum generated by the Monte Carlo simulation. The difference is observed especially in the shape of photoelectric peak (the upper figure). The simulation with non-uniform photon collection efficiency reproduces the measured spectrum (the lower figure).

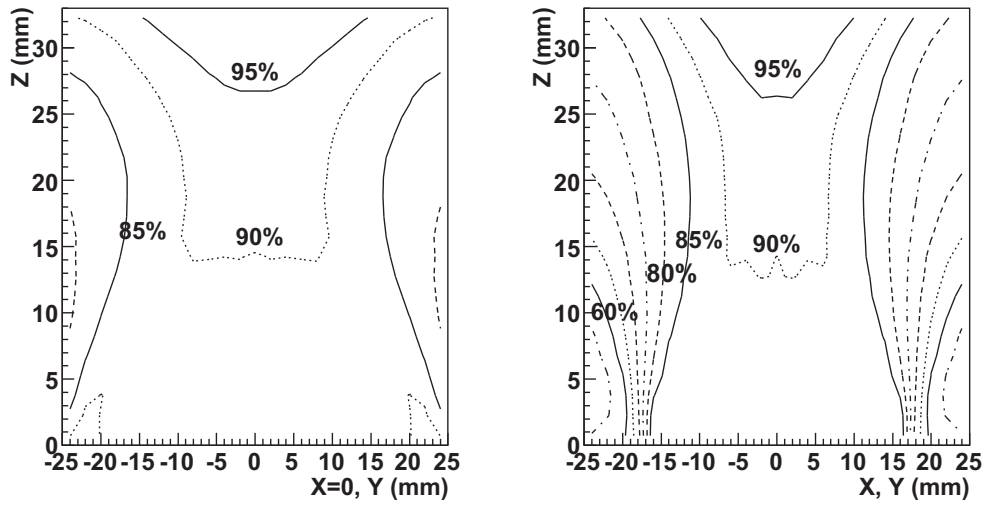


Figure 2.18: Collection efficiency of optical photon in YAP crystal. The left figure shows the collection efficiency along the Y axis on the center of crystal ( $X=0$ ). The right figure shows the collection efficiency along the diagonal direction of X-Y plane. The photomultiplier is connected on the lower side of X-Y plane ( $Z=0$ ).

# Chapter 3

## Analysis

In this chapter, the details of the analysis are described. Calibration, several cuts and time walk correction are explained in the first section. Then, the detailed description of the direct pick-off correction method will follow. The last section contains a discussion of the systematic errors accompanying the measurement. The various procedures in this chapter are explained for RUN II since most of the parts are common to two RUNs.

### 3.1 Calibration and Time Walk Correction

#### 3.1.1 Data Sets

The two RUNs have been performed in this experiment. Some properties of the two RUNs are summarized in Table 3.1. Most of the parts are the same, but the types of the silica target are different. The silica aerogel is used in the RUN I, whereas the silica powder is used in the RUN II.

During the RUNs, data are taken with the CAMAC system. Totally about  $1.4 \times 10^{10}$  events and  $1.6 \times 10^{10}$  events are taken for RUN I and RUN II respectively. Only when the  $\gamma$ -detectors detect any  $\gamma$ -rays within  $10\mu s$  from the  $\beta^+$  trigger, data are stored in the disk storage. Totally about  $5.7 \times 10^9$  events and  $6.6 \times 10^9$  events are recorded for RUN I and II respectively. The net data taking periods are about 2.3 month for RUN I and about 3.1 month for RUN II. Typical  $\beta^+$  trigger rates before anti-trigger veto system are 10.8 kHz for RUN I and 6.8 kHz for RUN II.

Data are stored into the multiple calibration units for every  $6 \times 10^7$  events. The calibration and the time walk correction are carried out within one calibration unit. Since the data taking time for one unit is about 6 hours, it is guaranteed that the fluctuation and the shift of the measured quantities by the environment do not propagate over that time scale.

During the measurements, the temperature of the experimental area was controlled within  $\pm 0.5$  °C to suppress the fluctuation of the measured quantities.

name	period	rate	events	target	detectors
RUN I	2.3 month	10.8 kHz	$1.4 \times 10^{10}$	silica aerogel	Ge $\times$ 3, YAP $\times$ 3
RUN II	3.1 month	6.8 kHz	$1.6 \times 10^{10}$	silica powder	Ge $\times$ 3, YAP $\times$ 4

Table 3.1: Properties of the RUNs

### Dependence on the event rate

There are two factors dependent on the event rate, the probability of the accidental event and the probability of the pile-up event. However, the following procedures in the analysis totally eliminate its propagation to the final result.

- The accidental flat distribution is directly fitted in the decay rate fitting. Then the probability of the accidental event does not affect the final result.
- The pile-up rejection cut is applied and the pile-up events are eliminated. The effect of the contamination is taken into account as a small modification of the energy response function (see Sec.2.4.2).
- The time spectrum of the later time region is slightly suppressed by the first hit condition of the data taking system. The deviation is dependent on the detector hit rate and taken into account in the fitting function (see Eq.3.8).

Though the event rate does not affect the final result, the systematic error of the pick-off correction is determined by the amount of the accidental events and the event rate should be as low as possible. In addition, the time range of decay curve region depends on the accidental level. In the present measurement, the range of the decay curve is about five times lifetime of o- $\text{Ps}$ .

### 3.1.2 Time and Energy Spectrum of the $\gamma$ -ray Detector

Before the details of the analysis is explained, the time and energy spectrum of the  $\gamma$ -ray detector is shown.

#### Spectrum of the YAP scintillator

Fig.3.1 shows the time and energy spectrum of the YAP scintillator. The time spectrum is already corrected by the time walk correction, which is explained in Sec.3.1.5. Due to the good time resolution of 1 ns, the time spectrum of the YAP scintillator is very clear. The time spectrum is composed of the following three regions.

- **prompt peak**

A sharp peak called as the prompt peak is observed at  $T_0(t = 0)$ . The prompt peak consists of the p-Ps,  $e^+$  annihilation and 1077 keV nuclei- $\gamma$ .

- **o-Ps decay curve**

The o-Ps decay curve is observed after the prompt peak. The decay time is about the lifetime of o-Ps and decreased by the pick-off contribution.

- **accidental events**

The flat distribution is observed after the o-Ps decay curve. These events consists of the accidental hits, that are not correlated with the  $\beta^+$  trigger.

On the other hand, the energy spectrum of the YAP scintillator is vague. But the energy information of the YAP scintillator is basically not required. The  $2\gamma$  spectrum of the  $e^+$  annihilation is dominant and some part of the spectrum is the  $3\gamma$  continuous spectrum.

### Spectrum of the Ge detector

Fig.3.2 shows the time and energy spectrum of the Ge detector. The time spectrum is already corrected by the time walk correction, which is explained in Sec.3.1.5. The time resolution of the Ge detector is larger than that of the YAP scintillator. But the resolution of 5 ns is good enough to extract the time dependence of the pick-off ratio.

On the other hand, the energy spectrum of the Ge detector is very clear and the resolution is about 0.5 keV around 511 keV photoelectric peak. Making use of the good energy resolution, the Ge detector can separate the pick-off  $2\gamma$  events from the  $3\gamma$  events.

### 3.1.3 Calibration

#### ADC spectrum of YAP scintillators and Ge detectors

The calibration of the ADC spectra has made use of the 511 keV positron annihilation line and the accompanying 1077 keV nuclei- $\gamma$ . Each peaks are fitted with normal gaussian function. Then, the fitted peak values are used to determine the energy scale of the ADCs. The Wide spectra and Narrow spectra are individually calibrated for both Ge and YAP detectors.

On the other hand, the absolute calibration is difficult for Base spectra. Therefore, the peak is fitted with normal gaussian and the standard deviation is used to define the scale of Base spectrum.

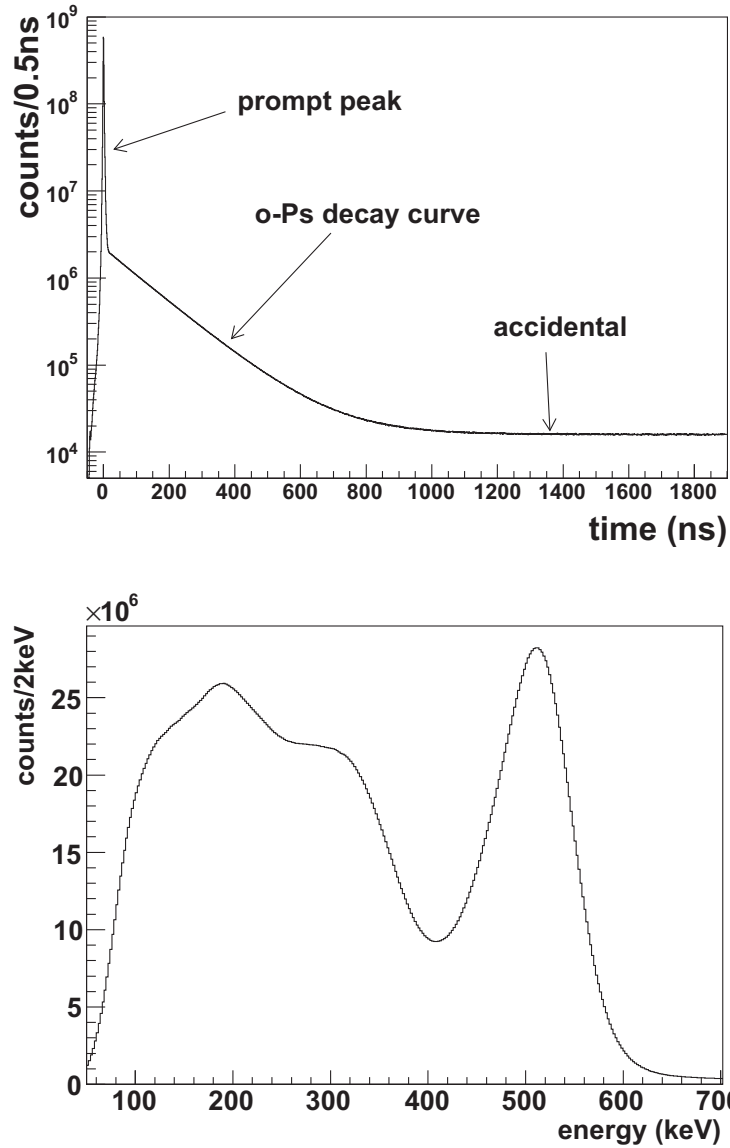


Figure 3.1: Time and Energy spectrum of the YAP scintillator. The upper figure is the time spectrum of the YAP scintillator. The energy range is restricted above 150 keV and the time walk correction is already applied. The lower figure is the energy spectrum of the YAP scintillator. The time window is restricted before 700 ns.

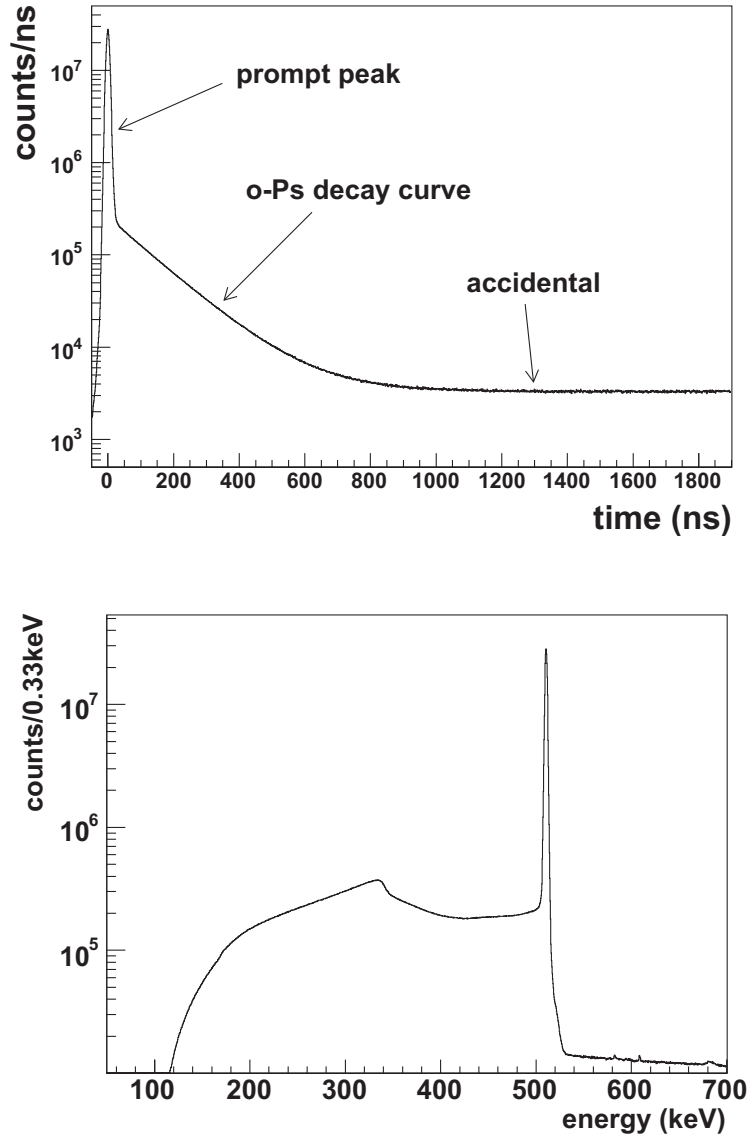


Figure 3.2: Time and Energy spectrum of the Ge detector. The upper figure is the time spectrum of the Ge detector. The energy range is restricted from 300 keV to 520 keV and the time walk correction is already applied. The lower figure is the energy spectrum of the Ge detector. The time window is restricted before 700 ns. The lower energy region is suppressed by the slow rise-time cut.

### TDC spectrum of YAP scintillators and Ge detectors

The absolute scale of the KEK TDC is determined by the external clock source. The 2 GHz clock leads to 0.5 ns bin width and 32  $\mu$ s full range. The calibration of the absolute value makes use of the prompt events which appears as a sharp peak and exactly stands at decay time  $t = 0$  ( $T_0$ ) since it consists of the p-Ps and 1077 keV nuclei- $\gamma$ . After the time walk correction, the prompt peak is fitted with normal gaussian and the absolute decay time is determined.

The differential non-linearity (DNL), which is the deviation of the relative bin width, is so small for the KEK TDC that the measured decay rate is not affected at all. But, the  $\chi^2$  of the decay rate fitting sums up the DNL and the minimum value is increased. To avoid this effect, the measured TDC values are smeared with the gaussian function which has 1.5 ns standard deviation.

Though the intrinsic DNL of the KEK TDC is negligible, the non-linearity of the time spectrum is observed at the DNL test where the random start signal and the stop signal of the clock are fed into the KEK TDC. As in Fig. 3.3, the 0.05-0.1 % excess of the relative bin width is observed near the  $T_0$ . It is found that the transition of the veto input in the logic unit causes the electric fluctuation of the output line and leads to the non-linearity of the time spectrum near the  $T_0$ . Therefore, the non-linearity is corrected by the relative bin width measured at the DNL test.

### ADC spectrum of plastic scintillator

The calibration of Wide spectrum for the plastic scintillator is not needed since no cut is applied for the spectrum. Wide spectrum is only used for the time walk correction within a calibration unit. On the other hand, Base spectrum of the plastic scintillator is calibrated by the standard deviation as in YAP and Ge cases.

#### 3.1.4 Event Selection

In order to extract the intrinsic timing of the  $\gamma$ -rays and the accurate energy of those, it is important to reject the pile-up event where the two or more  $\gamma$ -rays hit the detector successively. The two types of cut adopted in the measurement are explained in this section.

#### Base cut for Ge, YAP and the plastic scintillator

One type of the cuts is Base cut, which requires the clean baseline condition just before the signal. The Base cut rejects the events where the preceding signal disturbs the timing and the energy information of the succeeding

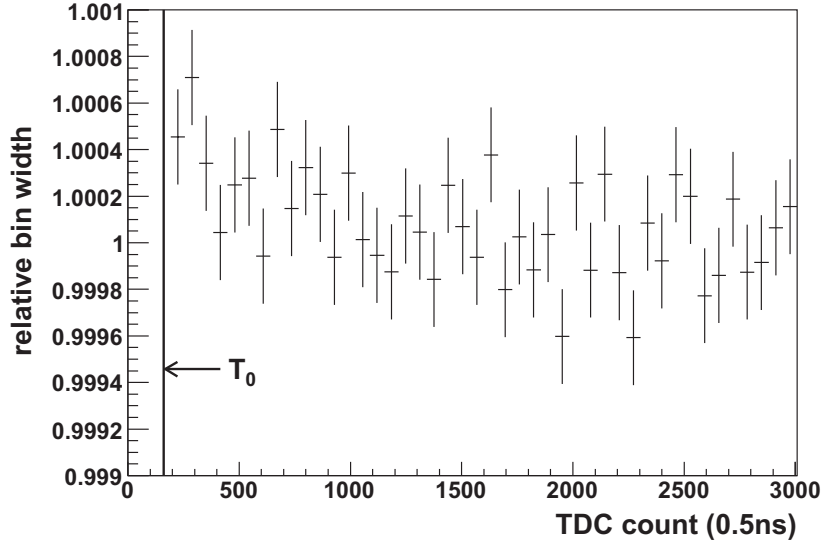


Figure 3.3: The relative bin width measured at the DNL test of the KEK TDC. The 0.05-0.1 % excess of the relative bin width is observed near the  $T_0$

signal as in Fig. 3.4. The events that are triggered by the tail of the detector signal are also gotten rid of.

The spectra of the Ge Base are shown in Fig.3.5. The slow rise-time events, which are explained later, are not included in the figures. The higher tail of the spectrum accounts for the pile-up events and the events triggered by the tail of the signal. The lower tail comes from the hits on the undershoot of the previous event. Thus, the events within  $\pm 4\sigma$  are selected as in the figure.

For the YAP scintillators, the time dependence of the cut efficiency affects the time spectrum. In fact, the prompt hits such as 1077 keV nuclei- $\gamma$  and bremsstrahlung- $\gamma$  of the positron deposit the energy in the Base gate of the delayed signal. If the Base cut  $\pm 4\sigma$  is applied, the events near the prompt are suppressed. In Fig. 3.6, these events are shown as the tail which extends to about  $140\sigma$ . Then, the upper boundary of the Base cut is set to  $140\sigma$ . The effect of the contamination is calculated in Appendix B and assigned as a systematic error.

The Base cut is also applied for the plastic scintillator. The events within  $\pm 4\sigma$  are selected as in Fig. 3.7.

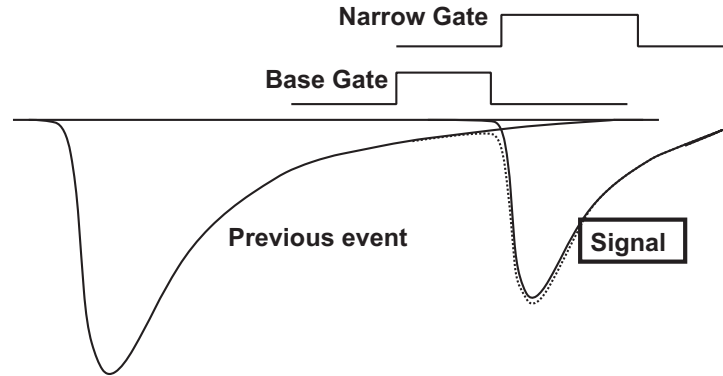


Figure 3.4: The schematic of the Base cut. The Base cut rejects the events where the preceding signal disturbs the timing and the energy information of the succeeding signal.

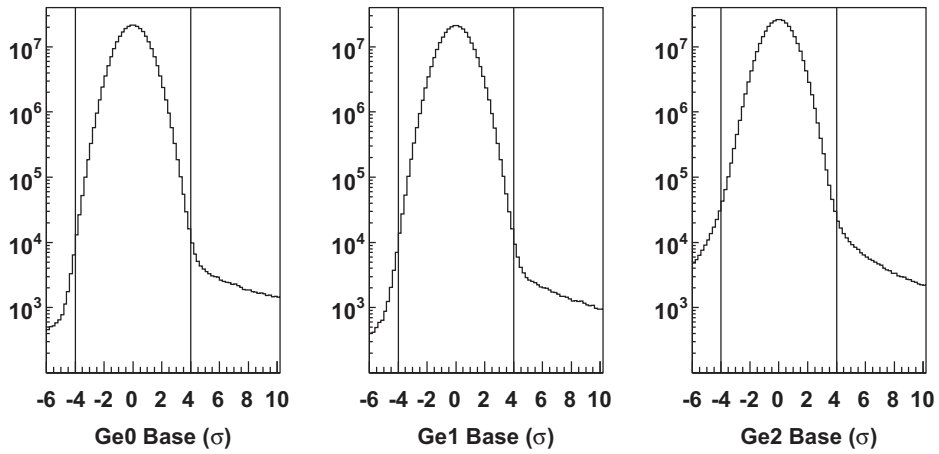


Figure 3.5: Base spectra for Ge detectors. The slow rise-time events are excluded in the figures. The events within  $\pm 4\sigma$  are selected. The two vertical lines in a figure show the boundaries of the cut.

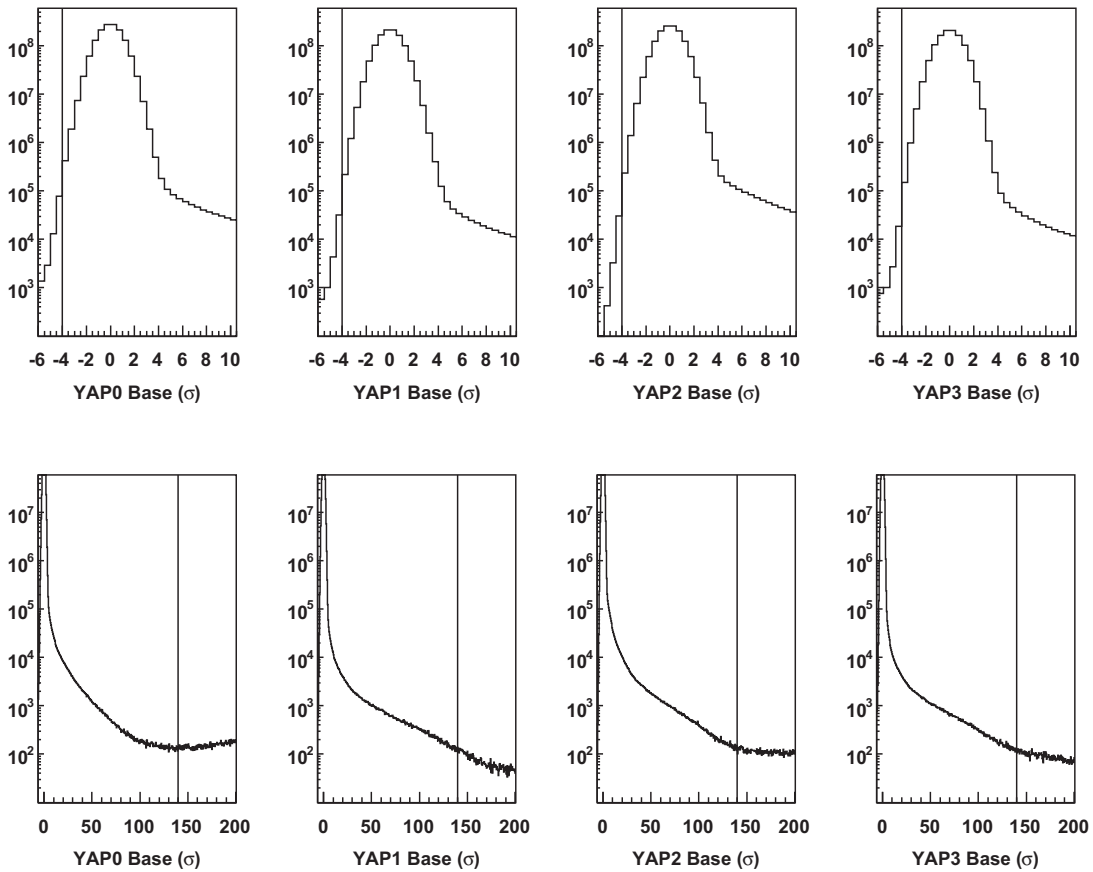


Figure 3.6: Base spectra for YAP scintillator. The events within the range from  $-4 \sigma$  to  $+140 \sigma$  are selected. The upper figures show the lower boundaries of the cut as the vertical line. The lower figures show the upper boundaries of the cut as the vertical line.

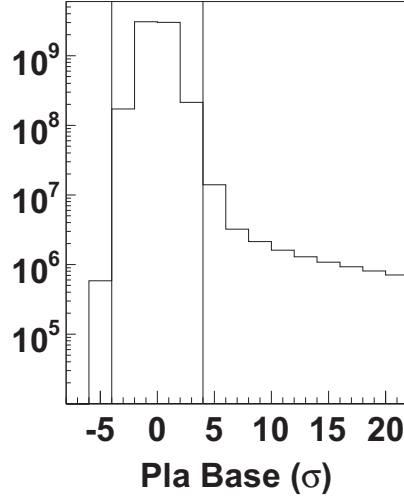


Figure 3.7: Base spectrum for the plastic scintillator. The events within  $\pm 4 \sigma$  are selected. The two vertical lines show the boundaries of the cut.

### Narrow-Wide (NW) cut for Ge and YAP

The other type of the cuts is Narrow-Wide (NW) cut, which requires the small difference of the energies measured with Narrow gate and Wide gate. The used quantity is Wide - Narrow in the keV unit. The NW cut rejects the events where the succeeding signal disturbs the energy information of the preceding signal as in Fig. 3.8.

The NW spectra for Ge detectors are shown in Fig. 3.9. The slow rise-time events, which are explained later, are not included in the figures. The higher tail account for the pile-up events. The events within  $\pm 15$  keV are selected as in the figure.

For the YAP scintillators, NW cut is also applied. The events within  $\pm 30$  keV are selected as in Fig. 3.10.

### 3.1.5 Time Walk Correction

The detection timings of the signals are depending on their amplitudes. This lag of time called walk must be corrected to obtain the intrinsic decay time. The following time walk corrections make use of the prompt events, which consist of the p-Ps and the  $e^+$  annihilation etc, and occur at  $T_0(t = 0)$ .

#### Time walk correction for YAP scintillator

Due to the fast rise-time feature of YAP scintillator, the time walk is as small as 2 ns if the energy is above 150 keV. The procedures of the time

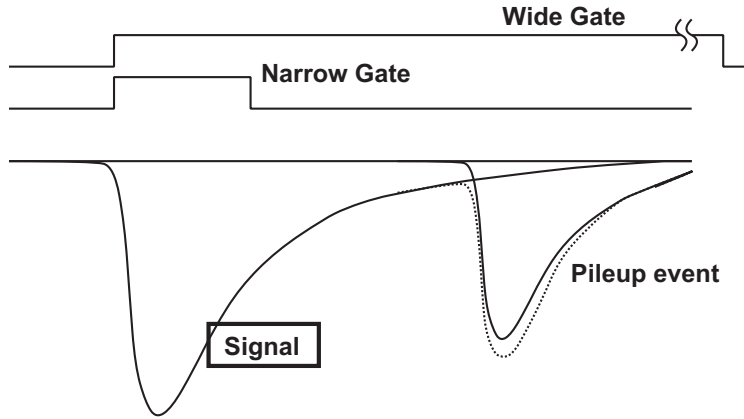


Figure 3.8: The schematic of the Narrow-Wide (NW) cut. The NW cut rejects the events where the succeeding signal disturbs the energy information of the preceding signal.

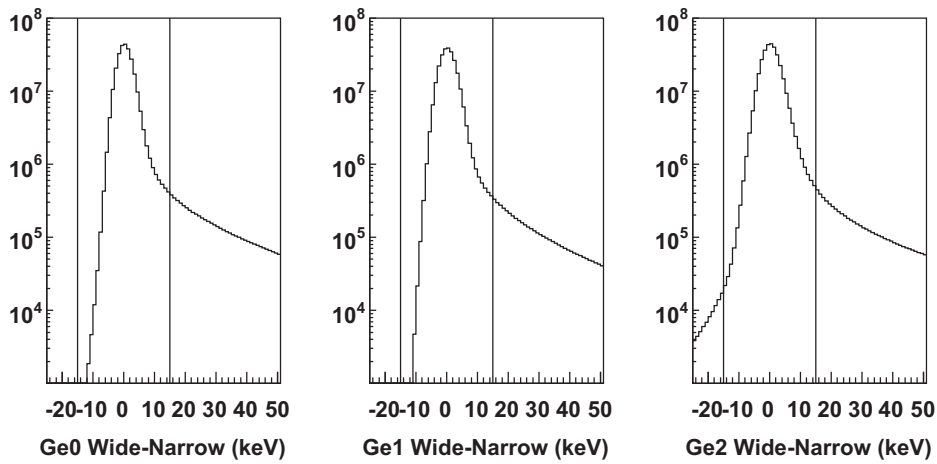


Figure 3.9: Narrow-Wide spectra for Ge detectors. The events within  $\pm 15$  keV are selected. The two vertical lines shows the boundaries of the cut.

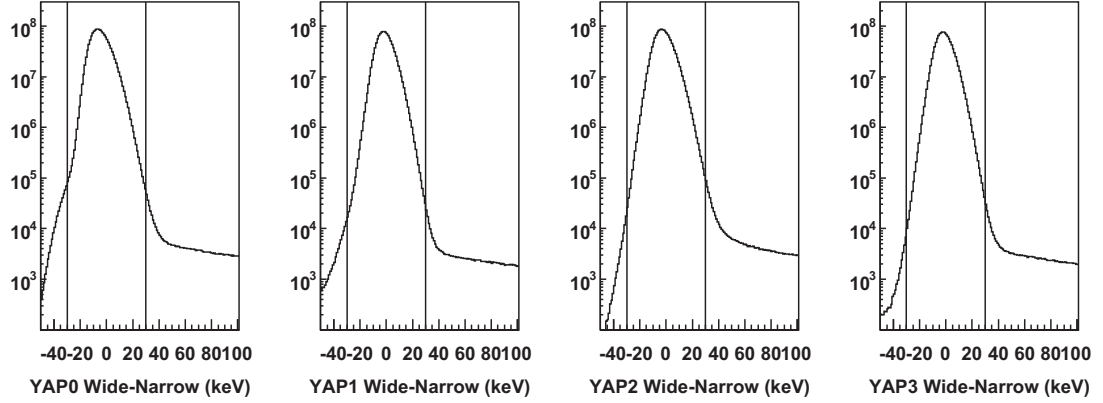


Figure 3.10: Narrow-Wide spectra for YAP scintillators. The events within  $\pm 30$  keV are selected. The two vertical lines show the boundaries of the cut.

walk correction for YAP scintillator are as follows. At first, the whole energy range is divided into the 50 keV width regions and the prompt peaks for these regions are fitted with normal gaussian. Then, the peak values are fitted with seven order polynomial function as in Fig. 3.11. The relative correction width is determined by this function at any energy. After the time walk correction, the excellent time resolution of 1.3 ns is obtained for the whole energy range above 150 keV.

### Time walk correction for plastic scintillator

In order to extract the time walk of the plastic scintillator, the prompt events of YAP scintillator is used. The energy region for YAP scintillator is restricted within  $\pm 100$  keV from 511 keV. Though the plastic scintillator has a fast rise-time signal, the time walk is clearly seen in Fig. 3.12. This is because the typical amplitude of the signal is just above the threshold. As in the YAP case, the whole Wide range of the plastic scintillator (Pla Wide) is divided into the 10 counts regions and the prompt peaks for these regions are fitted with normal gaussian. Then, the peak values are fitted with seven order polynomial function as in the figure. The relative correction width is determined by this function at any Pla Wide value.

### Time walk correction for Ge detector

For the Ge detectors, things are rather complicated due to the slow rise-time feature of the Ge signal. The rise-time of the Ge detector is as large as 200 ns and depending on the strength of the electric field. Since the electric field

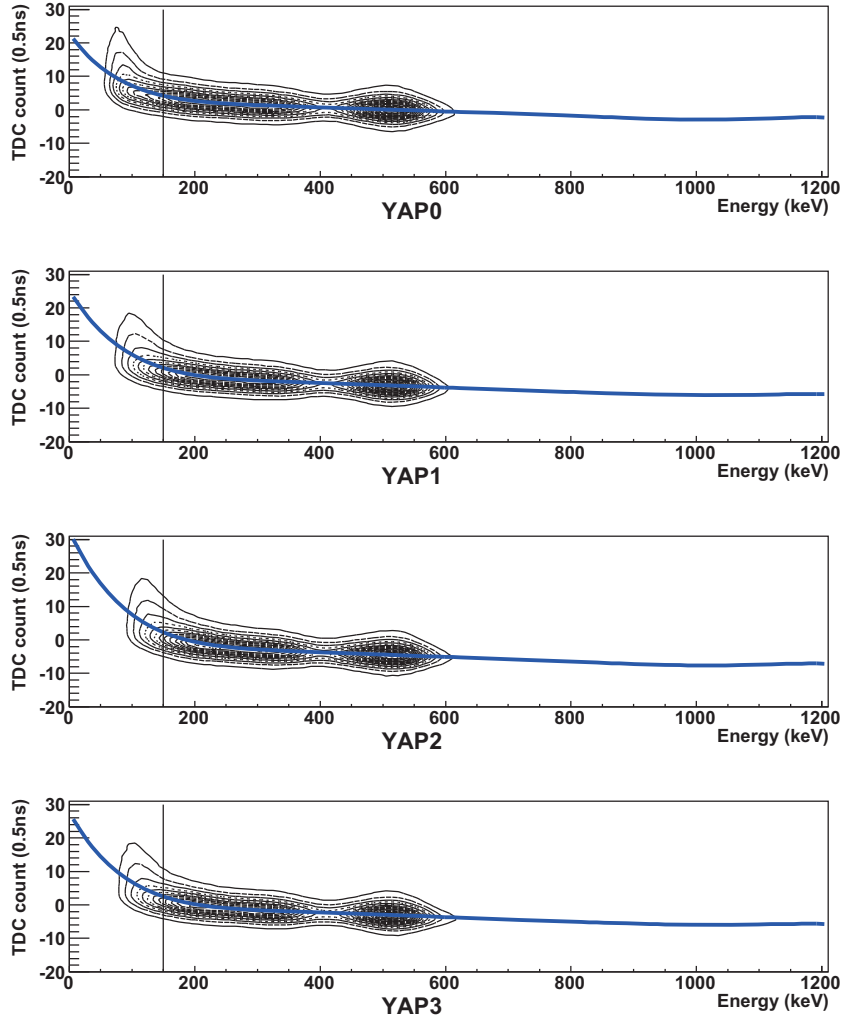


Figure 3.11: Time walk of YAP scintillator. The detection time of YAP scintillator is plotted against the YAP Wide value. The prompt peaks for every 50 keV regions of YAP Wide is fitted with seven order polynomial function. The blue line shows the fitted polynomial function and the time walk is corrected by this function.

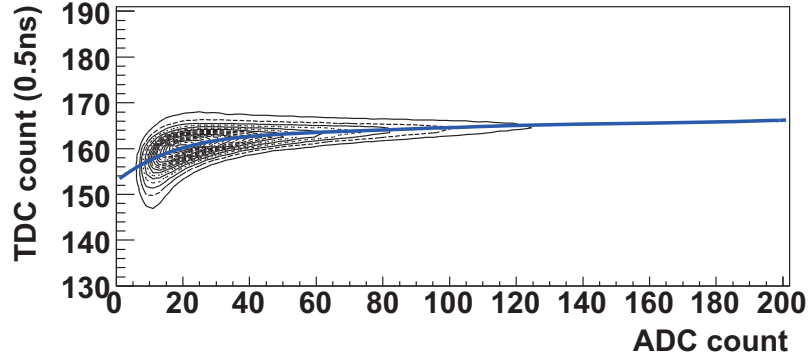


Figure 3.12: Time walk of plastic scintillator. The detection time of YAP scintillator is plotted against the Wide value of the plastic scintillator (Pla Wide). The prompt peaks for every 10 counts regions of Pla Wide is fitted with seven order polynomial function. The blue line shows the fitted polynomial function and the time walk is corrected by this function.

varies in a crystal, the rise-time of the signal depends on the position where the  $\gamma$ -ray is absorbed. In fact, the rise-time of the signal with a single energy widely ranges as shown in Fig. 3.13. The spectra in the figures are the time interval between two thresholds  $50\text{ mV}$  and  $150\text{ mV}$ , and the energy region is restricted from  $480\text{ keV}$  to  $520\text{ keV}$ . The second peak in the spectrum, which is referred to as SRT events, consist of the  $\gamma$ -rays absorbed at the front cap of the crystal, where the electric field is complicated and some places are so weak. Since the time resolution of the SRT events is too bad, the SRT events have to be eliminated. The vertical lines in the figures show the boundaries of the SRT cut.

The time walk correction makes use of the measured rise-time, or the time interval of two thresholds  $50\text{ mV}$  and  $150\text{ mV}$ . The energy region is restricted from  $480\text{ keV}$  to  $520\text{ keV}$ . The whole range of the rise-time variable is divided into 20 counts regions and the prompt peaks for these regions are fitted with normal gaussian. Then, the peak values are fitted with seven order polynomial function as in Fig. 3.14. Thus, the relative correction width is determined by the function at any rise-time variable. The obtained time resolutions for the  $511\text{ keV}$   $\gamma$ -rays are  $5.1\text{ ns}$ ,  $5.2\text{ ns}$  and  $3.2\text{ ns}$  for Ge0, Ge1 and Ge2 respectively.

### Evaluation of the SRT cut efficiency

The  $2\gamma$  and  $3\gamma$  detection efficiencies must be known to determine the decay rate by the direct pick-off correction method. But, the SRT cut efficiency is not resolved by the detector simulation. Then the SRT cut efficiency is

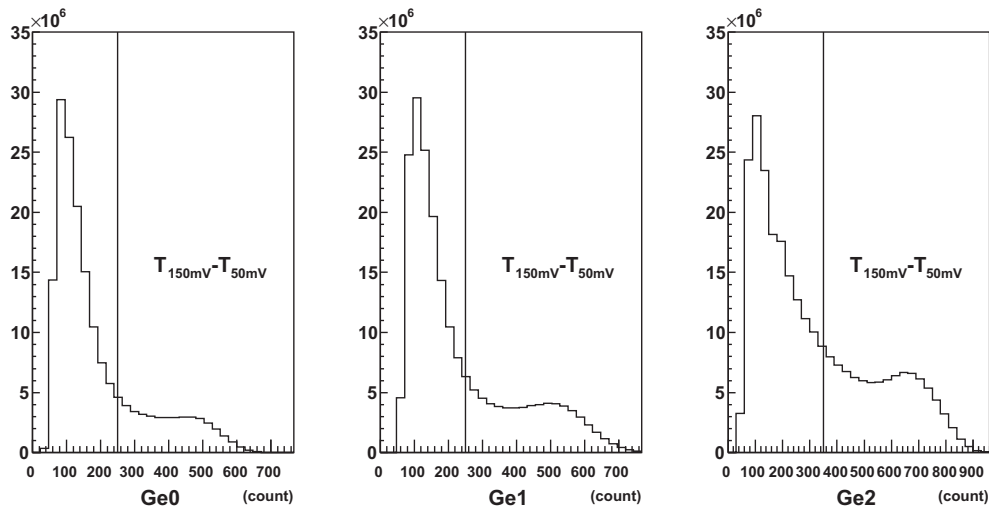


Figure 3.13: The rise-time of the Ge detectors. The time interval between two thresholds 50  $mV$  and 150  $mV$  are plotted. The unit of the horizontal axis is corresponding to 0.25  $ns$  for Ge0 (Ge1) and 0.2  $ns$  for Ge2. The energy region is restricted from 480 keV to 520 keV. The slow rise-time component, which is referred to as SRT events, is cut at the vertical line.

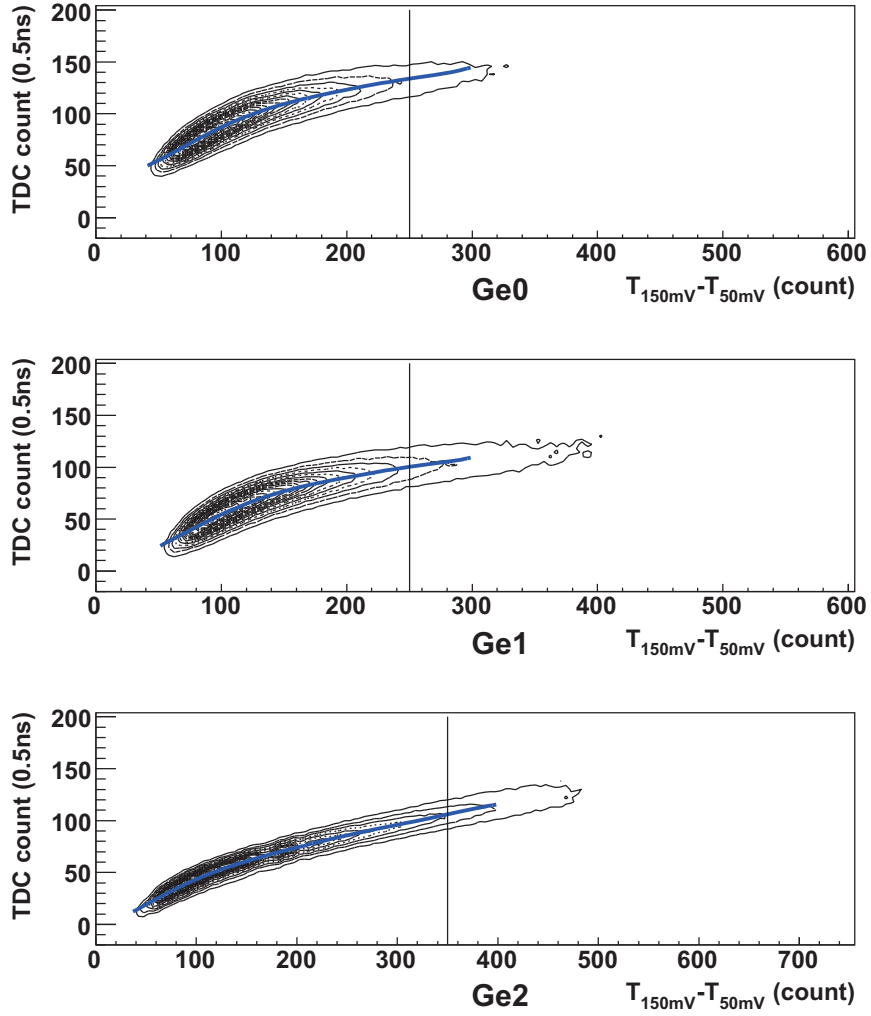


Figure 3.14: Time walk of Ge detectors. The detection time of the prompt peak is plotted against the rise-time variable ( $T_{150\text{ mV}} - T_{50\text{ mV}}$ ). The prompt peaks for every 20 counts regions of the rise-time variable is fitted with seven order polynomial function. The blue line shows the fitted polynomial function and the time walk is corrected by this function. The slow rise-time component beyond the vertical line is eliminated.

evaluated with the measured data.

The SRT cut efficiencies for Compton scattered  $2\gamma$  event and photoelectric  $3\gamma$  event are slightly different with each other even when the deposit energy is the same. This is because the distributions of the absorbed position in the crystal are different for these two cases. In practice, the Compton scattered  $2\gamma$  events rather than the photoelectric  $3\gamma$  events are more likely to be the SRT events. Therefore, the  $2\gamma$  SRT cut efficiency and the  $3\gamma$  SRT cut efficiency must be separately evaluated within the each dominant time region.

The dominant time regions for the  $3\gamma$  events and the  $2\gamma$  events are obviously the decay curve region and the prompt peak respectively. But the some part of the prompt  $2\gamma$  events enter the decay curve region because of the bad timing characteristics of the SRT events. To exclude these  $2\gamma$  events, the special time walk correction is applied for the SRT events and the much later time region is used for the evaluation of the  $3\gamma$  SRT cut efficiency.

At first, the time walk correction is applied for the SRT events. The used quantity is the time interval between two thresholds 30 mV and 50 mV, which is rather sensitive to the slow rise-time events. The Fig. 3.15 shows the correlation between the rise-time variable ( $T_{50\text{ mV}} - T_{30\text{ mV}}$ ) and the detection time of the prompt events. The fast rise-time component is not included in the figures. The linear functions shown in the figures are used to determine the time walk correction.

The obtained time resolution for the SRT events is evaluated with the data which is measured without the silica target. The Fig. 3.16 shows the time spectra before the SRT cut and after the SRT cut. The prompt peaks after the SRT cut are confined within 50 ns from the  $T_0$ , though the o-Ps in the air forms the rather long tail, which is simultaneously observed with the YAP detectors. On the other hand, the prompt peaks before the SRT cut spread over 200 ns for Ge0 (Ge1) and 600 ns for Ge2. Thus, it is found that the time region after 200 ns can be used to evaluate the  $3\gamma$  SRT cut efficiency for Ge0 and Ge1, whereas no time region is available for Ge2. The difference between Ge0 (Ge1) and Ge2 comes from the shape of the crystal. In fact, the Ge2 has the larger front cap part of the crystal than the others, where electric field is so complicated. In the circumstances, data of the Ge2 is not included in the analysis from now on.

For the  $3\gamma$  SRT cut efficiency, the time spectra of Ge0 and Ge1 is sliced out from 256 ns to 512 ns as in Fig. 3.17. The accidental contribution in this time region is subtracted by the spectrum from 2  $\mu$ s to 3.6  $\mu$ s. Then, the  $3\gamma$  SRT efficiency is obtained as the ratio of the events before and after the SRT cut. The Fig. 3.18 shows the  $3\gamma$  SRT efficiency along the deposit energy. The spectrum is fitted with the linear function from 480 keV to 500 keV and the obtained function is used for the  $3\gamma$  SRT cut efficiency. This is because the efficiency curve is slightly shifted from the linear relation in the region

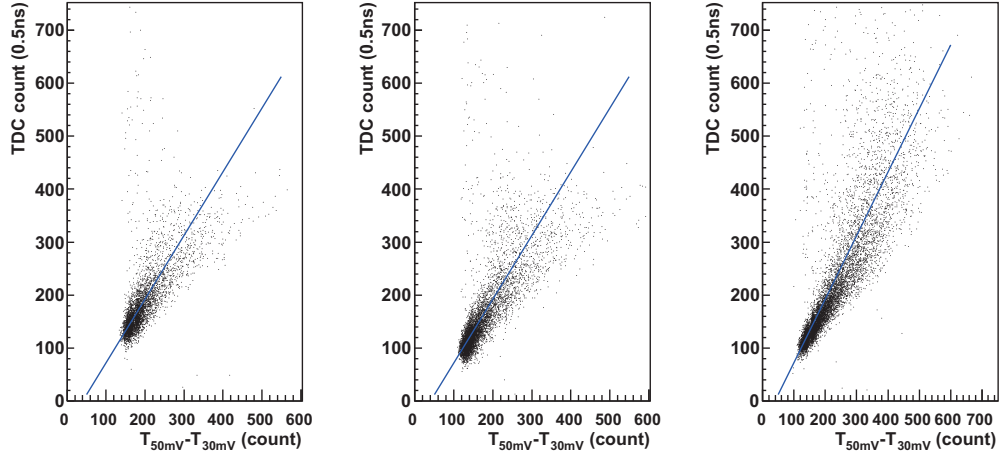


Figure 3.15: Time walk of the slow rise-time component. The detection time of the prompt events are plotted against the rise-time variable ( $T_{50\text{ mV}} - T_{30\text{ mV}}$ ). Note that the small amount of  $3\gamma$  events are not rejected. The correlations are clearly seen in the figures. The linear function shown as the blue line is used to determine the time walk correction.

under 480 keV. In addition, the pick-off contribution is negligibly small in the region under 500 keV.

On the other hand, the  $2\gamma$  SRT cut efficiency is evaluated within the time region from  $-256\text{ ns}$  to  $1536\text{ ns}$ . The obtained values are 0.76626(9) for Ge0 and 0.68378(8) for Ge1 in the region of  $511\text{ keV} \pm 4\text{ keV}$ , where the  $2\gamma$  SRT cut efficiency is used in the analysis. The contamination of  $3\gamma$  is small around 511 keV and the  $3\gamma$  SRT cut efficiency is the same as the  $2\gamma$ 's at 511 keV from the beginning. Then, the values are considered to be reliable.

The  $2\gamma$  SRT cut efficiency is also used to calculate the  $2\gamma$  efficiency in the region of 480 keV-505 keV. In this region, the contamination of  $3\gamma$  increases the obtained value by about 2 %. But the precision is not required in this case and the uncertainty of the effect does not contribute to the final result.

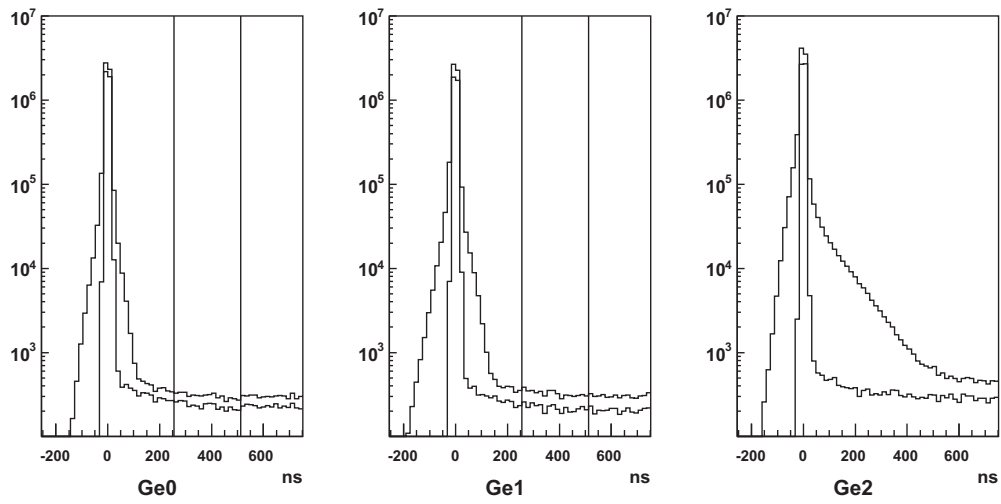


Figure 3.16: Time spectra of Ge detectors without silica target. The inside histogram is the spectrum after the SRT cut. The long tail of the spectrum after the SRT cut comes from the o-Ps in the air. The slow rise-time component of the prompt peak spreads over 200 ns for Ge0 (Ge1) and 600 ns for Ge2. The vertical lines show the region used for the evaluation of the  $3\gamma$  SRT efficiency.

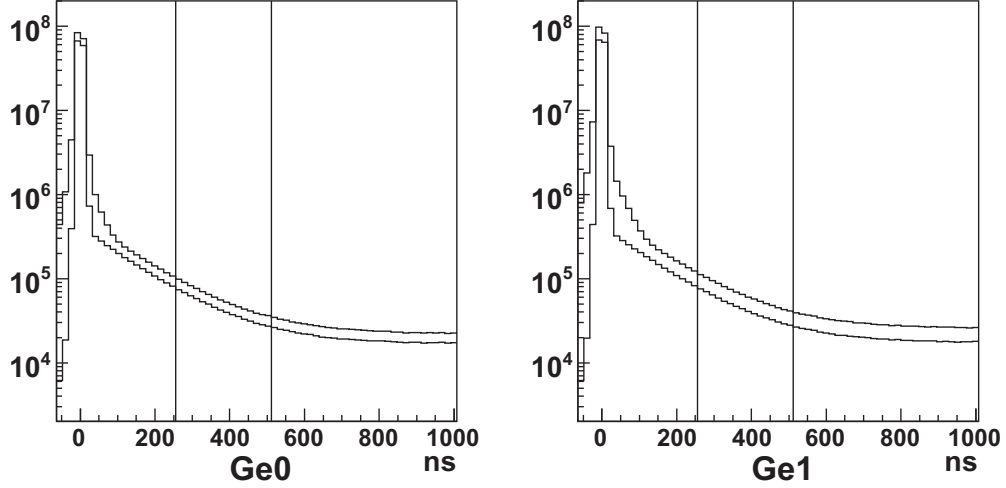


Figure 3.17: Time spectra of Ge detectors. The inside histogram is the spectrum after the SRT cut. The time region within the two vertical lines is used for the evaluation of the  $3\gamma$  SRT efficiency.

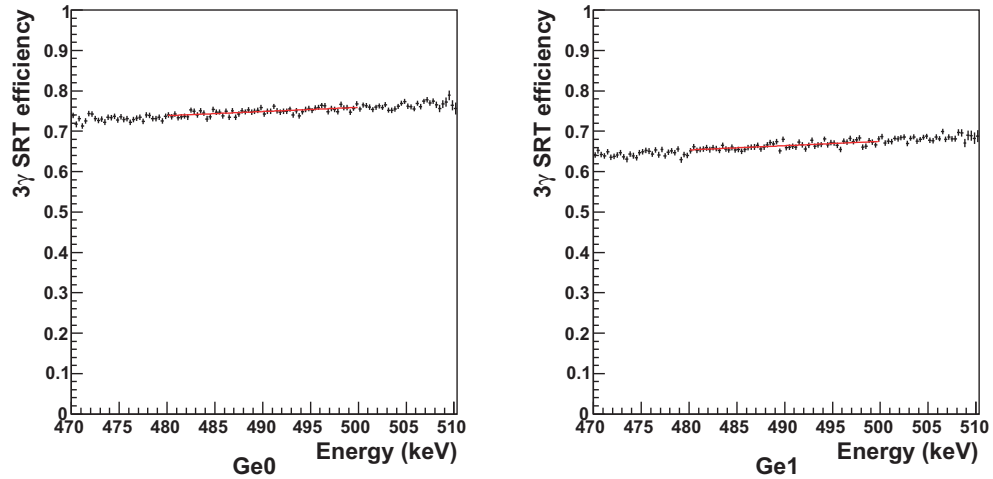


Figure 3.18:  $3\gamma$  SRT cut efficiency of Ge detectors. The event ratio before and after the SRT cut is plotted along the energy. The spectrum is fitted with linear function from 480 keV to 500 keV and the function is used as the  $3\gamma$  SRT cut efficiency. Ge0:  $1.023(150) \times 10^{-3} E(\text{keV}) + 0.247(73)$ , Ge1:  $1.063(153) \times 10^{-3} E(\text{keV}) + 0.143(75)$

## 3.2 Determination of $\lambda_{pick}(t)/\lambda_{3\gamma}$

In this section, the pick-off ratio  $\lambda_{pick}(t)/\lambda_{3\gamma}$  is determined as a function of time. Since the pick-off ratios for the two RUNs are different from each other, most of the plots are presented for each RUN.

### 3.2.1 Time and Energy Spectra of the Ge Detectors

To determine the pick-off ratio  $\lambda_{pick}(t)/\lambda_{3\gamma}$ , the energy and the timing information of the Ge detectors are made use of. After the SRT cut and the time walk correction, the time spectrum as shown in Fig. 3.19 is obtained. The three characteristic regions are observed in the figures, prompt peak, o-Ps decay curve and accidental region. These regions have different contributions of  $\gamma$ -rays and different energy spectra as follows.

#### prompt peak

A sharp peak, called as the prompt peak, is observed at  $T_0(t = 0)$ . The prompt peak consists of the p-Ps, the 1077 keV nuclei- $\gamma$  and the  $e^+$  annihilation, which is the events that positrons do not form Ps. Since most of the contributions are  $2\gamma$ , the energy spectrum is concentrated on the 511 keV photoelectric peak. The 511 keV peak of the prompt events is shown in Fig. 3.20. The energy resolution of the 511 keV peak is 1.1~1.2 keV, which is summarized in Table 3.2, whereas the intrinsic resolution of the Ge detector is 0.5~0.6 keV. This is because electrons in material have the bound momentum and the  $e^+$  annihilations are affected by the Doppler effect of this motion, and then observed as the broad photoelectric peak.

	RUN I		RUN II	
	511 keV	1077 keV	511 keV	1077 keV
Ge0	1.143 keV	0.734 keV	1.160 keV	0.744 keV
Ge1	1.153 keV	0.752 keV	1.183 keV	0.775 keV

Table 3.2: Energy resolution of the prompt events

#### o-Ps decay curve

The time region after the prompt peak, sometimes referred to as delayed region, is dominated by the o-Ps  $3\gamma$  and forms the exponential decay curve. Thus, the energy spectrum is a combination of the  $3\gamma$  continuous spectrum and the  $2\gamma$  spectrum as shown in Fig. 3.21. The latter comes from the pick-off annihilation and the accidental events.

#### accidental events

The time region far beyond the prompt peak is dominated by the

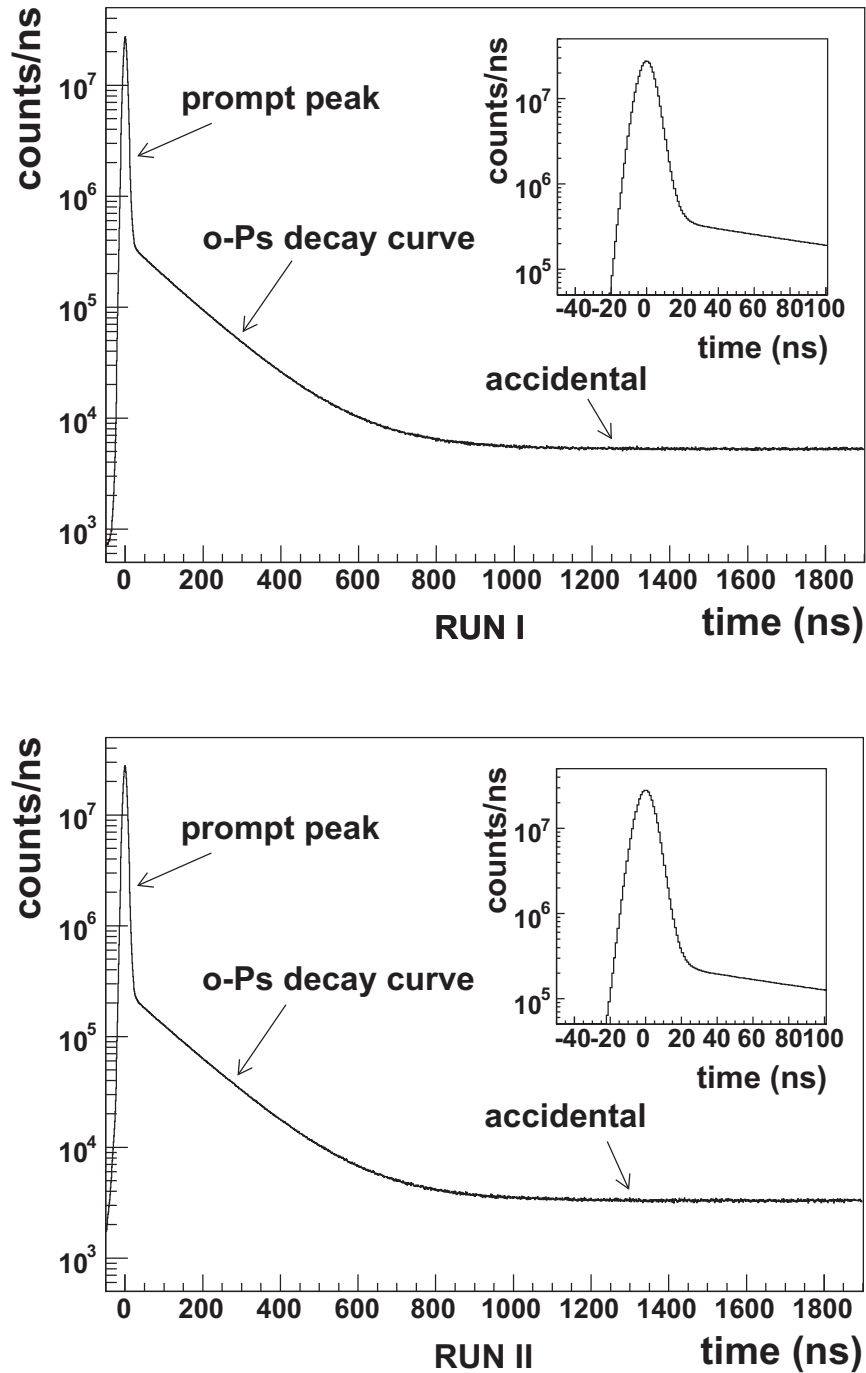


Figure 3.19: Time spectrum of Ge detectors. The upper figure is the spectrum for RUN I and the lower figure is the spectrum for RUN II. The spectrum includes both Ge0 and Ge1 events in the energy region of 300 keV-520 keV. The figure in the right corner is the enlarged view of the prompt peak.

accidental events and forms the flat time spectrum. The  $\gamma$ -ray hit of the accidental event is not correlated with the  $\beta^+$  trigger. Thus, the accidental events include all the  $\gamma$ -ray contributions, p-Ps, o-Ps,  $e^+$  annihilation and environmental background. The energy spectrum of the accidental events is nearly  $2\gamma$  spectrum as shown in Fig. 3.21. The spectrum is used to subtract the accidental contribution from the delayed region.

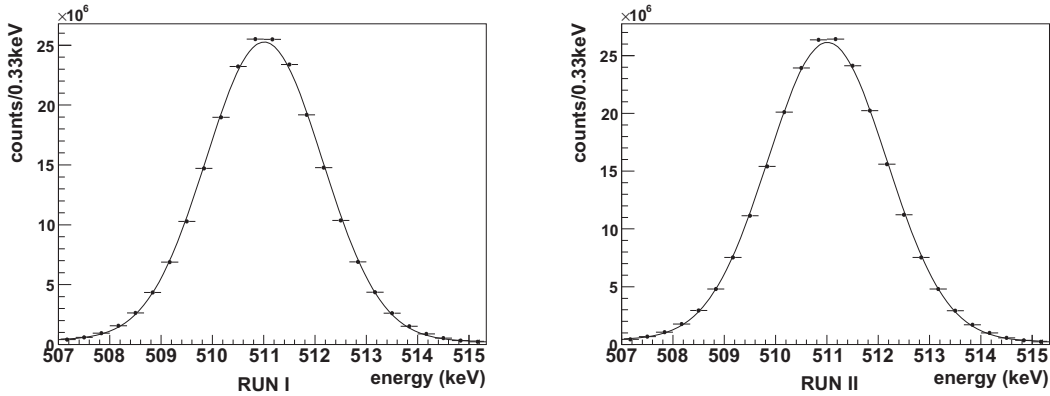


Figure 3.20: 511 keV photoelectric peak of the prompt events. The left figure is the spectrum for RUN I and the right figure is the spectrum for RUN II. The spectrum includes the prompt events of both Ge0 and Ge1, whose time region is restricted within  $\pm 10$  ns.

### 3.2.2 Extraction of the Pick-off Contribution

The delayed time region is divided into several regions to determine the pick-off ratio as a function of time. But in this section, the time region from 60 ns to 700 ns is used for the explanation of the procedures.

- First of all, the accidental contribution is subtracted from the delayed region as in Fig.3.21. The energy spectrum of the accidental time region (2000 ns - 3600 ns) is prepared for the subtraction. The normalization factor of the spectrum is described as the following equation.

$$f_{norm} = \frac{(700 - 60)}{(3600 - 2000)} \times \exp(R_{stop} \cdot \Delta t) \quad (3.1)$$

where the first term is the width of the used region and the second term is the stop rate factor. The value  $\Delta t$  is the time difference between the center of the delayed region  $(60 \text{ ns} + 700 \text{ ns})/2$  and the center of the

accidental region  $(2000 \text{ ns} + 3600 \text{ ns})/2$ . The stop rate factor comes from the fact that the data taking system accepts only the first hit of the detector, which is explained in Appendix B. The stop rates of the Ge detectors are summarized in Table 3.3.

	Ge0	Ge1
RUN I	880 Hz	1010 Hz
RUN II	550 Hz	640 Hz

Table 3.3: Typical stop rate of Ge detectors

- The next procedure is the subtraction of the  $3\gamma$  spectrum as shown in Fig.3.22. The  $3\gamma$  spectrum is produced by the Monte Carlo simulation and multiplied by the  $3\gamma$  SRT cut efficiency prepared in Sec. 3.1.5. Then, the  $3\gamma$  spectrum is normalized by the number of events ( $N_{3\gamma}$ ) within 480 keV-505 keV. However, the region contains the Compton scattered events of the pick-off  $2\gamma$ . Therefore, the normalization factor is decreased by this amount as following equation.

$$N_{3\gamma} = N(480 \text{ keV} \sim 505 \text{ keV}) - f_{\text{compton}} \times N_{\text{pick}} \quad (3.2)$$

where  $N_{\text{pick}}$  is defined as the number of events within  $\pm 4$  keV from 511 keV after the subtraction of the  $3\gamma$  spectrum. The coefficient  $f_{\text{compton}}$  is evaluated by the simulation and the values are summarized in Fig. 3.4.

detector	RUN	$f_{\text{compton}}$
Ge0	RUN I	0.0342
Ge1	RUN I	0.0337
Ge0	RUN II	0.0349
Ge1	RUN II	0.0356

Table 3.4: Compton factor  $f_{\text{compton}}$

In this step, it is found that the pick-off ratios for the two RUNs differ from each other by about a factor of three, which is seen in Fig. 3.22.

- After the subtraction of the  $3\gamma$  spectrum, the remaining spectrum is the pick-off contribution. As shown in Fig. 3.23, the spectrum is a Doppler broadening  $2\gamma$  spectrum like the prompt events. The peak value and the resolution of the 511 keV peak are summarized in Table 3.5.

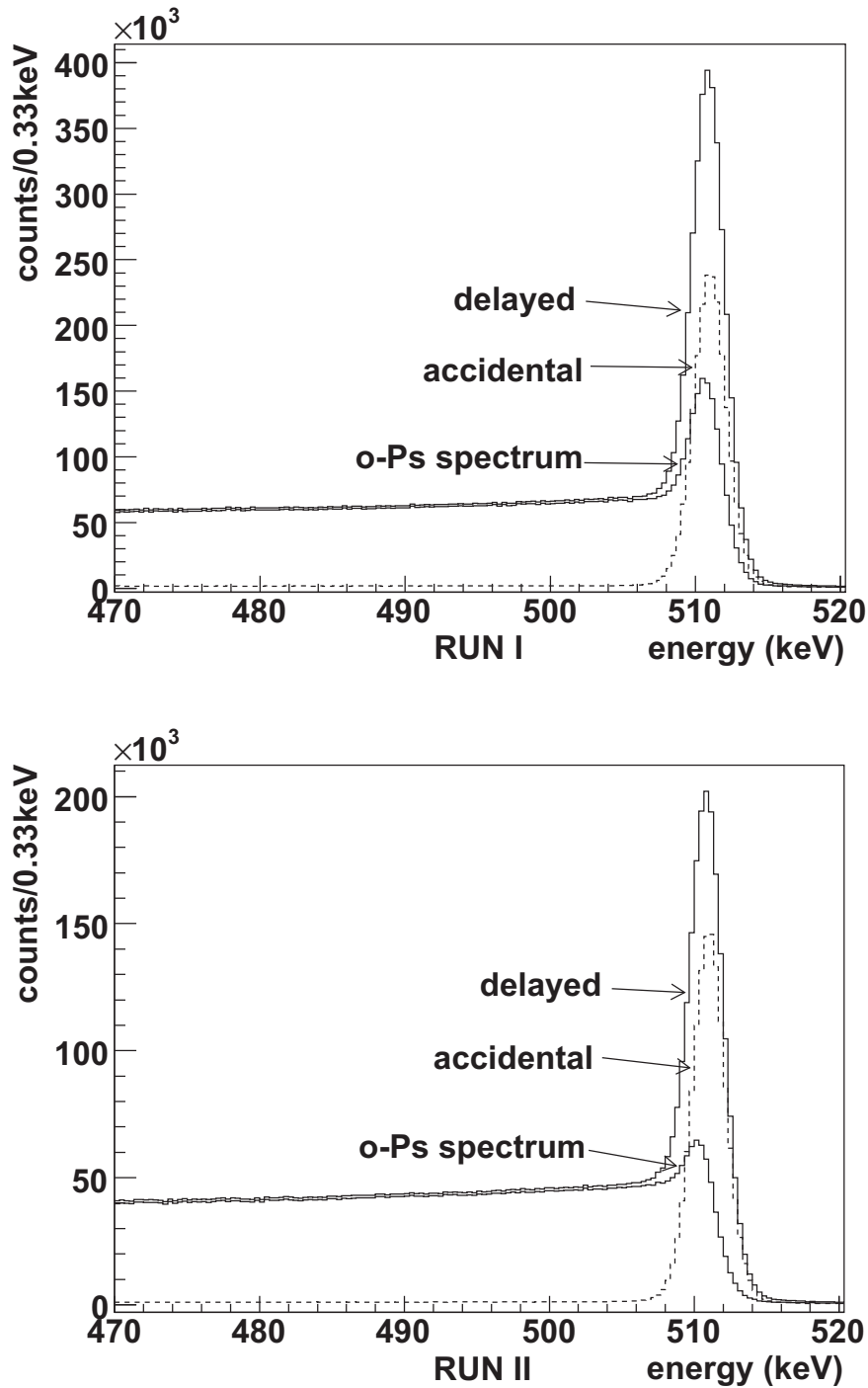


Figure 3.21: Energy spectrum of the delayed region. The upper figure is the spectrum for RUN I and the lower figure is the spectrum for RUN II. The spectrum includes both Ge0 and Ge1 events in the time region of 60 ns-700 ns. The contribution of the accidental events is subtracted by the spectrum of the accidental region from 2000 ns to 3600 ns (dotted line).

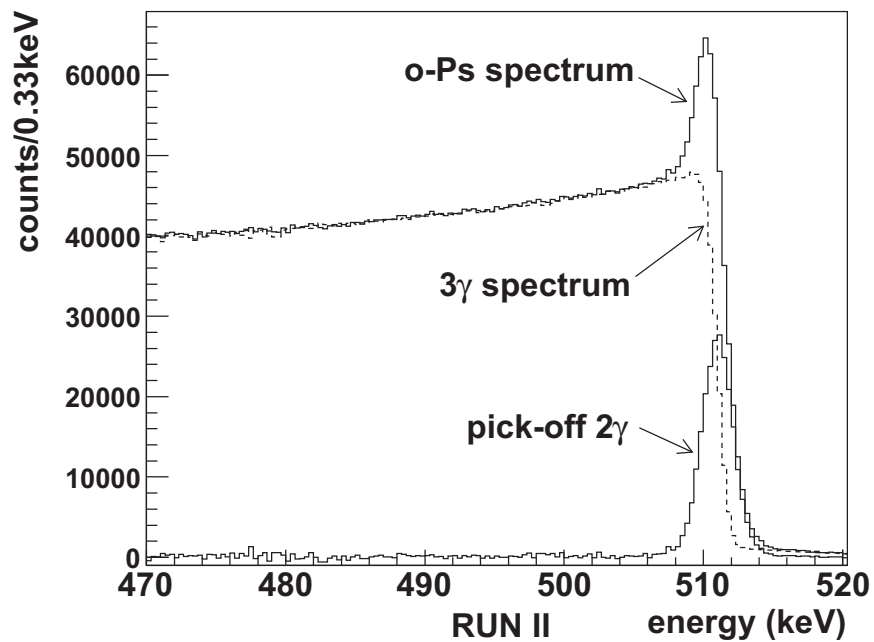
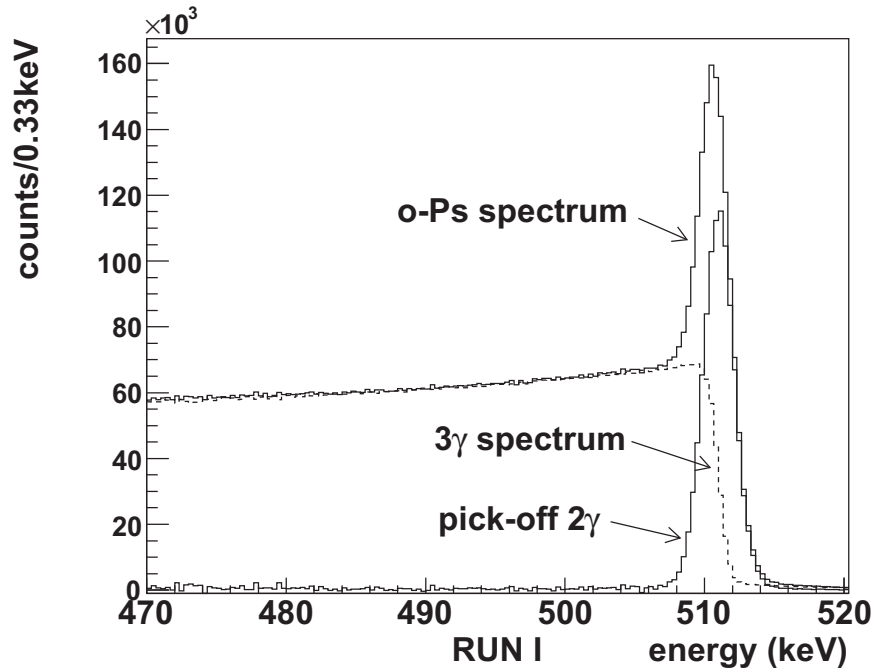


Figure 3.22: Subtraction of the  $3\gamma$  spectrum. Energy spectrum of the delayed region. The upper figure is the spectrum for RUN I and the lower figure is the spectrum for RUN II. The figure shows the spectrum after the subtraction of the accidental events. The  $3\gamma$  spectrum prepared by the simulation is normalized in the region from 480 keV to 505 keV. The difference is the contribution of the pick-off  $2\gamma$  events.

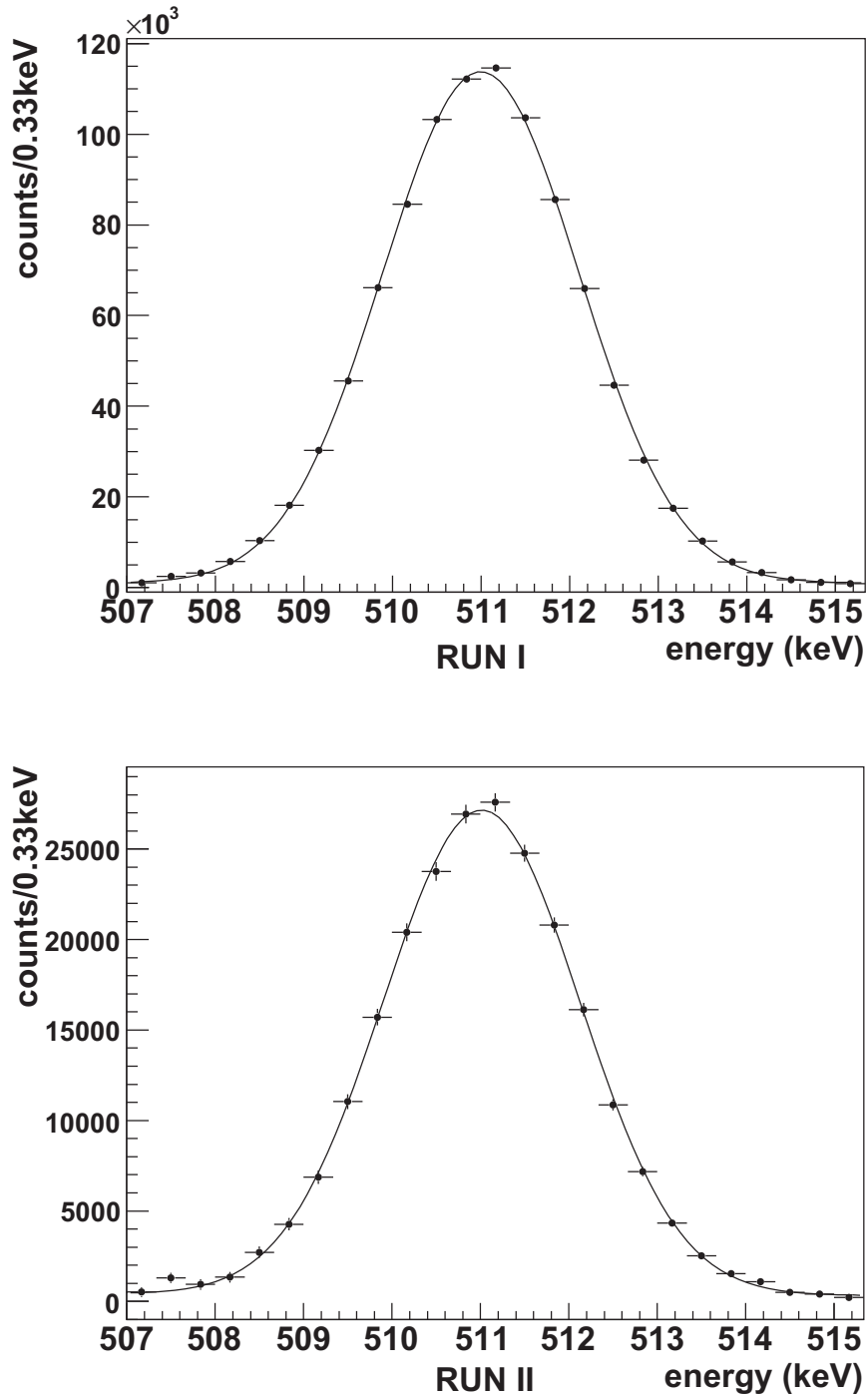


Figure 3.23: Energy spectrum of the pick-off events. The upper figure is the spectrum for RUN I and the lower figure is the spectrum for RUN II. The figure shows the spectrum after the subtraction of the  $3\gamma$  spectrum. The spectrum is a Doppler broadening  $2\gamma$  spectrum like the prompt events.

	peak value	resolution
RUN I	510.995(3) keV	1.108(3) keV
RUN II	511.013(9) keV	1.110(9) keV

Table 3.5: Peak value and resolution of the pick-off events

### 3.2.3 Determination of $\lambda_{pick}(t)/\lambda_{3\gamma}$

The pick-off ratio  $\lambda_{pick}/\lambda_{3\gamma}$  is calculated with the observed counts as the following equation.

$$\frac{\lambda_{pick}}{\lambda_{3\gamma}} = \frac{N_{pick}}{N_{3\gamma}} \times \mathcal{F} \quad (3.3)$$

where the counts  $N_{3\gamma}$  and  $N_{pick}$  are introduced in the previous section as

- $N_{3\gamma}$  = number of events within 480 keV-505 keV  
for the normalized  $3\gamma$  spectrum
- $N_{pick}$  = number of events within  $\pm 4$  keV from 511 keV  
for the pick-off spectrum.

and the conversion factor  $\mathcal{F}$  is defined as,

$$\mathcal{F} = \frac{\int_{480 \text{ keV}}^{505 \text{ keV}} P_{3\gamma}(E) dE}{\int_{507 \text{ keV}}^{515 \text{ keV}} P_{pick}(E) dE} \quad (3.4)$$

$P_{3\gamma}(E)$  and  $P_{pick}(E)$  are the detection efficiencies at energy  $E$  for  $3\gamma$  decay and  $2\gamma$  decay events respectively. That is, the observed counts  $N_{pick}, N_{3\gamma}$  are converted into the intrinsic decay rate  $\lambda_{pick}, \lambda_{3\gamma}$  with their detection efficiencies.

The factor  $\mathcal{F}$  is evaluated with the Monte Carlo simulation. The spectra for  $3\gamma$  decay and  $2\gamma$  decay events are produced and multiplied by their SRT cut efficiency. Then, the probability  $P_{3\gamma}$  and  $P_{pick}$  are integrated over the above regions. The obtained  $\mathcal{F}$  factor is summarized in Table 3.6.

detector	RUN	$\mathcal{F}$ factor
Ge0	RUN I	0.14700(15)
Ge1	RUN I	0.14632(15)
Ge0	RUN II	0.14846(14)
Ge1	RUN II	0.14760(14)

Table 3.6: Conversion factor  $\mathcal{F}$

To extract the dependency of the decay time, the delayed region is divided into 16 regions as in Table 3.7. Then, the pick-off ratio  $\lambda_{pick}/\lambda_{3\gamma}$  is calculated for each region.

time range	window width	# of windows
60-72 ns	6 ns	2
72-88 ns	8 ns	2
88-112 ns	12 ns	2
112-148 ns	18 ns	2
148-204 ns	28 ns	2
204-288 ns	42 ns	2
288-416 ns	64 ns	2
416-608 ns	96 ns	2

Table 3.7: Definition of the time windows

The obtained ratio is shown in Fig. 3.24. The curve in the figure represents the thermalization process of o-Ps. It takes about 600 ns that o-Ps is fully thermalized in silica aerogel and silica powder. The pick-off ratio of the RUN I (silica aerogel) is about 3 times higher than the one of RUN II (silica powder). The difference is considered to originate in the characteristics of the silica material such as the grain size, the aggregate structure, the surface.

The pick-off ratio is fitted with the analytic function for later uses. The analytic form of the thermalization process is discussed in Sec. 2.1.3. But, the next rather simple form is adopted for technical reasons.

$$\frac{d}{dt}\theta(t) = -C \left( \theta(t)^2 - \theta_{\infty}^2 \right) \theta(t)^{2\beta} \quad (3.5)$$

where  $\theta(t) \equiv \lambda_{pick}(t)/\lambda_{3\gamma}$  and numerous parameters are substituted with one new fitting parameter  $\beta$ . This notation is identical to the one which can be found in reference [41]. The equation is numerically solved by the Runge-Kutta method, which is implemented as the subroutine DDEQMR in CERN LIB [56]. Since the first-order differential equation requires a boundary condition, one more variable, the pick-off ratio at 60 ns ( $\theta_{60}$ ), is introduced. The result of the fitting is summarized in Table 3.8.

The uncertainties of the fitted parameters are estimated by the MINOS error analysis routine in the *MINUIT* package [57]. However, the parameter  $C$  and  $2\beta$  are tightly correlated with each other and the correlation coefficient is almost 1. This is caused by the small magnitude of the pick-off rate  $\theta(t)$ , which is the order of  $10^{-2}$ . Therefore, the rather diagonal form is used for the error estimation.

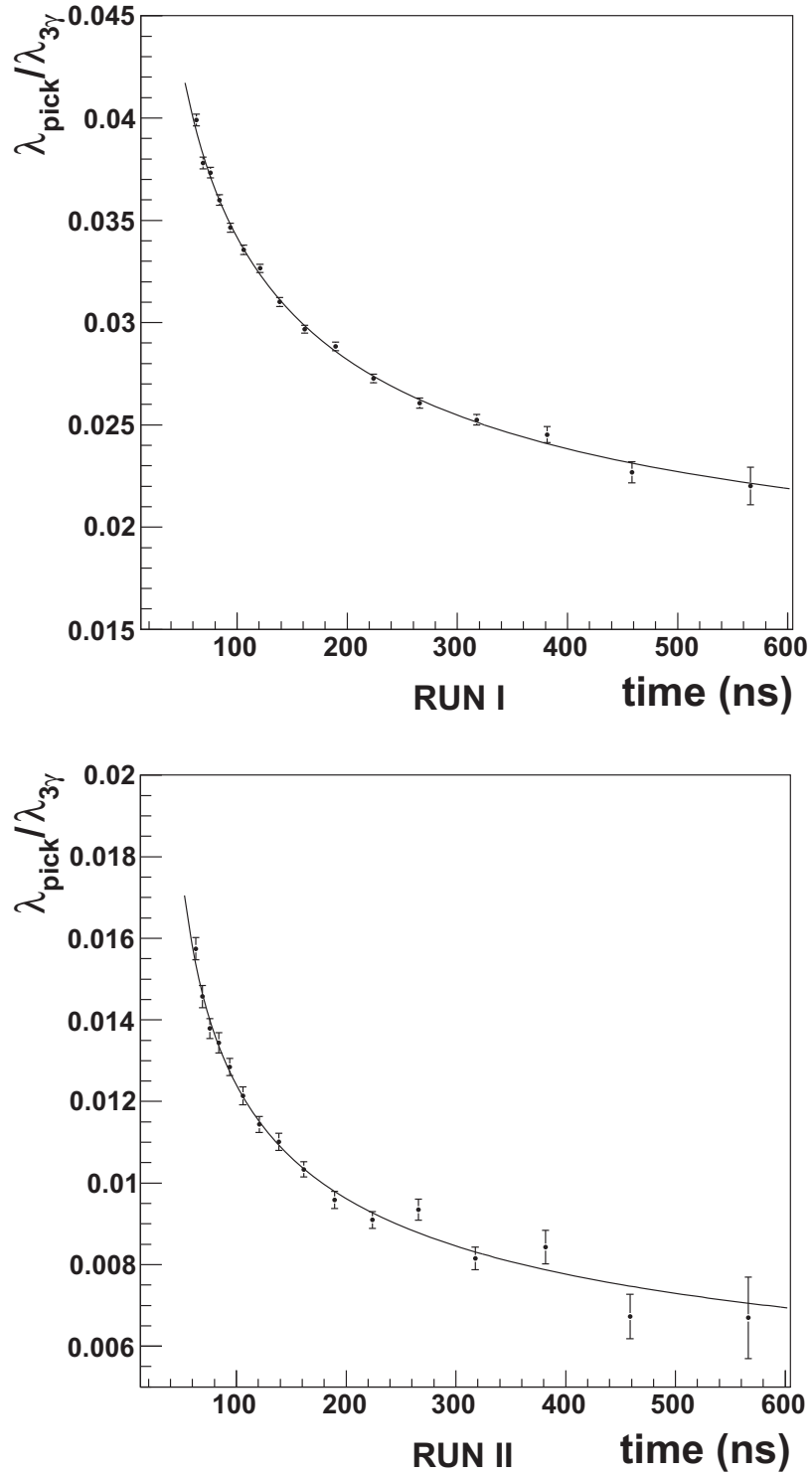


Figure 3.24: Pick-off ratio  $\lambda_{pick}(t)/\lambda_{3\gamma}$ . The upper figure is the spectrum for RUN I and the lower figure is the spectrum for RUN II. The slow curve represents the thermalization process of o-Ps. The pick-off ratio of the RUN I is about 3 times higher than the one of RUN II.

parameters	RUN I	RUN II
$C$	$2.71 \times 10^3$	$5.87 \times 10^4$
$\theta_\infty$	$1.24 \times 10^{-2}$	0
$2\beta$	3.02	2.75
$\theta_{60}$	$4.04 \times 10^{-2}$	$1.61 \times 10^{-2}$
reduced $\chi^2$	1.00	1.11

Table 3.8: Summary of  $\lambda_{pick}(t)/\lambda_{3\gamma}$  fitting result

$$\frac{d}{dt}\theta'(t) = -C' \left( \theta'(t)^2 - \theta_\infty^2 \right) \theta'(t)^{2\beta} \quad (3.6)$$

where  $\theta'(t) = f \theta(t)$ ,  $C' = f^{-1-2\beta} C$ ,  $\theta_\infty = f \theta_\infty$ ,  $f = 40$  for RUN I and  $f = 100$  for RUN II. The estimated uncertainties of the parameters are summarized in Table 3.9. The uncertainty of the parameter  $\theta_\infty$  in the negative direction is not defined since the deviation of  $\chi^2$  does not reach +1 even if  $\theta_\infty$  is set to be 0.

parameters	RUN I		RUN II	
	negative	positive	negative	positive
$C'$	$-2.68 \times 10^{-4}$	$+7.86 \times 10^{-4}$	$-1.26 \times 10^{-4}$	$+1.43 \times 10^{-3}$
$\theta_\infty$	not defined	$+7.22 \times 10^{-3}$	not defined	$+6.50 \times 10^{-3}$
$2\beta$	-1.07	+0.60	-1.13	+0.37
$\theta_{60}$	$-2.96 \times 10^{-4}$	$+2.96 \times 10^{-4}$	$-3.03 \times 10^{-4}$	$+3.17 \times 10^{-4}$

Table 3.9: Uncertainties of the fitted parameter (RUN I).

The propagation of the uncertainties is evaluated as the following procedures. At first, one of four parameters is fixed at the value which is deviated from the best fit value by  $1 \sigma$ . The rest parameters are fitted as the free parameters again. The obtained parameters and pick-off function are prepared to evaluate the uncertainty of the parameter. Thus, the deviated functions for the four parameters are obtained as shown in Fig. 3.25 and Fig. 3.26. Then, the total propagation of the uncertainties to the decay rate is defined as follows.

$$\sigma_{total} = \sqrt{\frac{\sum_{i=1}^4 \sigma_i^2(\text{pos}) + \sigma_i^2(\text{neg})}{2}} \quad (3.7)$$

where  $\sigma_i(\text{pos})$ ,  $\sigma_i(\text{neg})$  are the deviation of the decay rate when the parameter  $i$  is deviated in the positive direction and the negative direction and then the corresponding function is used for the decay rate fitting.

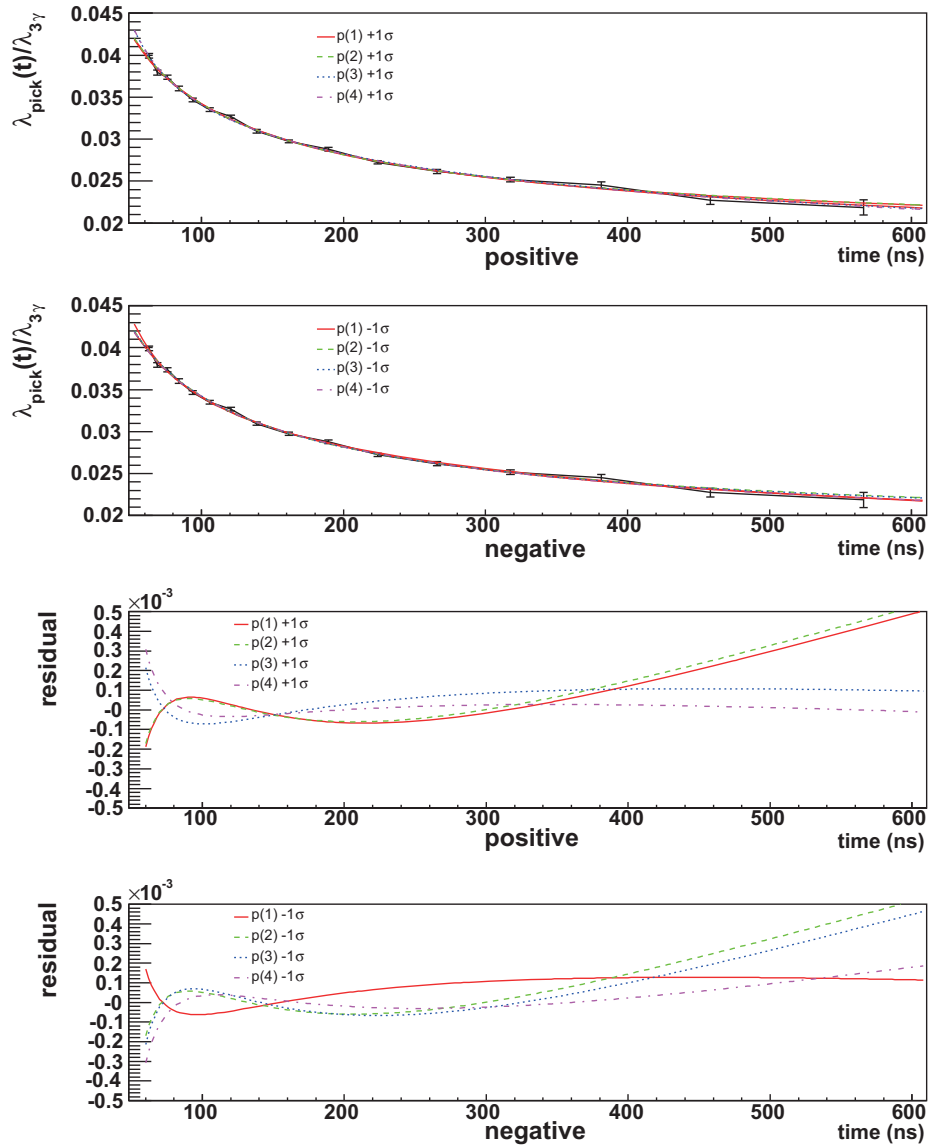


Figure 3.25: Uncertainties of the parameters (RUN I). The upper two figures are the deviated function when one parameter is fixed at  $+1\sigma$  and at  $-1\sigma$ . The lower two figures show the deviation of the pick-off ratio for each function.

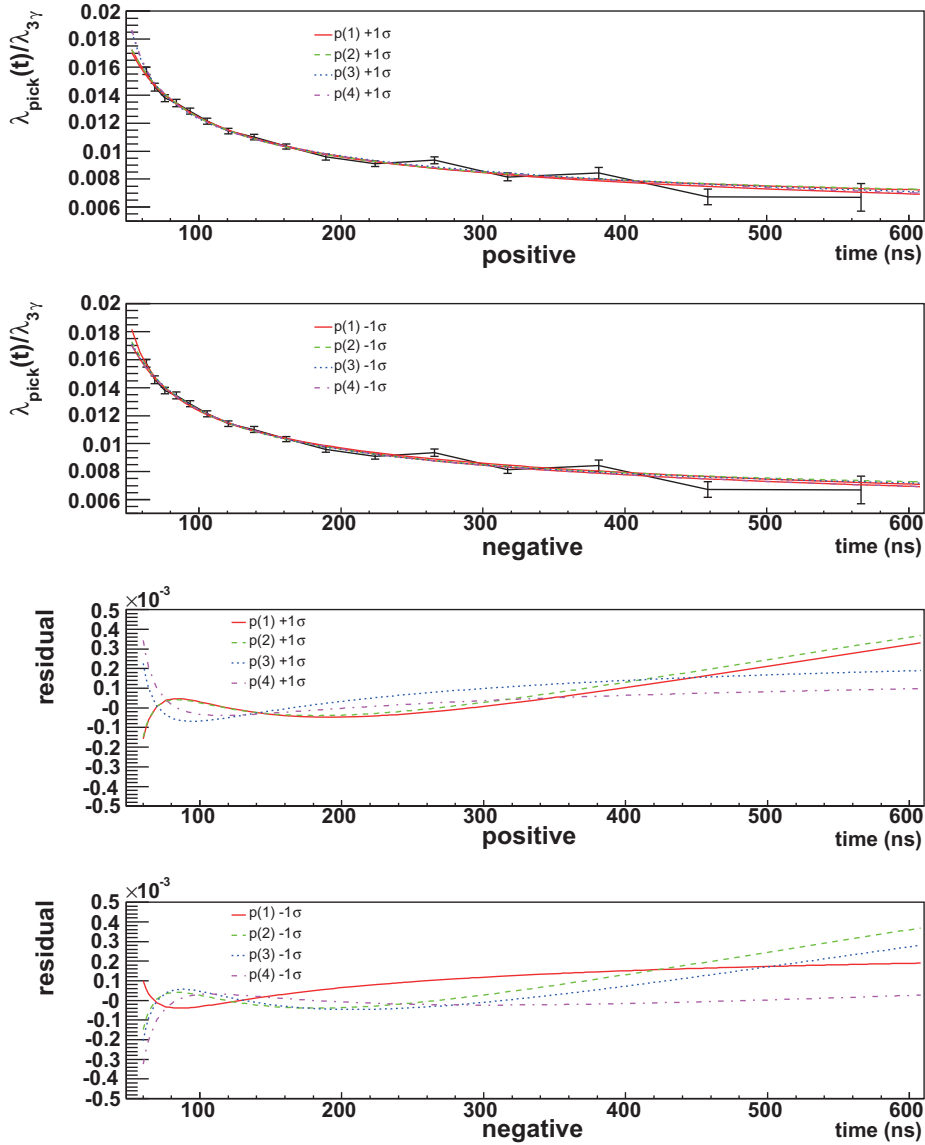


Figure 3.26: Uncertainties of the parameters (RUN II). The upper two figures are the deviated function when one parameter is fixed at  $+1\sigma$  and at  $-1\sigma$ . The lower two figures show the deviation of the pick-off ratio for each function.

### 3.3 Decay Rate Fitting

In this section, the time spectrum of the YAP scintillators is fitted to obtain the intrinsic decay rate. The fitting function includes the pick-off ratio measured in the previous section.

#### 3.3.1 Time and Energy Spectrum of the YAP Scintillators

After the time walk correction, the time spectrum of the YAP scintillators is obtained as in Fig. 3.28. As in Fig. 3.27, the energy region is restricted above 150 keV since the time walk and the resolution are large in the energy region below 150 keV. The three characteristic regions, prompt peak, o-Ps decay curve and accidental region, are observed as in the case of Ge detector. But, the prompt peak of the YAP scintillators is more sharp than the one of the Ge detectors. In addition, the number of events is much larger than the one of Ge. This is attributed to the good timing characteristics of YAP scintillator.

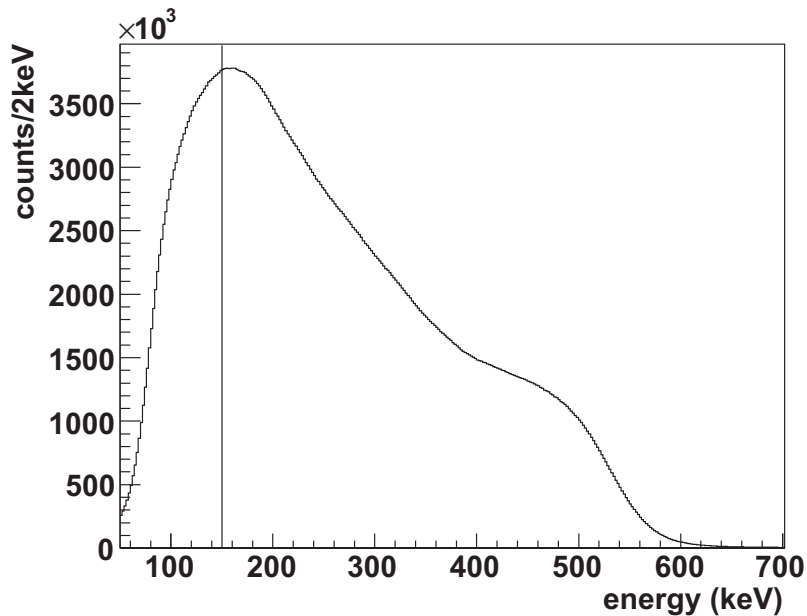


Figure 3.27: Energy spectrum of YAP scintillator in the delayed region. The time region is restricted from 60 ns to 700 ns. The vertical line shows the energy threshold of 150 keV.

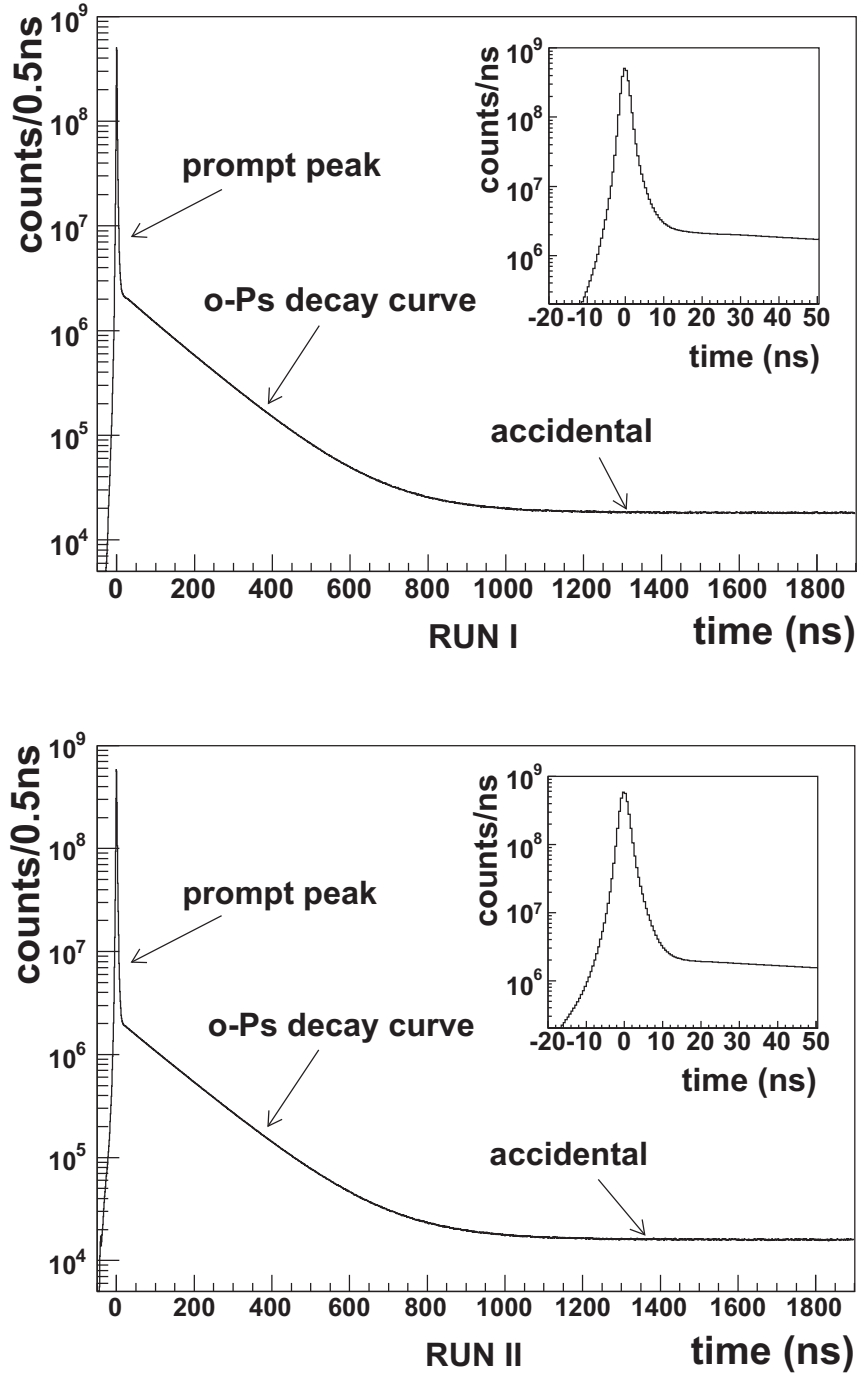


Figure 3.28: Time spectrum of the YAP scintillators. The upper figure is the spectrum for RUN I and the lower figure is the spectrum for RUN II. The spectrum include the events of all the YAP scintillators in the energy region above 150 keV. The figure in the right coner is the enlarged view of the prompt peak.

	YAP0	YAP1	YAP2	YAP3
RUN I	0.718	0.717	0.701	—
RUN II	0.730	0.714	0.700	0.723

Table 3.10: Ratio  $\epsilon_{pick}/\epsilon_{3\gamma}$  of YAP scintillators

	YAP0	YAP1	YAP2	YAP3
RUN I	1530 Hz	1440 Hz	1540 Hz	—
RUN II	750 Hz	590 Hz	850 Hz	680 Hz

Table 3.11: Typical stop rate of YAP scintillators

### 3.3.2 Decay Rate Fitting

The analytic form of the observed time spectrum is discussed in Sec. 2.1.3 and given by,

$$N_{obs}(t) = e^{-R_{stop}t} \left[ \left( 1 + \frac{\epsilon_{pick}}{\epsilon_{3\gamma}} \frac{\lambda_{pick}(t)}{\lambda_{3\gamma}} \right) N_0 \exp \left( -\lambda_{3\gamma} \int_0^t \left( 1 + \frac{\lambda_{pick}(t')}{\lambda_{3\gamma}} \right) dt' \right) + C \right]. \quad (3.8)$$

The ratio  $\epsilon_{pick}/\epsilon_{3\gamma}$  is estimated by the Monte Carlo simulation. The values are summarized in Table 3.10. The stop rate  $R_{stop}$  of YAP scintillators are summarized in Table 3.11. Thus, the free parameters in Eq. (3.8) are just three,  $N_0$ ,  $C$  and  $\lambda_{3\gamma}$ .

The part of Eq. (3.8) containing time integration can be rewritten as,

$$\begin{aligned} & N_0 \exp \left( -\lambda_{3\gamma} \int_0^t \left( 1 + \frac{\lambda_{pick}(t')}{\lambda_{3\gamma}} \right) dt' \right) \\ &= N_0 \exp \left( -\lambda_{3\gamma} \int_0^{t_{start}} \left( 1 + \frac{\lambda_{pick}(t')}{\lambda_{3\gamma}} \right) dt' - \lambda_{3\gamma} \int_{t_{start}}^t \left( 1 + \frac{\lambda_{pick}(t')}{\lambda_{3\gamma}} \right) dt' \right) \\ &= \overline{N_0} \exp \left( -\lambda_{3\gamma} \int_{t_{start}}^t \left( 1 + \frac{\lambda_{pick}(t')}{\lambda_{3\gamma}} \right) dt' \right) \end{aligned} \quad (3.9)$$

Therefore, the integration before  $t_{start}$  is absorbed into the normalization factor  $\overline{N_0}$  and does not have any influence on the decay rate fitting.

The different size of  $\epsilon_{pick}/\epsilon_{3\gamma}$  factor is another problem when the time spectra of the YAP scintillators are combined. To overcome this difficulty, the following procedures are performed.

1. At first, the constant term  $C$  is fixed by fitting the accidental time region from 2000 ns to 3600 ns. Then, the accidental contribution is subtracted from the time spectrum.

2. The detector dependent term,

$$\left(1 + \frac{\varepsilon_{pick}}{\varepsilon_{3\gamma}} \frac{\lambda_{pick}(t)}{\lambda_{3\gamma}}\right) \quad (3.10)$$

is divided from the time spectrum. Then the following spectrum is obtained for each detector.

$$N(t) = \overline{N}_0 \exp\left(-\lambda_{3\gamma} \int_{t_{start}}^t \left(1 + \frac{\lambda_{pick}(t')}{\lambda_{3\gamma}}\right) dt'\right) \quad (3.11)$$

3. The subtracted term  $C$  is added to each time spectrum. At this stage, the time spectrum is independent of the detector efficiency as,

$$N'(t) = \overline{N}_0 \exp\left(-\lambda_{3\gamma} \int_{t_{start}}^t \left(1 + \frac{\lambda_{pick}(t')}{\lambda_{3\gamma}}\right) dt'\right) + C \quad (3.12)$$

4. The obtained time spectra are simply summed up into one spectrum.

#### Time spectrum fitting for RUN I

The time spectrum is fitted by the minimization package *MINUIT* [57]. The fitted decay rate and reduced  $\chi^2$  is shown in Fig. 3.29. The fitted decay rate is plotted against the fitting start time to see the dependence on the fitting start time. The fitting end time is fixed at 3600 *ns*. It is found that the fitted decay rate is flat along the decay time and no significant dependence is observed. The reduced  $\chi^2$  is also flat along the fitting start time and the value is reasonable.

Therefore, the fitting start time is fixed at 60 *ns* and the obtained decay rate for RUN I is determined to be,

$$\lambda_{3\gamma} = 7.03876 \pm 0.0009(stat.) \mu s^{-1}, \quad (3.13)$$

where only the statistic error is shown. The propagated error from  $\lambda_{pick}(t)/\lambda_{3\gamma}$  fitting is already included.

#### Time spectrum fitting for RUN II

The time spectrum for RUN II is fitted by the same procedures as for RUN I. The result is shown in Fig. 3.30. No significant dependence on the decay time is found in both the fitted decay rate and reduced  $\chi^2$ .

Then, the fitting start time is fixed at 60 *ns* and the obtained decay rate for RUN II is determined to be,

$$\lambda_{3\gamma} = 7.04136 \pm 0.0009(stat.) \mu s^{-1}, \quad (3.14)$$

where only the statistic error is shown as for RUN I.

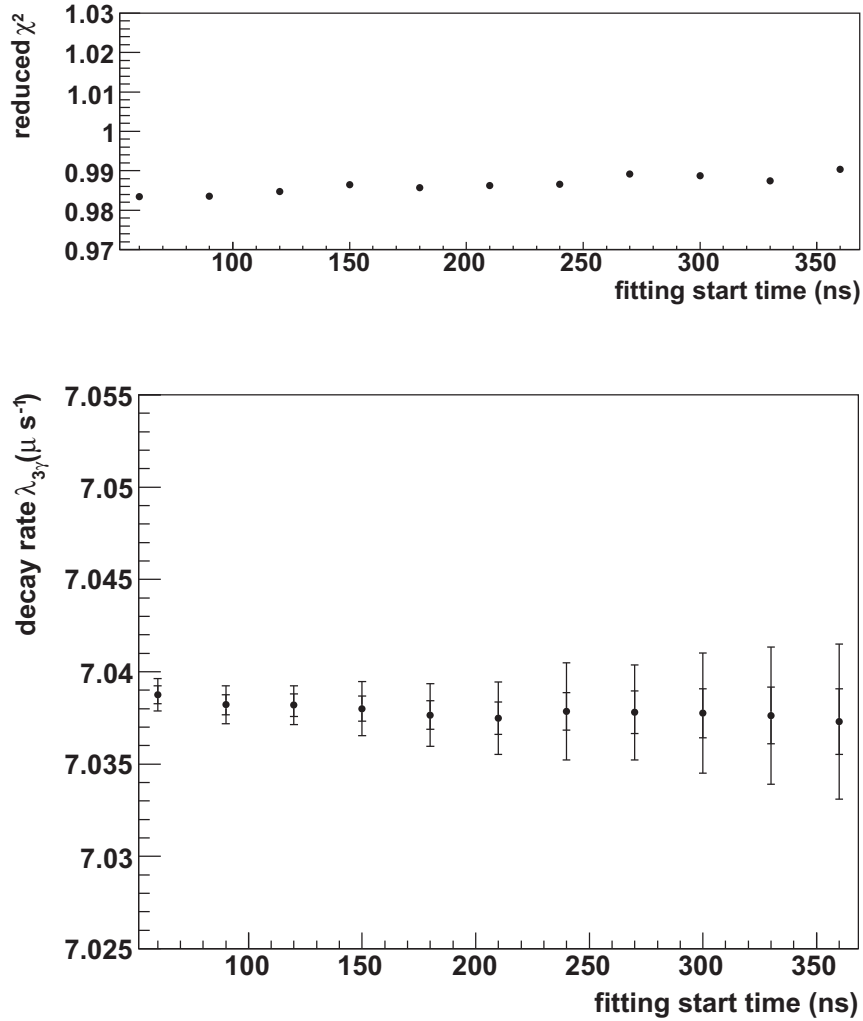


Figure 3.29: Fitted decay rate (RUNI). The fitted decay rate is plotted along the fitting start time in the lower figure. The error bars show only the statistic error and the inner lines represent the statistic error of the YAP time spectrum. The reduced  $\chi^2$  along the fitting start time is also shown in the upper figure. Since the bin width of the histogram is  $0.5\text{ ns}$ , the degree of freedom is  $7080-3$  at  $60\text{ ns}$  fitting start time.

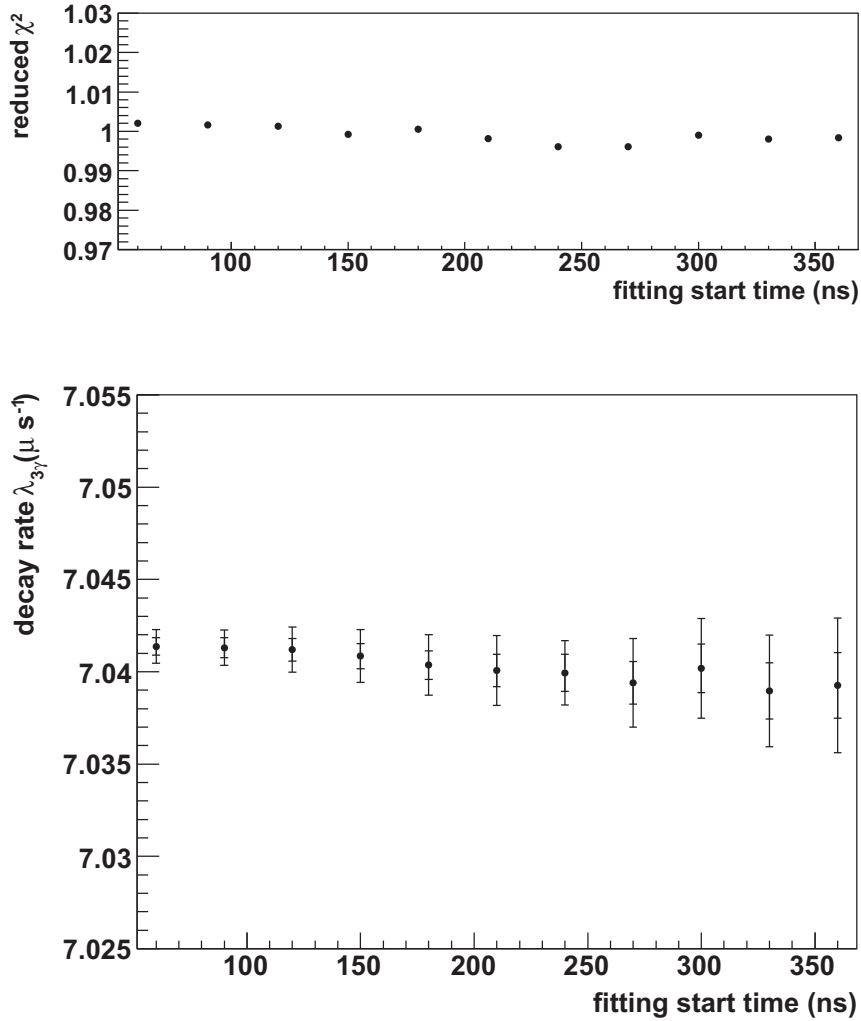


Figure 3.30: Fitted decay rate (RUNII). The fitted decay rate is plotted along the fitting start time in the lower figure. The error bars show only the statistic error and the inner lines represent the statistic error of the YAP time spectrum. The reduced  $\chi^2$  along the fitting start time is also shown in the upper figure. Since the bin width of the histogram is  $0.5\text{ ns}$ , the degree of freedom is  $7080-3$  at  $60\text{ ns}$  fitting start time.

### 3.4 Various Checks

The several cuts are applied to the obtained data in order to reject the pile-up events and the slow rise-time events. The measured decay rate must be independent of the cut condition since the choice of the boundary is rather arbitrary. To make sure of this independency, the cut conditions are varied to some extent.

In addition, to check the quality of the data sample, data of each run are divided into four samples.

#### 3.4.1 Energy Selection

The energy windows for YAP scintillator and Ge detector are varied and the deviations of the decay rate are shown in the following tables. The efficiency is also reevaluated according to the energy window. The observed deviation of the decay rate is less than one third of the statistic error for both YAP scintillator and Ge detector. Considering the fact that about 20 % of the events are varied for both YAP scintillator and Ge detector, the deviation of the decay rate is considered to be statistical fluctuation. Therefore, one can conclude that the obtained decay rate is not biased by the energy window.

The energy window for the pick-off 511 keV peak is not varied since the wider window sums up the uncertainty of the  $3\gamma$  subtraction. The uncertainty of the  $3\gamma$  is guaranteed for the window of 511 keV  $\pm 4$  keV in Sec.3.5.3.

**for YAP scintillator** normal threshold: 150 keV

	strict cut	loose cut
RUN I	200 keV $\sim$ +14 ppm	100 keV $\sim$ -30 ppm
RUN II	200 keV $\sim$ -20 ppm	100 keV $\sim$ -9 ppm

**for Ge detector** normal range: 480 keV  $\sim$  505 keV

	lower boundary	higher boundary
RUN I	485 keV $\sim$ 505 keV -13 ppm	480 keV $\sim$ 500 keV -33 ppm
RUN II	485 keV $\sim$ 505 keV +37 ppm	480 keV $\sim$ 500 keV -0 ppm

#### 3.4.2 Base Cut

The Base cut conditions for YAP scintillator and Ge detector are varied and the deviations of the decay rate are shown in the following tables. The deviation of the decay rate is considered to be the statistical fluctuation.

The effect of the contamination below  $140 \sigma$  boundary is discussed in the next section.

**for YAP scintillator** normal range:  $-4 \sigma \sim +140 \sigma$

	strict cut	loose cut
RUN I	$-3 \sigma \sim +130 \sigma$ +0 ppm	$-6 \sigma \sim +160 \sigma$ +0 ppm
RUN II	$-3 \sigma \sim +130 \sigma$ -1 ppm	$-6 \sigma \sim +160 \sigma$ +7 ppm

**for Ge detector** normal range:  $\pm 4 \sigma$

	strict cut	loose cut
RUN I	$-3 \sigma \sim +3 \sigma$ +9 ppm	$-6 \sigma \sim +6 \sigma$ +7 ppm
RUN II	$-3 \sigma \sim +3 \sigma$ +4 ppm	$-6 \sigma \sim +6 \sigma$ +4 ppm

### 3.4.3 Narrow-Wide Cut

The Narrow-Wide cut conditions for YAP scintillator and Ge detector are varied and the deviations of the decay rate are shown in the following tables. The deviation of the decay rate is considered to be the statistical fluctuation. The effect of the contamination is small as discussed in Appendix B.3.1. But the deviation of Ge energy spectrum is incorporated into the response function (see Sec. 2.4).

**for YAP scintillator** normal range:  $\pm 30 \text{ keV}$

	strict cut	loose cut
RUN I	$-25 \text{ keV} \sim +25 \text{ keV}$ +13 ppm	$-40 \text{ keV} \sim +40 \text{ keV}$ +7 ppm
RUN II	$-25 \text{ keV} \sim +25 \text{ keV}$ +0 ppm	$-40 \text{ keV} \sim +40 \text{ keV}$ +3 ppm

**for Ge detector** normal range:  $\pm 15 \text{ keV}$

	strict cut	loose cut
RUN I	$-12 \text{ keV} \sim +12 \text{ keV}$ -4 ppm	$-20 \text{ keV} \sim +20 \text{ keV}$ +4 ppm
RUN II	$-12 \text{ keV} \sim +12 \text{ keV}$ -0 ppm	$-20 \text{ keV} \sim +20 \text{ keV}$ +4 ppm

### 3.4.4 SRT Cut

The SRT cut conditions for Ge detector are varied and the deviations of the decay rate are shown in the following table. The efficiency is also reevaluated according to the cut condition. The deviation of the decay rate is considered to be the statistical fluctuation and the deviation of the response function. The response function of the Monte Carlo, which is evaluated with the normal cut condition, is not changed at this time. In practice, the SRT cut correlates with the response function and the decay rate slightly increases at loose cut for the underestimation of  $\mathcal{F}$  factor.

**for Ge detector** normal boundary: 62.5 ns (250 counts)

	strict cut	loose cut
RUN I	$\sim 57.5$ ns (230 counts) -7 ppm	$\sim 67.5$ ns (270 counts) +27 ppm
RUN II	$\sim 57.5$ ns (230 counts) -6 ppm	$\sim 67.5$ ns (270 counts) +9 ppm

### 3.4.5 Data Sample

To check the quality of the data sample, data of each run are divided into four samples. The decay rates of the four samples are shown in Fig. 3.31 for RUN I and Fig. 3.32 for RUN II. The decay rates of the four samples are statistically fluctuated in the figure. Since the same Monte Carlo data is used for the four samples, the systematic error of the detector efficiency and the shape of the  $3\gamma$  spectrum is completely correlated among the four samples.

## 3.5 Systematic Errors

In this section, the systematic errors accompanying the measurement is discussed. They are put into several categories according to their origins.

### 3.5.1 TDC Module Related Errors

The KEK TDC used in the measurement is jointly developed by KEK and our group. The KEK TDC is a direct clock counting type TDC and all the systematic errors can be attributed to the external clock source. The characteristics of the KEK TDC and the external clock source is explained in Sec.2.3.4.

#### **Integral non-linearity (deviation of the full range)**

The external clock source is adjusted to 2 GHz within 1 ppm accuracy. Therefore, the integral non-linearity is considered to be less than  $\pm 15$  ppm

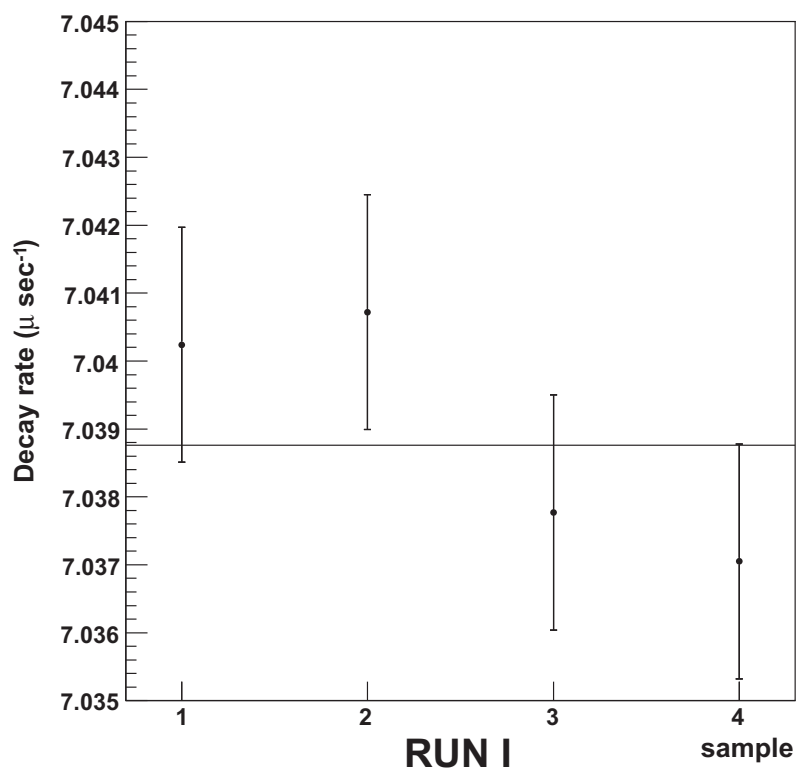


Figure 3.31: Decay rates of the four samples for RUN I. The bar of the data point represents the statistic error. The horizontal line shows the decay rate of the run.

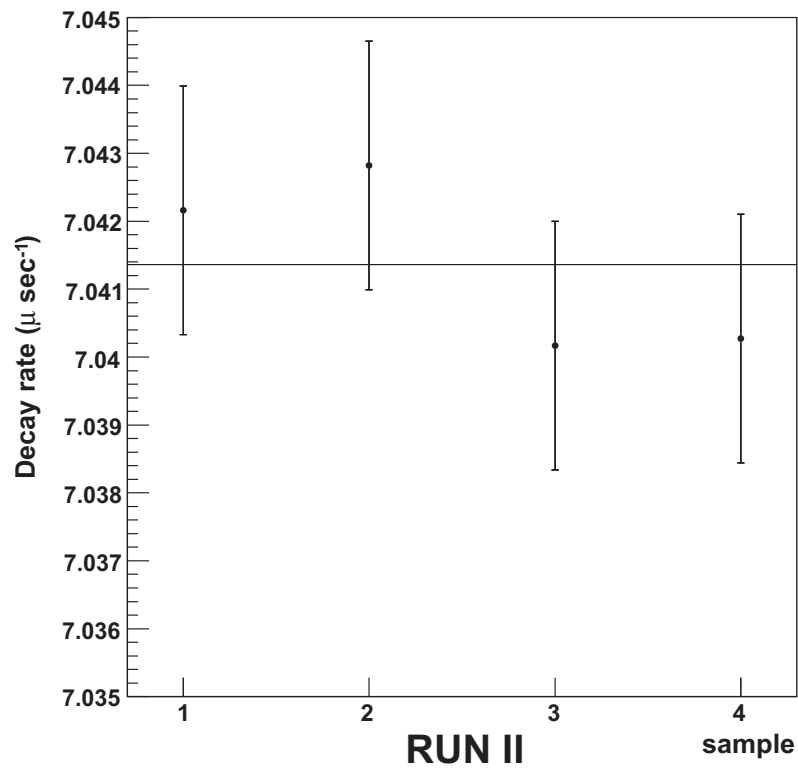


Figure 3.32: Decay rates of the four samples for RUN II. The bar of the data point represents the statistic error. The horizontal line shows the decay rate of the run.

corresponding to the bin width. The frequency of the clock is guaranteed to be stable within 3 *ppm* in one year, and within 2.5 *ppm* in the temperature  $-10\text{ }^{\circ}\text{C} \sim 50\text{ }^{\circ}\text{C}$ .

### Differential non-linearity (deviation of the bin width)

The intrinsic non-linearity is totally smeared in the time walk correction and the rebinning operation. Therefore, the effect of the DNL is considered to be negligible at the decay rate fitting.

### 3.5.2 Contamination of the Pile-up Events

For the YAP scintillator, the Base cut cannot be applied with  $\pm 4\sigma$  boundary. This is because the time dependence of the Base cut distorts the time spectrum as mentioned in Sec. 3.1.4. Then, the upper boundary of the Base cut is set to  $+140\sigma$ .

The effect of the contamination (about 0.1 %) can be estimated as follows. The energies of these events are slightly increased. Then the effective efficiency above 150 keV energy threshold is raised by 10 %. Consequently, the contribution to the decay rate is found to be less than 10 *ppm* (see Appendix B.3.2 for detailed discussion).

### 3.5.3 Subtraction of $3\gamma$ Energy Spectrum

The pick-off ratio  $\lambda_{pick}/\lambda_{3\gamma}$  is calculated with the counting method. The separation of the pick-off events and the  $3\gamma$  events is crucial for the counting method. The uncertainty of the separation comes from the statistics of the  $3\gamma$  events and the shape of the  $3\gamma$  spectrum. The shape of the  $3\gamma$  spectrum is related to the following factors.

- Monte Carlo simulation (all factors such as geometry, material, etc)
- $3\gamma$  SRT cut efficiency, which is evaluated with the data.
- resolution of Ge detector, which is measured with single  $\gamma$ -rays.
- response function, which is measured with  $^{85}\text{Sr}$  source.

These factors varies the  $3\gamma$  spectrum in their own manner and the propagations to the decay rate are different from each other.

But, one can estimate the uncertainty of the subtraction by making use of the following relation. Since the  $3\gamma$  spectrum sharply falls off at 511 keV, the deviation of the  $3\gamma$  spectrum varies only the left side of the residual pick-off peak. This relation is easily seen in Fig.3.33, where the normalization of the  $3\gamma$  spectrum is varied by  $\pm 1\%$ . Therefore, the asymmetry of the pick-off peak can be used to validate the subtraction of the  $3\gamma$  events.

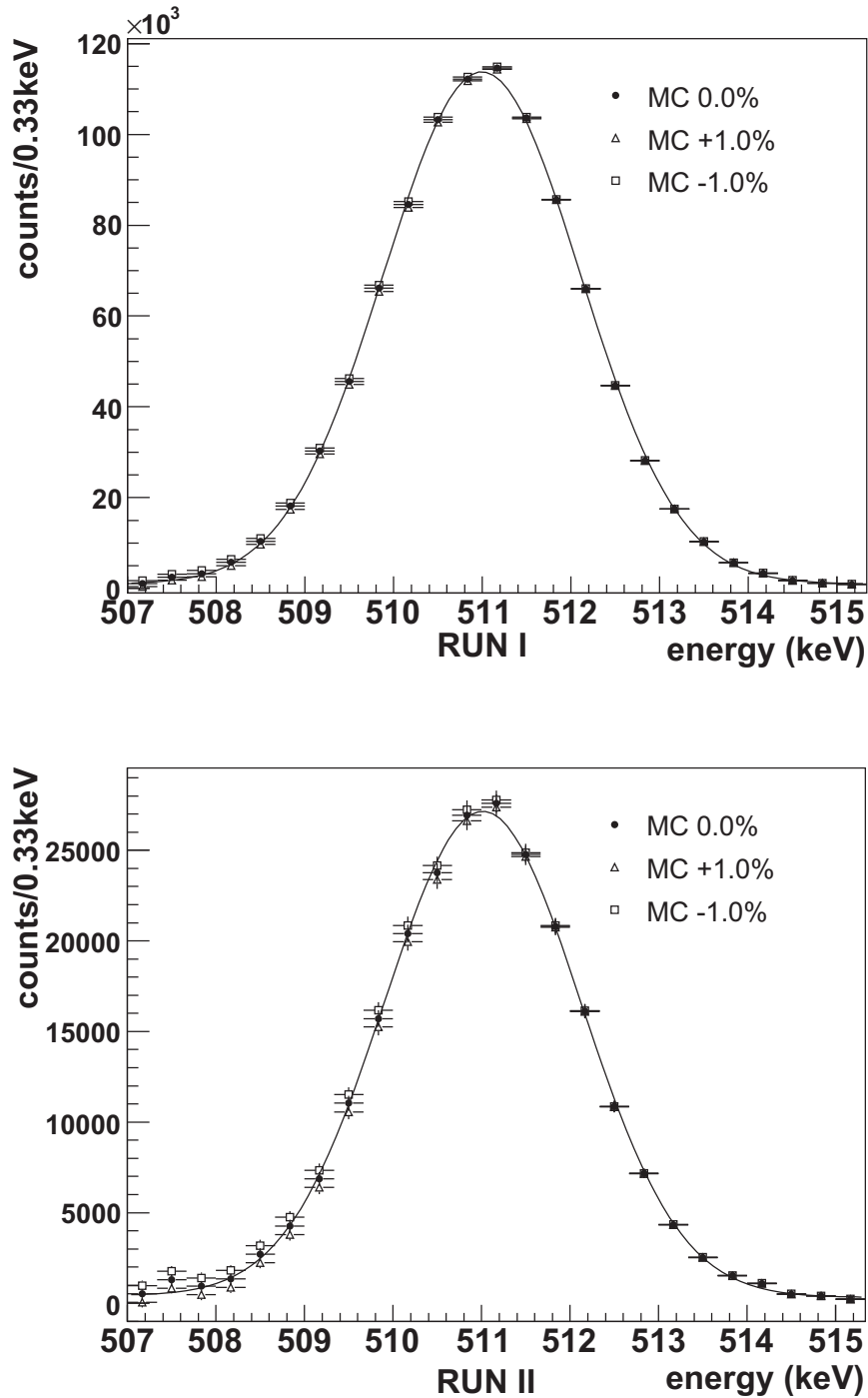


Figure 3.33: The pick-off spectrum with varied  $3\gamma$  normalization. The upper figure is the spectrum for RUN I and the lower figure is the spectrum for RUN II. The figure shows the pick-off spectra when the normalization of the  $3\gamma$  spectrum is varied by  $\pm 1\%$ . The left side of the peak is shifted according to the variation of the normalization.

The observed asymmetry of the pick-off peak is parameterized as,

$$\xi_{asym} = \left( \sum_{E=507.0 \text{ keV}}^{E<511.0 \text{ keV}} N(E) \right) / \left( \sum_{E>511.0 \text{ keV}}^{E=515.0 \text{ keV}} N(E) \right) \quad (3.15)$$

where  $N(E)$  represents the spectrum of the pick-off peak. Then, the  $\xi_{asym}$  parameter of the  $\pm 1$  % normalization is calculated as in Table 3.12, where the  $\xi_{asym}$  parameter for the prompt events is also shown. These relations

Normalization	-1.0% MC	$\pm 0.0\%$ MC	+1.0% MC	Prompt
RUN I	1.016 $\pm 0.005$	1.001 $\pm 0.005$	0.987 $\pm 0.005$	0.998
RUN II	1.025 $\pm 0.014$	0.984 $\pm 0.014$	0.937 $\pm 0.014$	0.997

Table 3.12: Summary of the  $\xi$ -parameters

are also shown in Fig. 3.34. Since the prompt events mainly consist of  $2\gamma$ , the  $\xi_{asym}$  parameter of the prompt events is a good indicator for the proper subtraction of the  $3\gamma$  events. In the figure, it is found that the  $\xi_{asym}$  parameter at the  $\pm 0.0$  % normalization is consistent with the  $\xi_{asym}$  parameter of the prompt events within  $\pm 1 \sigma$  error. The  $\pm 1 \sigma$  error of the  $\xi_{asym}$  parameter corresponds to  $\pm 0.33$  % normalization for RUN I and  $\pm 0.34$  % normalization for RUN II respectively. These values affect the decay rate by  $\pm 89$  ppm for RUN I and  $\pm 91$  ppm for RUN II, which is assigned as a systematic error.

### 3.5.4 Detection Efficiencies

#### Detection efficiency of Ge detector

The pick-off ratio  $\lambda_{pick}/\lambda_{3\gamma}$  is calculated from the event counts with the detection efficiency of Ge detector, which is introduced as  $\mathcal{F}$  factor. The uncertainty of  $\mathcal{F}$  factor comes from the following factors.

- response function, which is measured with  $^{85}\text{Sr}$  source.

The response function of Ge detector is evaluated with 514 keV single photon of  $^{85}\text{Sr}$  source. To estimate the uncertainty of the Monte Carlo simulation, the following parameter is introduced,

$$R_{\text{peak}} = \frac{\text{photoelectric peak}}{\text{photoelectric peak} + \text{compton free region}} \quad (3.16)$$

$$= \frac{\text{Number of events}(514 \text{ keV} \pm 4 \text{ keV})}{\text{Number of events}(483 \text{ keV} \sim 518 \text{ keV})} \quad (3.17)$$

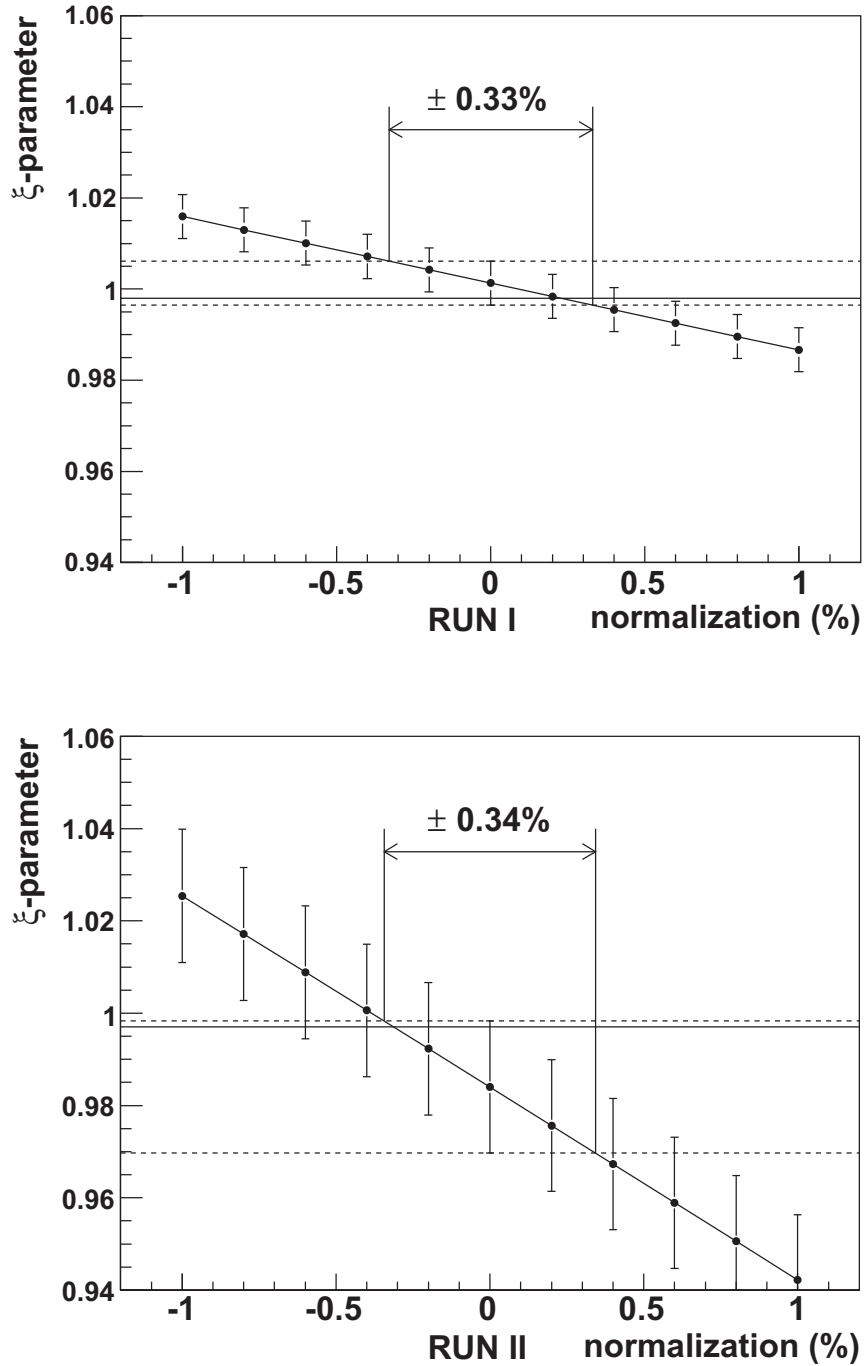


Figure 3.34:  $\xi$ -parameter with varied  $3\gamma$  normalization. The upper figure is the spectrum for RUN I and the lower figure is the spectrum for RUN II. The boundaries of the  $\pm 1 \sigma$  error from the  $\xi$ -parameter of the  $\pm 0.0 \%$  normalization is shown as dotted lines. This error corresponds to  $\pm 0.33 \%$  normalization for RUN I and  $\pm 0.34 \%$  normalization for RUN II. The  $\xi$ -parameter of the prompt events is also shown as a solid line.

This is because the counting efficiency of the pick-off events is related to the event number within  $\pm 4$  keV from photoelectric peak and sensitive to the tail of the photoelectric peak, whereas the counting efficiency of  $3\gamma$  events in the Compton free region is not sensitive to the response function around the photoelectric peak.

The difference between the measured data and the Monte Carlo simulation is summarized in Table 3.13. The maximum difference of 0.04% is assigned as a systematic uncertainty of  $\mathcal{F}$  factor.

	Ge0	Ge1
RUN I	$0.03 \pm 0.02$ %	$0.01 \pm 0.02$ %
RUN II	$0.04 \pm 0.02$ %	$0.01 \pm 0.02$ %

Table 3.13: The difference between the measured data and the Monte Carlo simulation

- Monte Carlo simulation (geometry, density, etc)

The response function of Ge detector is evaluated with 514 keV single photon. Then, the deviation of geometry and material, if exist, is incorporated into the response function. Therefore, remaining uncertainty is related to the silica material, which is introduced at the start of RUN. The density of the silica material is known at the start of RUN. The variation of the density during the RUN is conservatively estimated as 10 %. The 10 % variation of density leads to  $0.12 \pm 0.12$  % deviation of  $\mathcal{F}$  factor, which is assigned as a systematic error. For the RUN I, the systematic error is not assigned since the silica aerogel is in the solid state and the deviation of the density is negligibly small.

- SRT cut efficiency, which is evaluated with the data.

The precision of the  $3\gamma$  SRT cut efficiency is statistically limited since only the delayed time region can be used for the evaluation. The uncertainty of the absolute value in the region 480 keV $\sim$ 505 keV is 0.08 % for RUN I and 0.09 % for RUN II.

Above systematic errors and statistic error of Monte Carlo simulation 0.07 % are quadratically added. Then, the total error of  $\mathcal{F}$  factor is estimated as 0.11 % for RUN I and 0.27 % for RUN II. These errors of  $\mathcal{F}$  factor affect the decay rate by 33 ppm for RUN I and 28 ppm for RUN II, which is assigned as a systematic error.

### Detection efficiency of YAP scintillator

The detection efficiency of YAP scintillator is used for the decay rate fitting in the form of the ratio  $\varepsilon_{pick}/\varepsilon_{3\gamma}$ . The main factor of the uncertainty is the

response function of the YAP scintillator. The response function of the YAP scintillator is evaluated with 514 keV single photon of  $^{85}\text{Sr}$  source.

To estimate the uncertainty of the Monte Carlo simulation, the spectrum of 514 keV  $\gamma$ -ray is parameterized as,

$$R_{\text{peak}} = \frac{\text{photoelectric peak}}{\text{photoelectric peak} + \text{compton region}} \quad (3.18)$$

$$= \frac{\text{Number of events}(400 \text{ keV} \sim 700 \text{ keV})}{\text{Number of events}(150 \text{ keV} \sim 700 \text{ keV})} \quad (3.19)$$

The difference between the measured data and the Monte Carlo simulation is summarized in Table 3.14. The mean value of the difference is 2.0 % for RUN I and 1.3 % for RUN II, which is considered as a systematic uncertainty of the efficiency ratio  $\varepsilon_{\text{pick}}/\varepsilon_{3\gamma}$ . When the efficiency ratio  $\varepsilon_{\text{pick}}/\varepsilon_{3\gamma}$  is varied by that, the deviation of the decay rate is 64 *ppm* for RUN I and 19 *ppm* for RUN II, which is assigned as a systematic error.

	YAP0	YAP1	YAP2	YAP3
RUN I	1.1 %	3.4 %	1.5 %	—
RUN II	1.1 %	1.2 %	2.2 %	0.7 %

Table 3.14: The difference between the measured data and the Monte Carlo simulation

### 3.5.5 Other Sources of Systematic Errors

#### The Zeeman effect

In the presence of a magnetic field  $B$ , one of the o-Ps states is perturbed. The decay rate of the state is estimated as [32],

$$\lambda'_{\text{o-Ps}} = \lambda_{\text{o-Ps}} \left( 1 + \frac{\eta^2}{4} \frac{\lambda_{\text{p-Ps}}}{\lambda_{\text{o-Ps}}} \right) \quad (3.20)$$

where  $\eta = 4\mu B/\hbar\omega = B(\textit{gauss})/36287 \ll 1$ ,  $\mu$  is magnetic moment of the electron,  $\hbar\omega$  is the hyperfine structure splitting between o-Ps and p-Ps. As in Sec. 2.3.1, the absolute magnetic field is measured around the assembly. The measured value  $B = 0.5 \textit{ gauss}$  contributes to the decay rate by +5 *ppm*, which is assigned as a systematic error.

#### Three-photon annihilation of an electron-positron pair

The three-photon pick-off process can occur with a small relative ratio to the two-photon process. The relative ratio  $\sigma_{3\gamma}/\sigma_{2\gamma}$  can be estimated from

the decay rate ratio,

$$\sigma_{3\gamma}/\sigma_{2\gamma} = \frac{\lambda_{o\text{-Ps}} \times 3}{\lambda_{p\text{-Ps}} \times 1} \sim 1/378. \quad (3.21)$$

where  $\lambda_{o\text{-Ps}}$  and  $\lambda_{p\text{-Ps}}$  are the decay rate of o-Ps and p-Ps respectively. The factor 3 in numerator comes from the triplet states of o-Ps.

On the other hand, the pick-off events by the *spin-flip* effect (see Sec.2.1.1) do not have the  $3\gamma$  decay process. If the contribution of the *spin-flip* is neglected, the  $3\gamma$  pick-off events increase  $\mathcal{F}$  factor by 0.3 % and  $f_{\text{compton}}$  factor by 1 %. These changes decrease the decay rate by 91(33) ppm for RUN I(II).

### The Stark effect

As mentioned in Appendix A, the electric field on the grain surface of the  $\text{SiO}_2$  powder can decrease the decay rate. These contributions are estimated with simple models in Appendix A. For RUN I, typically  $-3$  ppm contribution is expected, while  $-4$  ppm is expected for RUN II.

### Excited state of Ps

The excited state ( $n=2$ ) of Ps is observed in the experiment utilizing the slow positron beam with a fraction of  $10^{-3}$ - $10^{-4}$  [58, 59].  $2P$  state immediately transits to  $1S$  state ( $\tau_p = 3.2$  ns). However,  $2S^3$  state, whose fraction is  $3/16$  of excited states, decays with a low decay rate of  $\lambda_{3\gamma}/8$ .

But in this experiment, positrons are much energetic and deeply enter into the bulk of the target material. Then, the positrons diffusing to the surface are considered to be well thermalized. In this case, the positrons cannot be emitted as the excited state Ps since its work function is positive owing to the small binding energy of 1.7 keV.

In addition, the excited state Ps is likely to be deexcited at the first collision on the  $\text{SiO}_2$  grain surface. Consequently, the excited state Ps cannot affect the time spectrum in the delayed region.

### 3.5.6 Summary of the Systematic Errors

Above systematic effects are summarized in Table 3.15. The total systematic error is calculated as a quadratic sum of them since they are considered to be independent with each other.

## 3.6 Results of the Present Measurement

From the analysis in this chapter, the following o-Ps decay rates are obtained for two runs,

Source of the Contributions	For RUN I ( <i>ppm</i> )	For RUN II ( <i>ppm</i> )
TDC module related error		
– Integral Non Linearity	< ± 15	< ± 15
Contamination of pile-up events		
– for Base cut	< – 10	< – 10
Pick-off Correction		
– 3 $\gamma$ subtraction	±89	±91
– Ge detector efficiency	±33	±28
– YAP scintillator efficiency	±64	±19
Other Sources		
– Zeeman effect	–5	–5
– Three-photon annihilation	–91	–33
– Stark effect	+3	+4
Total	–147 and +115	–104 and +98

Table 3.15: Summary of the systematic errors

for RUN I,

$$\lambda_{\text{o-Ps}}(\text{RUN I}) = 7.03876 \pm 0.0009(\text{stat.})_{-0.0010}^{+0.0008}(\text{sys.}) \mu\text{s}^{-1} \quad (3.22)$$

and for RUN II,

$$\lambda_{\text{o-Ps}}(\text{RUN II}) = 7.04136 \pm 0.0009(\text{stat.})_{-0.0007}^{+0.0007}(\text{sys.}) \mu\text{s}^{-1} \quad (3.23)$$

where the first error represents a statistic error, and the second one is for systematic. The values are shown in Fig. 3.35. The  $O(\alpha^2)$ -corrected QED prediction is also shown in the figure.

The discrepancy of the two runs is  $1.6 \sigma$ . Then it can be said that the two measurements with different types of silica material are consistent. In the calculation, the systematic error of the pick-off correction is considered to be not correlated between two runs.

The final result is obtained by combining these results of the two runs. The weighted average value with respect to the error is,

$$\lambda_{\text{o-Ps}} = 7.0401 \pm 0.0006(\text{stat.})_{-0.0009}^{+0.0007}(\text{sys.}) \mu\text{s}^{-1} \quad (3.24)$$

The total error is about 150 *ppm* and 1.6 times more precise than that of the previous measurement [37].

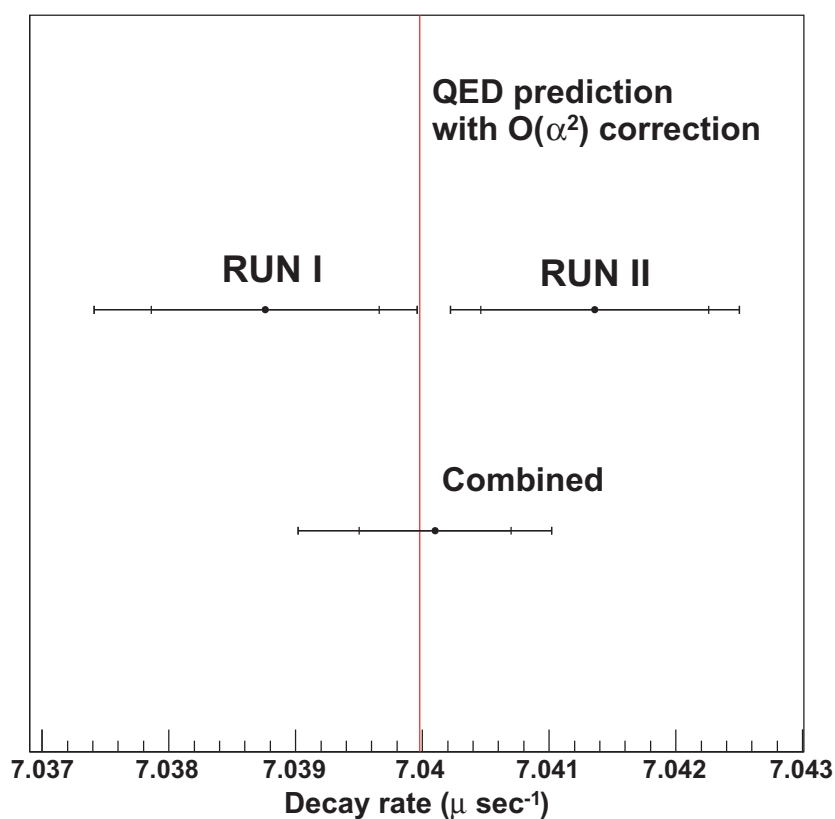


Figure 3.35: The results of the two runs and the combined result. The whole error bar shows the total error and the inside line represents the statistical error. The  $O(\alpha^2)$ -corrected NRQED prediction of  $7.039979 \mu \text{ s}^{-1}$  is also shown as the red vertical line.

## Chapter 4

# Discussion

In this chapter, the experimental meanings and the theoretical implications of the obtained results are discussed.

### 4.1 Experimental Meanings

#### 4.1.1 Solution of the Systematic Increase near the Prompt Peak

The direct pick-off correction method adopted in this experiment guarantees that all the pick-off contributions are completely corrected even when the pick-off ratio cannot be estimated in advance, or the pick-off ratio is time dependent. At this point, the direct correction method has the great advantage over the previous extrapolation method.

But unfortunately, the previous two measurements by this method observed the rapid rise of the decay rate near the prompt peak. The deviation reached  $500\text{ ppm}\sim 1000\text{ ppm}$  at  $60\text{ ns}$  fitting start time. This systematic error was not understood at that time and left room to doubt the obtained decay rate.

However, the results of the present measurements show no indication of this systematic rise. The change is attributed to the following improvements of the measurement.

- In the present measurement, the timing characteristics of  $\gamma$ -ray detectors are improved. For the measurement of the o-Ps time spectrum, fast inorganic scintillator YAP is introduced. Consequently, one can deny the possibility that the tail of the prompt events or the pile-up events distort the time spectrum near the prompt peak. For the measurement of the pick-off ratio, time walk correction and treatment of the SRT component is thoroughly studied. Then, more conservative approach is taken. Only the direct information such as measured rise-time is used to correct the time walk and the validity of the time walk

correction is evaluated with the measured data without silica target.

- In the present measurement, the validity of the electronics system is thoroughly investigated. In the end, the systematic deviation of the relative bin width is found in the KEK TDC. The cause of the deviation is a logic unit module fluctuated by the veto release signal just before  $T_0$ . The veto release signal is produced by the trigger system and the output of the logic unit is slightly correlated with the trigger timing. Consequently, the detector hit signal suffers from the fluctuation correlated with the trigger timing. Once the reason is understood, the deviation can be corrected with the calibration data by the random stop RUN.

In these improvements, the present measurement successfully confirms the validity of the direct pick-off correction method. Then, the obtained decay rate is considered to be reliable.

#### 4.1.2 Validation of the Fitting Start Time

The pick-off ratio can be obtained in the time region after 60 *ns*. This is because the prompt peak of the Ge detector extends up to 50 *ns*, which is confirmed with the measured data without silica target. However, the excellent time resolution of the YAP scintillator makes it possible that the time spectrum before 60 *ns* is fitted with the analytic form of the pick-off ratio, which is referred to as the thermalization function.

Fig. 4.1 shows the fitted decay rate with the fitting start time before 60 *ns*. It is found that the fitted decay rate is stable around 60 *ns* fitting start time. However the fitted decay rate is rapidly deviated before 40 *ns* for RUN I and 45 *ns* for RUN II. It can be understood as the following systematic effects.

##### Statistic error of the thermalization function

Before 60 *ns*, the pick-off ratio is calculated with the extrapolation of the thermalization function. As seen in Fig. 3.25 and Fig. 3.26, the uncertainty of the thermalization function is rapidly increased.

##### Systematic error of the thermalization function

For the thermalization function, the simplest form is introduced in Eq. 3.5. It is too simple to reproduce the thermalization process before 60 *ns*. Then, the systematic uncertainty is considered to be large in the extrapolated region. In fact, the thermalization function rapidly increases in the hatched region of the Fig. 4.1. Consequently, the decay rate fitting fails.

##### Systematic errors proportional to the pick-off ratio

Some systematic errors such as the error of the detector efficiency

are proportional to the pick-off ratio. Since the pick-off ratio rapidly increases before 60 *ns*, the propagation of these errors is much larger than the assigned value, which is evaluated at 60 *ns* fitting start time.

#### **Suppression by the anti-trigger coincidence**

A trigger may be suppressed by the anti-trigger hit of the accidental event. The margin of the anti-trigger coincidence is set to 30 *ns* in the measurement. Consequently, the time spectrum of the YAP scintillator before 30 *ns* is suppressed with the probability of the accidental event.

#### **Time walk correction of the plastic scintillator**

The time walk correction of the plastic scintillator is carried out with the Wide ADC value of the plastic scintillator. However the Wide ADC value correlates with the accidental activity within the gate width of 50 *ns*. Consequently, the small dip of the time spectrum is expected just before 50 *ns*. The amount does not exceed the accidental probability.

#### **The prompt peak of the YAP scintillator**

Practically, the prompt peak of the YAP scintillator is not normal gaussian function. This is because the time constant of the  $e^+$  annihilation in the plastic scintillator or the glass beaker is about 2 *ns*. For the simplicity, all the prompt events are assumed to annihilate with the time constant of 2 *ns*. It takes 20 *ns* for the prompt peak to decrease to the level of accidental distribution. Then, it takes another 20 *ns* to totally disappear.

Thus, one can conclude that indeed the fitted decay rate is rapidly deviated before 40 *ns* or 45 *ns*. the deviation is totally understood as the above systematic effects. Then, one can safely set the fitting start time at 60 *ns* where the above systematic effects are highly suppressed or do not exist.

### **4.1.3 Improvements of the Monte Carlo Simulation**

The Monte Carlo simulation plays a crucial role in this experiment. In the present measurement, the Geant4 based Monte Carlo simulation is introduced. It can handle the simulation of the positron and the simulation of the secondary particles. They are implemented in the previously used Monte Carlo simulation. But after some studies, it is found that the simulation does not reproduce the measured data and the discrepancy originates in the detector specific nature such as the optical photon collection efficiency, the charge collection efficiency and the slow rise-time component. Then, the following measures are taken.

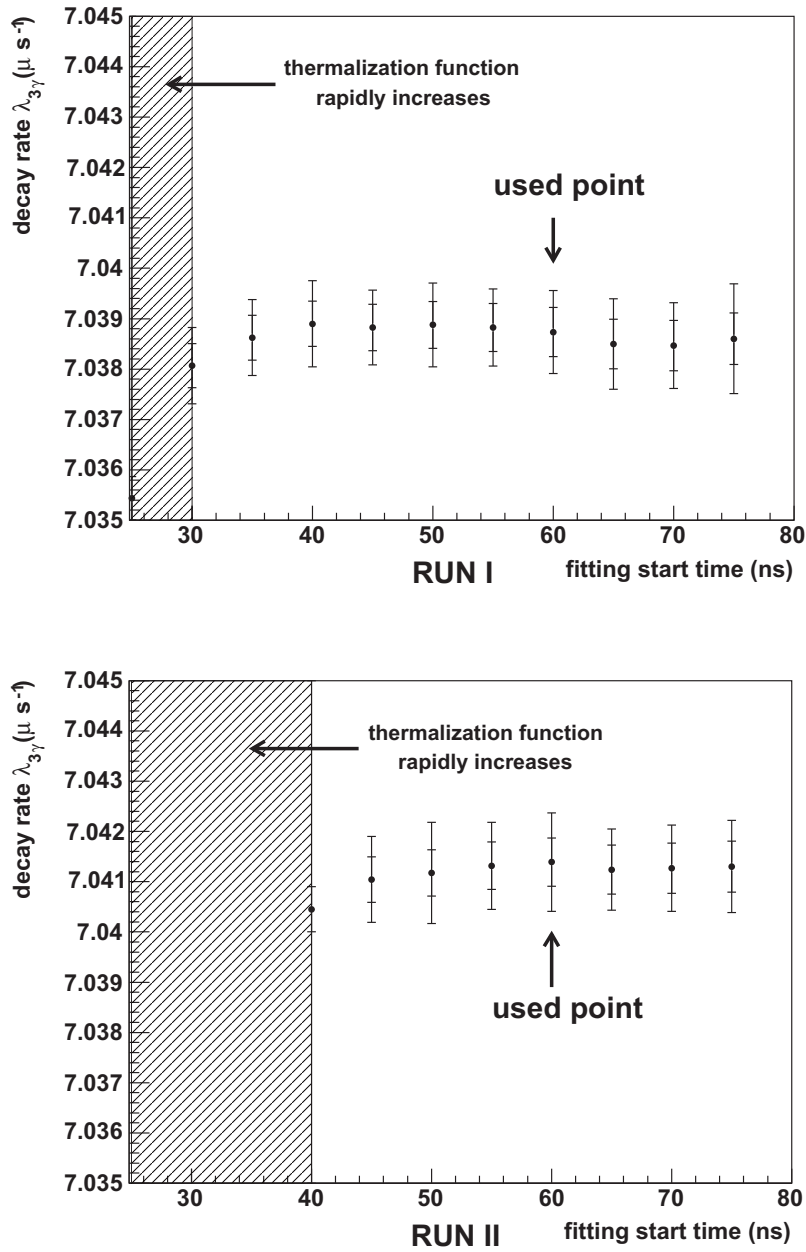


Figure 4.1: The fitted decay rate with the fitting start time before 80 ns. The upper figure shows the decay rate for RUN I. The lower figure shows the decay rate for RUN II. The error bars show only the statistic error and the inner lines represent the statistic error of the YAP time spectrum. In the left hatched region, the thermalization function rapidly increases.

- The response function is evaluated with the measured data and incorporated into the Monte Carlo simulation.
- The slow rise-time component of the Ge detector is cut with the measured rise-time information in the offline analysis. Then, the cut efficiency is evaluated with the run data and applied to the Monte Carlo simulation data. In fact, this strategy is employed in the previous measurement.

The obtained Monte Carlo simulation more realistically estimates the detection efficiency and the shape of the  $3\gamma$  spectrum. It can suppress the uncertainty of the pick-off correction and the energy window dependence. In fact, the previously observed energy window dependence is disappeared in the present measurement.

#### 4.1.4 Dependence on the Two Types of Silica Material

In the previous measurements, the two types of silica powder was used for a systematic test of the method. One is the hydrophilic silica powder and low density, another is the hydrophobic silica powder and higher density. The results of the two measurements are consistent with each other.

In the present measurements, the two types of silica material are used. One is the silica aerogel and solid state, another is the silica powder. They have the almost same density. However, the pick-off ratios are different with each other by a factor of 3 as clearly seen in Fig. 4.2. The reason of this difference is not fully understood. But it can be said that the pick-off ratio is dependent on not only density but also internal structure, such as the grain size, the aggregate structure, the surface, etc. The measured decay rate is consistent with each other. Then, one can conclude that the direct pick-off correction method is a robust technique for the various materials whose internal structure is not fully known, whereas the extrapolation method which assumes the linearity to the density is not safe in this situation.

## 4.2 Theoretical Implications

As seen in Fig.4.3, the present measurement agrees with the recent three measurements from 1995. They include the two measurements of our group by the direct pick-off correction method and the one measurement of Michigan group by the improved extrapolation method. Then it can be said that the experimental values by the different method does not conflict with each other in about 200 ppm level.

The present measurement disagrees with the old measurements before 1990. The reason of the discrepancy is the one mentioned in Sec. 2.1.2. The *orthopositronium lifetime puzzle* is already solved.

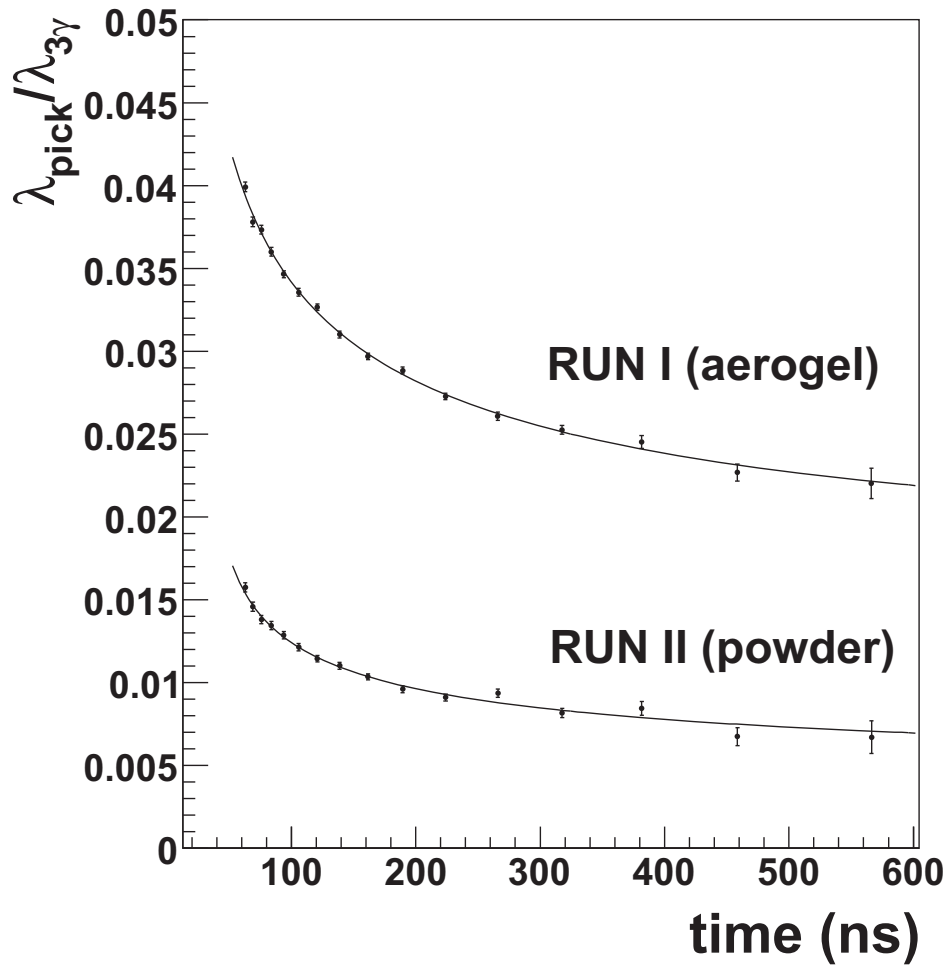


Figure 4.2: The measured pick-off ratios with two types of silica material. The pick-off ratio of silica aerogel is 3 times larger than that of silica powder.

The result of the present measurement is in good agreement with the  $O(\alpha^2)$ -corrected QED prediction as in the figure. In addition, the precision of the present measurement, about 150 *ppm*, enables us to discuss the non-logarithmic  $\alpha^2$  correction on the o-Ps decay rate. As in Fig. 4.4, the result of the present measurement differs from the  $O(\alpha^2)$ -corrected QED prediction by  $0.1 \sigma$  while differs from the QED prediction without  $O(\alpha^2)$  correction by  $1.7 \sigma$ . When the recent four measurements after the solution of the *orthopositronium lifetime puzzle* are combined, the world average of the decay rate is obtained as,

$$\lambda_{\text{o-Ps}} = 7.0401 \pm 0.0007(\text{total}) \quad (4.1)$$

where the errors of the four measurements are considered to be not correlated with each other. The world average of the decay rate is in good agreement with the  $O(\alpha^2)$ -corrected QED prediction and the discrepancy to the QED prediction without  $O(\alpha^2)$  correction is  $2.6 \sigma$ . Then, it can be said that the world average favors the  $O(\alpha^2)$ -corrected QED prediction rather than that of  $O(\alpha)$  correction.

In fact, the absolute value of the  $O(\alpha^2)$  correction is not proved with the accuracy of the present measurement. Though the theoretical group which have performed the complete calculation of the  $O(\alpha^2)$  term states a *ppm* level uncertainty, the calculation has not been verified by other authors. Then, the more accurate measurements of the o-Ps decay rate are expected.

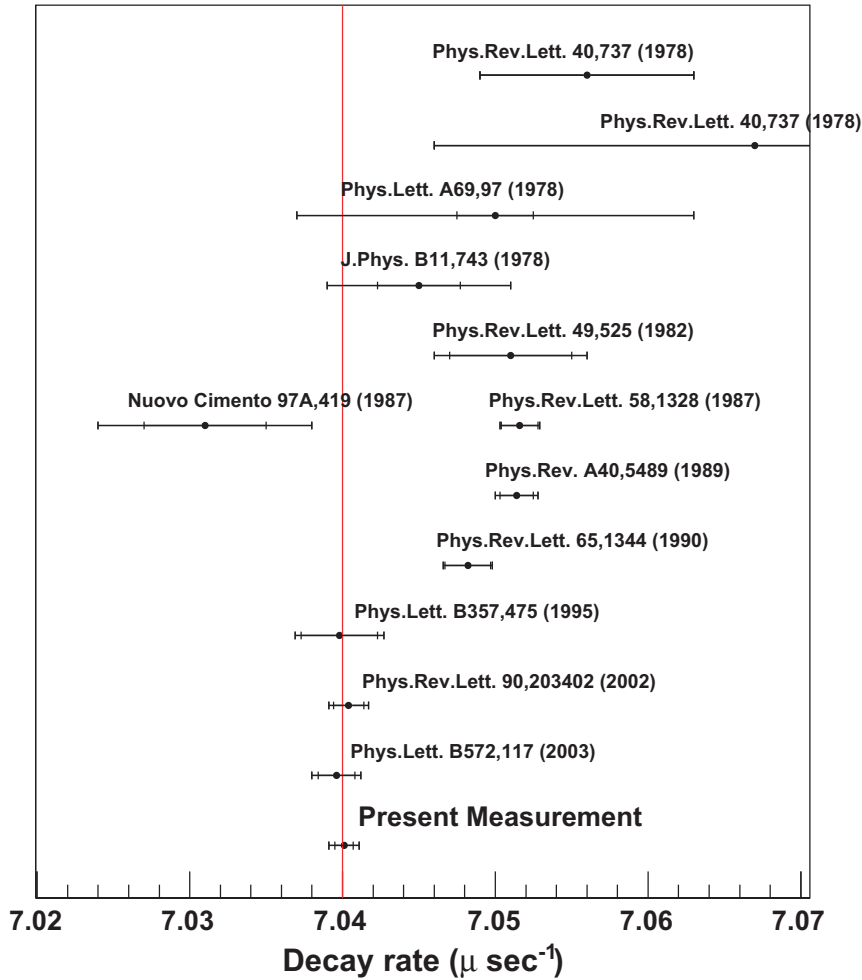


Figure 4.3: The history of the o-Ps decay rate measurements including the present measurement. The each error bar shows the total error of the measurement and the inside line represents the statistic error. The red vertical line shows the  $O(\alpha^2)$ -corrected NRQED prediction of  $7.039979\mu\text{s}^{-1}$ .

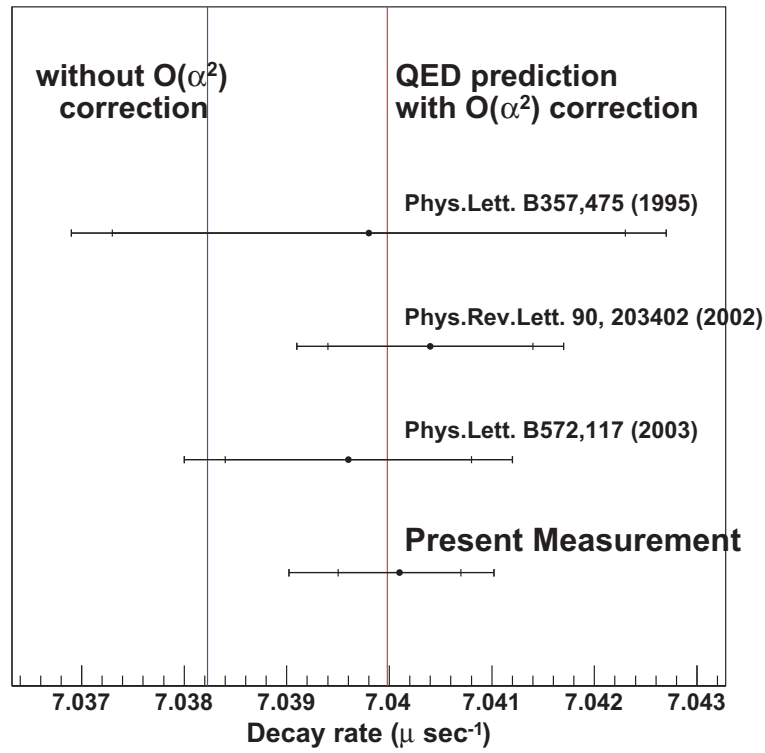


Figure 4.4: The relation between the resent measurements and the theoretical predictions. The red vertical line shows the  $O(\alpha^2)$ -corrected NRQED prediction of  $7.039979\mu\text{s}^{-1}$ . The blue vertical line shows the QED prediction without  $O(\alpha^2)$  correction, that is  $7.038226\mu\text{s}^{-1}$ .

# Chapter 5

## Conclusions

To test the bound state QED, especially the  $O(\alpha^2)$  correction term, the orthopositronium decay rate is newly measured. The features of the present measurement are as follows.

- The setup is newly constructed on the base of the fast inorganic scintillator YAP.
- The positronium formation assembly and the trigger system are totally refined.
- The Monte Carlo simulation is made on the base of the Geant4 package. The detector specific nature is also reproduced by incorporating the response function.

In the present measurement, the two runs are performed with the different types of silica target. The following results are obtained.

- The systematic increase near the prompt peak is understood and solved.
- Other systematic errors such as the energy window dependence and the uncertainty of the detection efficiency are highly suppressed.
- The results of the two runs are consistent with each other, even though they have the totally different pick-off ratios.
- The combined result achieves the total error of about 150 *ppm* and agrees with the  $O(\alpha^2)$ -corrected QED prediction.

In addition, the world average of the decay rate is in good agreement with the  $O(\alpha^2)$ -corrected QED prediction and the discrepancy to the QED prediction without  $O(\alpha^2)$  correction is  $2.6 \sigma$ . Then, one can conclude that the world average of the decay rate favors the  $O(\alpha^2)$ -corrected QED prediction rather than that of  $O(\alpha)$  correction.

# Appendix A

## Stark Shift

In this appendix, Stark shift of the decay rate is discussed. Most of the calculations are quoted from the reference [38].

### A.0.1 Stark Effects on o-Ps Decay Rate

The decay rate of o-Ps is proportional to the Ps wave-function at the origin, which is a flux factor of  $3\gamma$  decay.

$$\lambda_{3\gamma} \propto |\phi(r=0)|^2. \quad (\text{A.1})$$

If a uniform electric field  $E$  is applied to the Ps, the wave function of the Ps,  $\psi$ , is perturbed to be,

$$\psi = \psi_0 + E\psi_1 + E^2\psi_2 + \dots, \quad (\text{A.2})$$

where  $\psi_0$  is the unperturbed ground state wave function, and  $\psi_1, \psi_2, \dots$  stand for the higher order perturbed terms. Simple calculation by the perturbation method shows the relative shift of the decay rate as a function of  $E$  [60],

$$\frac{\Delta\lambda_{3\gamma}}{\lambda_{3\gamma}} = E^2 \frac{|\psi_1|^2}{|\psi_0|^2} \quad (\text{A.3})$$

$$= 248 \cdot (E/E_0)^2, \quad (\text{A.4})$$

where  $E_0 = m_e^2 e^5 / \hbar^4 \approx 5.14 \times 10^9 \text{ V/cm}$ , and  $E$  is the electric field sensed by the Ps during its lifetime.

### A.0.2 Contribution of Charge on Primary Grains

The charges on the silica materials are measured with a static electricity sensor [61]. The measured values are  $3(1) \times 10^{-9} \text{ [C/g]}$  for silica aerogel and less than  $1 \times 10^{-9} \text{ [C/g]}$  for silica powder.

Provided that the primary grains and the electric charges are uniformly distributed, the volume  $L^3$  which one electron occupy on average is estimated as,

$$L^3 = \frac{1.6 \times 10^{-19}[C]}{3 \times 10^{-9}[C/g] \cdot 0.03[g/cc]} \sim 1.8 \times 10^{-9}[cc] \quad (\text{A.5})$$

If the distance between the Ps and the electron is  $x$ , the square of the electric field sensed by the Ps would be,

$$\begin{aligned} |E|^2 &= \left( \frac{e}{4\pi\epsilon_0 x^2} \right)^2 \\ &= \frac{\tilde{e}^2}{x^4} \quad \left[ \tilde{e} = 1.4 \times 10^{-9} [V \cdot m] \right]. \end{aligned} \quad (\text{A.6})$$

Since the Ps is freely moving across the whole area between the grains, the average field sensed by the Ps should be estimated by averaging over the whole volume as,

$$\begin{aligned} \overline{|E|^2} &= \int dV |E|^2 / L^3 \\ &= 4\pi \int_{\epsilon}^L dx x^2 \frac{\tilde{e}^2}{x^4} / L^3 \\ &\simeq \frac{4\pi\tilde{e}^2}{\epsilon L^3}, \end{aligned} \quad (\text{A.7})$$

where  $\epsilon$  is a minimum distance between the Ps and electron. Bohr radius of the Ps  $r_{Ps} = 1.1 \times 10^{-10} [m]$  (twice the Bohr radius of atomic hydrogen) is a good approximation for  $\epsilon$ , since the Ps in the free space keeps away from the grain surface with a potential as [62],

$$V(x) = V_0 e^{-x/r_{Ps}} \quad (\text{A.8})$$

where  $V_0$  is the work function of Ps (of order 1eV).

Thus, an average of the squared electric field would be,  $\overline{|E|^2} = 1.3 \times 10^8 [V^2/m^2]$ . From Eq. (A.4), this could contribute to the decay rate only by  $1.2 \times 10^{-7}$  ppm level. Clearly we can neglect this term.

### A.0.3 Contribution of Dipole Moment on the Surface of Grains

SiO<sub>2</sub> powders have mainly two types of functional groups, silanol groups (–Si (OH)) and siloxan groups (–Si (O) Si–). The hydrophilia of the powder is attributed to these silanol groups. In order to obtain the hydrophobe characteristics, these groups are substituted with other functional groups such as, the tri-methyl-silyl groups, the dimethyl-silyl groups, etc.

The typical density of the silanol groups on the grain surface are investigated, 2.5 /nm<sup>2</sup> for hydrophilic silica and 0.44 /nm<sup>2</sup> for hydrophobic silica. Figure A.1 shows the schematic diagram of one SiO<sub>2</sub> grain. The silanol

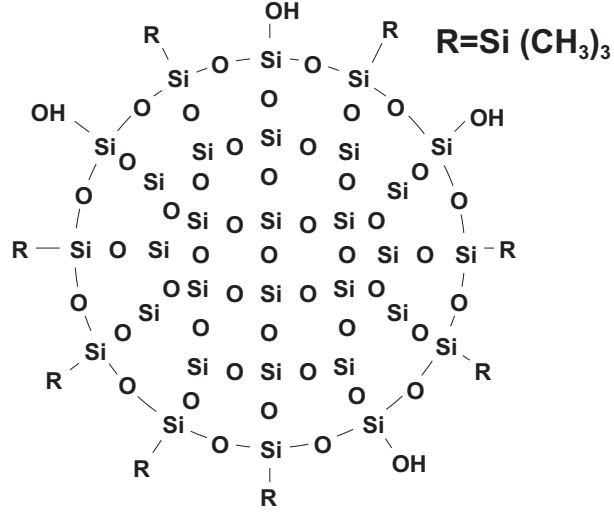


Figure A.1: Schematic diagram of  $\text{SiO}_2$  grain. Part of the surface functional groups are substituted, while there are still silanol groups left.

groups are existing on the surface of the grain. A typical size of dipole moment for the groups  $-(\text{OH})$  is  $1.7 \times 10^{-18} [\text{esu} \cdot \text{cm}]$  [63].

For the sake of the simplicity, it is assumed that the dipole moment  $\vec{p}$  is directed outward on the surface of the grain as illustrated in Fig. A.2. Then, the electric field at the point  $O$  outside the grain is expressed as,

$$\vec{E} = \frac{1}{4\pi\epsilon_0} \cdot \frac{3(\vec{n} \cdot \vec{p}) \cdot \vec{n} - \vec{p}}{R_0^3} \quad (\text{A.9})$$

The squared electric field would be,

$$\begin{aligned} |E|^2 &= \frac{p^2}{R_0^6} (3 \cos^2 \alpha + 1) \\ &= \dots \\ &= \frac{p^2}{R_0^8} (R_0^2 + 3(r - R \cos \theta)^2) \end{aligned} \quad (\text{A.10})$$

Defining the area density of the silanol-group as  $\sigma$  and integrating over the surface of one grain, the squared electric field at the position  $O$  would be,

$$\begin{aligned} |E|_o^2 &= 2\pi\sigma r^2 \int_0^\pi \sin \theta d\theta |E|^2 \\ &= 2\pi\sigma r^2 p^2 \int_{-1}^1 dx \left( \frac{1}{R_0^6} + 3 \frac{(r + Rx)^2}{R_0^8} \right) \\ &\quad (\text{substituted } x \text{ as } x = -\cos \theta). \end{aligned} \quad (\text{A.11})$$

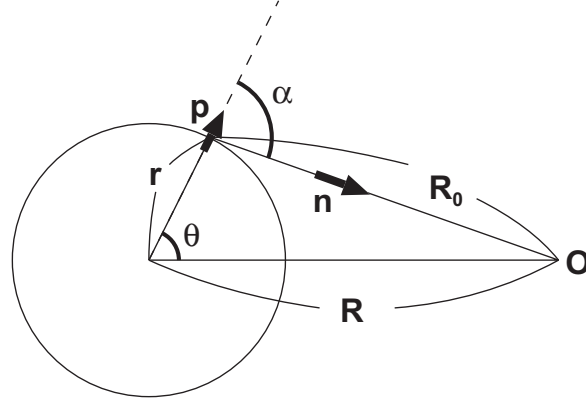


Figure A.2: A definition of the variables used for calculation in the context.  $\vec{n}$  is a unit vector directing from dipole moment  $\vec{p}$  to the observing point  $O$ .

In the end, the following equation is obtained.

$$|E|_o^2 = \pi\sigma p^2 \frac{r}{R} \left( \frac{3}{2} \left( \frac{1}{(R-r)^4} - \frac{1}{(R+r)^4} \right) - \frac{1}{2r} \left( \frac{1}{(R-r)^3} - \frac{1}{(R+r)^3} \right) + \frac{1}{4Rr} \left( \frac{1}{(R-r)^2} - \frac{1}{(R+r)^2} \right) \right) \quad (\text{A.12})$$

As in the previous section, the Ps is assumed to be freely moving across the grains. However in this case, the Ps continues to collide with the grains. Then, average distance is calculated as a mean free path between the grains,  $\bar{L}$ , which has been already obtained as in Table 2.1. Thus the integration is carried out in one dimension from the nearest distance to the powder  $\varepsilon$  (again the Bohr radius of Ps is used as  $\varepsilon$ ), to the mean distance between the grains  $\bar{L}$ .

Integrating Eq. (A.12) by variable  $R$  ( $r + \varepsilon \leq R \leq \bar{L}$ ), Almost all contribution comes from the first term of Eq. (A.12) as  $R$  approaches to  $r + \varepsilon$ . Thus, the average squared electric field would be,

$$\begin{aligned} \overline{|E|_o^2} &= \int_{r+\varepsilon}^{\bar{L}} dR |E|_o^2 / \bar{L} \\ &= \frac{3\pi\sigma p^2 r}{2\bar{L}} \int_{r+\varepsilon}^{\bar{L}} dx \frac{1}{x(x-r)^4} \\ &\simeq \frac{3\pi\sigma p^2 r}{2\bar{L}} \cdot \frac{1}{r} \left[ \frac{1}{-3(x-r)^3} \right]_{r+\varepsilon}^{\bar{L}} \\ &\simeq \frac{\pi\sigma p^2}{2\bar{L}\varepsilon^3}. \end{aligned} \quad (\text{A.13})$$

For the silica aerogel (SP-7), the average squared electric field  $\overline{|E|_o^2} =$

$2.2 \times 10^{16} [V^2/m^2]$  is obtained. From the Eq. (A.4), one can estimate the contribution of Stark shift to be 2.6 *ppm* of the decay rate.

For the silica powder (R972CF), the average squared electric field  $\overline{|E|_0^2} = 2.2 \times 10^{16} [V^2/m^2]$  is obtained. Then, one can estimate the contribution of Stark shift to be 3.7 *ppm* of the decay rate.

## Appendix B

# Expected Time Spectrum

The expected time spectrum is discussed in the following sections. The situation is rather complicated when the conditions of the trigger and the effects of the several cuts are taken into account.

### B.1 Probability of Accidental Events

First of all, the probability of accidental events around a trigger is discussed in this section. The trigger scheme of this experiment is

- The first hit of the trigger plastic scintillator from the main latch reset is a trigger candidate.
- Only when the event does not hit the anti-trigger, the trigger is accepted.
- The second trigger signal is blocked by the main latch system, even if the above trigger condition is met.

The accidental events which hit the anti-trigger are uniformly distributed around the trigger. This is because the accidental event with anti-trigger hit does not make a trigger and does not correlate with the trigger signal just like environmental background events. But, considering the effect of the anti-trigger, the accidental event with anti-trigger hit cannot exist within the width of anti-trigger veto from a trigger. The width of anti-trigger veto is 150 ns and its margin from the trigger signal is 30 ns. Then, the probability of the accidental event with anti-trigger hit is

$$P_{\text{with}}(t) = \begin{cases} 0 & \text{when } -120 \text{ ns} < t < 30 \text{ ns} \\ C_{\text{with}} & \text{when } t < -120 \text{ ns}, 30 \text{ ns} < t \end{cases} \quad (\text{B.1})$$

where  $C_{\text{with}}$  is a constant value determined by the event rate accompanying anti-trigger hit.

On the other hand, the accidental event which does not hit the anti-trigger is a candidate of trigger and correlates with the trigger signal. Indeed the probability after the trigger is uniform like the events with anti-trigger hit, the probability before the trigger must be small due to the first hit condition. The accidental events without anti-trigger hit are allowed only when the events occur before the main latch reset. The main latch reset occurs before the trigger signal with the following probability.

$$P_{\text{reset}}(t) = C_{\text{reset}} \exp(R_{\text{trig}} \cdot t) \quad (\text{B.2})$$

where the exponential function comes from the first hit condition and  $R_{\text{trig}}$  is the trigger rate. An accidental event without anti-trigger hit at  $t = t'$  is allowed only when the main latch reset comes in the time region from  $t'$  to 0. Thus, the probability of accidental events without anti-trigger hit is expressed as,

$$P_{\text{without}}(t') = \begin{cases} C_{\text{without}} \int_{t'}^0 P_{\text{reset}}(t) dt \sim -C'_{\text{without}} R_{\text{trig}} \cdot t' & \text{when } t' < 0 \\ C'_{\text{without}} & \text{when } t' > 0 \end{cases} \quad (\text{B.3})$$

The probability  $P_{\text{with}}(t)$  and  $P_{\text{without}}(t)$  is also shown in Fig. B.1. In the figure, the probability  $P_{\text{without}}(t)$  remains at 0 in the time region from  $-50 \text{ ns}$  to  $0 \text{ ns}$ . This is because the trigger logic signal has the width of  $50 \text{ ns}$  and the succeeding signal within  $50 \text{ ns}$  does not produce a trigger edge in the discriminator.

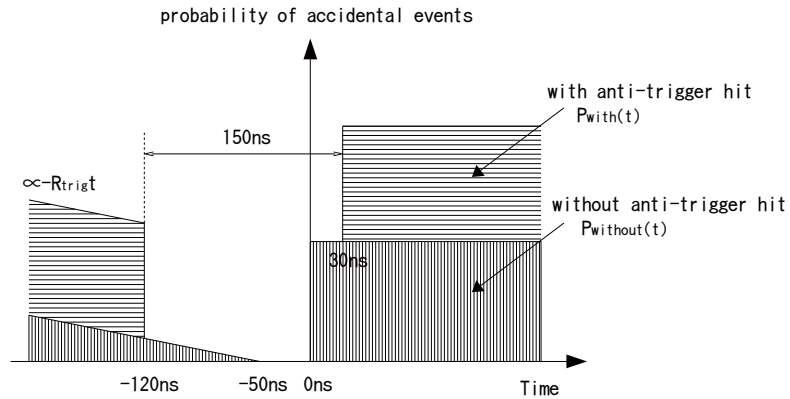


Figure B.1: Probability of accidental events around the trigger signal. The accidental events with and without anti-trigger hit have the different probability.

In the above discussion, the trigger efficiency of  $\beta^+$  decay events is considered as 100 %. Practically, less than 10 % of them are not triggered and forms the flat distribution over the trigger.

Another factor comes in the offline analysis. The Base cut of the trigger plastic scintillator suppress the accidental events just before the incident trigger. But, the accidental events before the trigger are already suppressed as seen in the figure.

## B.2 Expected Time Spectrum

In this section, the expected time spectrum of  $\gamma$ -ray detectors are discussed. Firstly, the  $\gamma$ -rays hit the detectors in this experiment are classified into following three groups according to their time distribution, which is shown in Fig. B.2.

- A.** The  $\gamma$ -rays of Ps which correlate with the trigger. These events consist of the  $2\gamma$  events at  $T_0$  and the  $3\gamma$  events which decay exponentially from  $T_0$ .
- B.** The 1077 keV nuclei- $\gamma$ , the positron and their secondary particles such as electrons and bremsstrahlung- $\gamma$ 's which correlate with the trigger. These events are concentrated at  $T_0$ .
- C.** The accidental events which do not correlate with the trigger. These events consist of the positron source related events and the environmental backgrounds. The former is discussed in the previous section and the latter is rather small and completely flat distribution.

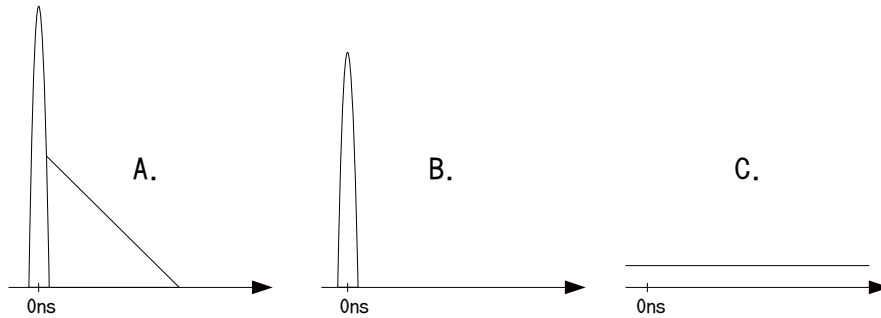


Figure B.2: Time distribution of the the  $\gamma$ -rays. The  $\gamma$ -rays which hit the detectors in this experiment are classified into three groups. **A.** Ps events, **B.** source related events, **C.** accidental events.

The group **A** and **B** are restricted to at most one event for a trigger, whereas the group **C** can occur many times for a trigger. The probabilities

of these group are denoted by  $P_A$ ,  $P_B$  and  $P_C$ .  $P_C$  is much smaller than  $P_A$  and  $P_B$ .

Then, all the cases of event are expressed as

$$(\mathbf{A} + \overline{\mathbf{A}})(\mathbf{B} + \overline{\mathbf{B}})(\mathbf{C} + \overline{\mathbf{C}})^\infty \quad (\text{B.4})$$

where  $\overline{\mathbf{A}}$ ,  $\overline{\mathbf{B}}$  and  $\overline{\mathbf{C}}$  denote that the detector does not detect  $\mathbf{A}$ ,  $\mathbf{B}$  and  $\mathbf{C}$  respectively. The term which includes  $\overline{\mathbf{A}}$ ,  $\overline{\mathbf{B}}$  or  $\overline{\mathbf{C}}$  decrease its probability by a factor of  $\overline{P_A}=1-P_A$ ,  $\overline{P_B}=1-P_B$ ,  $\overline{P_C}=1-P_C \sim 1$ . Thus, the above form leads to

$$\overline{P_B}\mathbf{A}(\overline{\mathbf{C}} + \mathbf{C})^\infty + \overline{P_A}\mathbf{B}(\overline{\mathbf{C}} + \mathbf{C})^\infty + \overline{P_A}\overline{P_B}\mathbf{C}(\overline{\mathbf{C}} + \mathbf{C})^\infty + \mathbf{A}\mathbf{B} \quad (\text{B.5})$$

The multiplied terms such as  $\mathbf{A}\mathbf{B}$  express the pile-up events and have their own time distribution.

### B.2.1 Pile-up by the Accidental Events $\sim \mathbf{X}(\overline{\mathbf{C}} + \mathbf{C})^\infty$

The first three terms of the form  $\mathbf{X}(\overline{\mathbf{C}} + \mathbf{C})^\infty$  denote the time distribution of  $\mathbf{X}$  under the accidental backgrounds. If two signals overlap with each other, the pile-up cuts reject the event in the offline analysis. Then, the probability of  $\mathbf{X}$  without the accidental event, denoted by  $\mathbf{X}\overline{\mathbf{C}}^n$ , is a dominant contribution on the observed spectrum. The probability of  $\mathbf{X}(\overline{\mathbf{C}} + \mathbf{C})^\infty$  is already known such as a exponential function for  $\mathbf{X} = \mathbf{A}$ . The probability of  $\mathbf{X}\overline{\mathbf{C}}^n$  is considered to be a modification of the intrinsic probability. This is expressed as

$$\mathbf{X}\overline{\mathbf{C}}^\infty = \mathbf{X}(\overline{\mathbf{C}} + \mathbf{C})^\infty \times S(t) \quad (\text{B.6})$$

where the function  $S(t)$  is a suppression factor depending on the detection time of  $\mathbf{X}$ .

The accidental events spoil the event in the following two situations.

- The accidental events hit the detector around the timing of  $\mathbf{X}$  hit. The overlapped events are suppressed by the Base cut and the Narrow-Wide cut in the offline analysis. These range are denoted by  $t_b$  and  $t_{nw}$  respectively
- The accidental events hit the detector before the  $\mathbf{X}$  hit. The detector system accepts only the first hit from the latch reset.

Therefore, the time region in which the accidental hit spoils the  $\mathbf{X}$  event at  $t$  is

$$0 \sim t + t_{nw} \quad \text{when } t > t_b \quad (\text{B.7})$$

$$t - t_b \sim t + t_{nw} \quad \text{when } t < t_b \quad (\text{B.8})$$

which is also shown in Fig. B.3. Practically, the boundary between these two cases is shifted by the margin of latch reset from  $T_0$ , which is 50 ns in

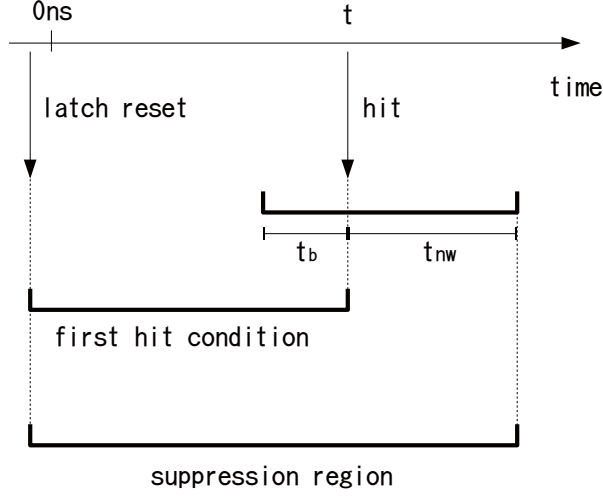


Figure B.3: The suppression region in which accidental events spoil the event. The events with accidental hits are suppressed by the pile-up cuts. The events are also suppressed through the first hit condition.

this experiment. When the above time region is denoted by  $t_{\text{start}} \sim t_{\text{end}}$ , the suppression factor is calculated with

$$S(t) = 1 - \int_{t_{\text{start}}}^{t_{\text{end}}} (\mathbf{C}^n \text{ terms}) \sim 1 - \int_{t_{\text{start}}}^{t_{\text{end}}} \mathbf{C} \quad (\text{B.9})$$

The probability of the accidental  $\mathbf{C}$  is complicated around the trigger signal. But, if the probability is a flat distribution, the suppression factor leads to

$$S(t) = e^{-(t_{\text{end}} - t_{\text{start}})} \quad (\text{B.10})$$

Then, the time spectrum of  $\mathbf{X}$  is obtained as

$$\mathbf{X}\overline{\mathbf{C}}^\infty = P_{\mathbf{X}}(t) \times S(t) \quad (\text{B.11})$$

To be precise, the energy distribution and the solid angle must vary among the accidental events, such as the events with anti-trigger hit, the events without anti-trigger hit and the environmental backgrounds. But, the effect is considered to be small.

The another term  $\mathbf{X}\mathbf{C}$  is usually rejected as a overlapped event. But, this term may remain in the following two cases. The effect of the contaminations which pass through the pile-up cuts are discussed later.

- If the detector has fast timing nature like YAP scintillator, the data taking of the accidental event may be completed before the hit of  $\mathbf{X}$ .

The probability is expressed as

$$\mathbf{XC} = P_{\mathbf{C}}(t) \times \int_{t+t_{\text{nw}}}^{\infty} P_{\mathbf{X}}(t') dt' \quad (\text{B.12})$$

where  $t$  is the timing of the accidental hit and the measured energy is the one of the accidental event.

- when the amplitude of the signal  $\mathbf{X}$  is less than the threshold value, the accidental hit after the  $\mathbf{X}$  is accepted as a accidental events. The time spectrum is not just the accidental's flat distribution and affected by the time distribution of  $\mathbf{X}$  through the Base cut. The probability is expressed as,

$$\mathbf{XC} = P_{\mathbf{C}}(t) \times \int_{-\infty}^{t-t_{\text{b}}} dt' \int_0^{E_{\text{thr}}} dE P_{\mathbf{X}}(t', E) \quad (\text{B.13})$$

Therefore, a part of the accidental's flat distribution is considered to be suppressed near the prompt peak.

### B.2.2 Pile-up Events with the Prompt Signal $\sim \mathbf{AB}$

The pile-up events with the prompt signal is not a problem since the events are triggered at  $T_0$  and do not affect the time spectrum in the delayed region. But, the special care must be taken if the amplitude of the prompt signal is less than the threshold level. In this case, the time spectrum of  $\mathbf{A}$  is suppressed near the prompt by the Base cut, just as the case of  $\mathbf{XC}$ . Then, the probability is expressed as,

$$\mathbf{AB} = \begin{cases} 0 & \text{when } 0 \text{ ns} < t < t_{\text{b}} \\ P_{\mathbf{A}}(t) \int_0^{E_{\text{thr}}} P_{\mathbf{B}}(E) dE & \text{when } t > t_{\text{b}} \end{cases} \quad (\text{B.14})$$

The probability is usually larger than the one in the  $\mathbf{XC}$  case, where the probability of the accidental is so small from the beginning. If the boundary of the Base cut is set above the energy threshold  $E_{\text{thr}}$ , the distortion of the time spectrum is avoided. But in this case, the measured energy is deviated by the prompt signal.

### B.2.3 Contamination of Pile-up Events

The overlapped event is assumed to be eliminated by the pile-up cut in the above discussion. But practically, the pile-up cuts have dependency on the energy of the accidental  $\gamma$ -ray. In addition, the completely overlapped events are not rejected by the pile-up cuts. Thus, the effect of the pile-up cuts is restricted as shown in Fig. B.5. The allowed region can be divided into three typical regions.

1. The overlapped signal is so small that the Narrow-Wide cut cannot reject the event. The energy of the incident  $\gamma$ -ray is deviated by the cut margin at most, which is 15 keV for Ge and 30 keV for YAP.
2. The two signals are completely overlapped and the Narrow-Wide cut cannot distinguish these signals. The energy is largely deviated by the overlapped  $\gamma$ -ray.
3. The preceding signal is so small that the Base cut cannot reject the event. Especially near the prompt peak, the energy deviation and the cut efficiency must be closely looked at.

The probability of the contamination is obtained as an integral over the allowed region. When  $\mathbf{X}$  and  $\mathbf{C}$  are overlapped, there are two cases according to the leading signal.

$$\mathbf{XC} = P_{\mathbf{X}}(t) \times \int_0^{\infty} d(\Delta E) \int_{-t_b}^{t_{nw}} d(\Delta t) P_{\mathbf{C}}(t + \Delta t) \text{Cont}(\Delta t, \Delta E) \quad (\text{B.15})$$

$$\mathbf{CX} = P_{\mathbf{C}}(t) \times \int_0^{\infty} d(\Delta E) \int_{-t_b}^{t_{nw}} d(\Delta t) P_{\mathbf{X}}(t + \Delta t) \text{Cont}(\Delta t, \Delta E) \quad (\text{B.16})$$

where the detection time is the timing of the leading signal  $\mathbf{X}$  and  $\mathbf{C}$  respectively. The measured energy is a sum of the leading signal's energy  $E$  and a part of the pile-up signal's energy  $\Delta E$ .

## B.3 Time Spectrums of $\gamma$ -ray Detectors

### B.3.1 The Case of Ge Detector

**suppression factor  $S(t)$**

Since  $t_b$  is a scale of the detector signal, the value reaches several  $\mu s$  in the case of Ge detector. On the other hand,  $t_{nw}$  is determined by the width of Wide gate, which is 40  $\mu s$  for Ge detector. Thus, the probability of the accidental events around the trigger does not affect the time dependency of the suppression factor. Only the difference of the probability before and after the trigger, which is the probability of the accidental events without anti-trigger hit, determines the time dependence. Thus, the suppression factor  $S(t)$  for Ge detector is expressed as

$$S(t) \propto \begin{cases} \exp(R_{\text{without}} \cdot t) & \text{when } t < \text{several } \mu s \\ \exp((R_{\text{with}} + R_{\text{without}}) \cdot t) & \text{when } t > \text{several } \mu s \end{cases} \quad (\text{B.17})$$

where  $R_{\text{with}}$  and  $R_{\text{without}}$  are the detector hit rate of the event with and without anti-trigger hit. They are approximately half of the total hit rate.

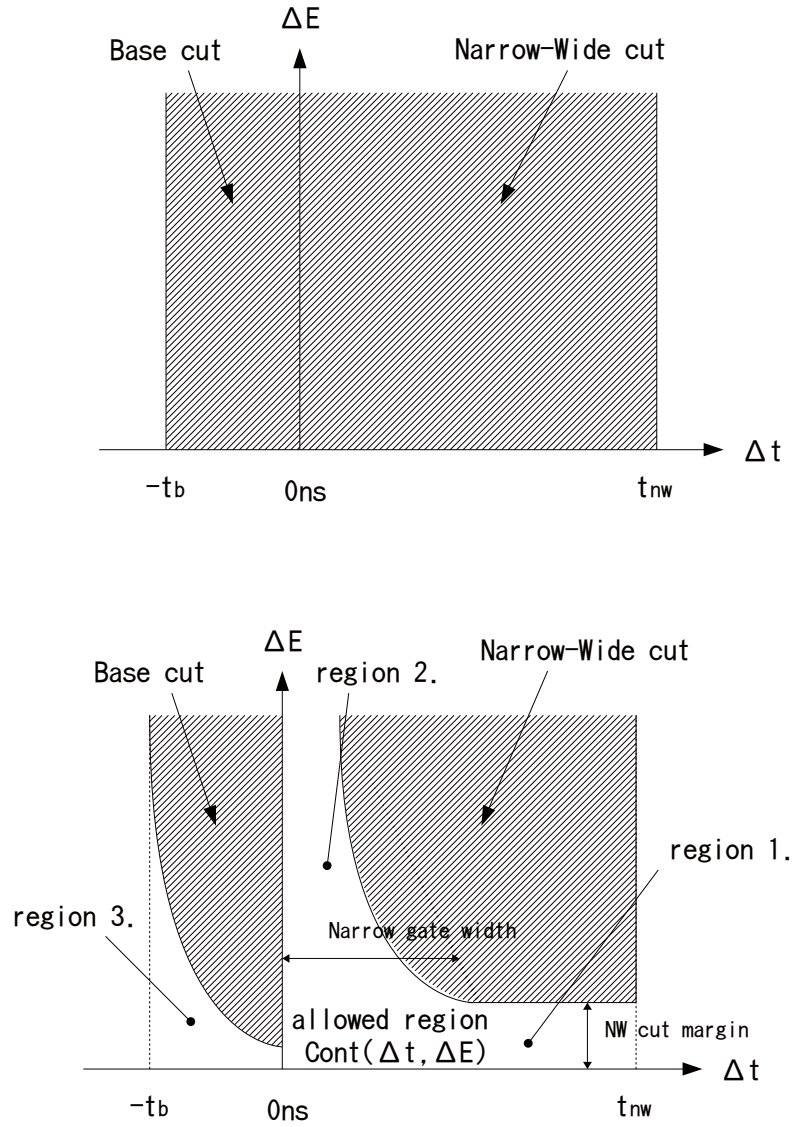


Figure B.4: Suppression region of the pile-up cuts. The upper figure shows the suppression region when the pile-up cuts are assumed to be perfect.  $\Delta E$  and  $\Delta t$  are the energy of the accidental signal and the time interval from the incident signal. The lower figure shows the suppression region in considering the energy dependence of the pile-up cuts. In this case, some regions are allowed.

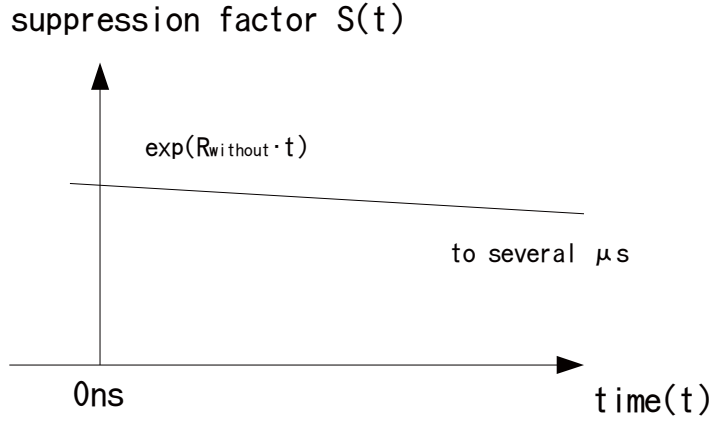


Figure B.5: Suppression factor  $S(t)$  for Ge detector. The events in the later region are suppressed through the first hit condition.

#### other factors

The time dependent deviation of the intrinsic time spectrum is not a problem for Ge detector, since only the ratio of  $2\gamma$  and  $3\gamma$  is important in the analysis. But, the time dependence of the accidental distribution is sensitive through the subtraction of the accidental spectrum. The energy of the accidental event near the prompt is varied by the prompt hit with the probability of about 0.2 %. These tails, which extend to 50 keV threshold energy, is eliminated by the pile-up cut in the later accidental region. Most of the difference is in the region above the counting window 507 keV - 515 keV and does not contribute to the decay rate.

The slow rise-time component of Ge detector plays some role when the accidental events pile up on the event. The event may be not rejected by the SRT cut since the accidental signal provides the fast rise-time of the event. Thus, the number of accidental events is increased by about 1 % near the prompt peak. However, the energies of these events are not localized around the 511 keV peak and widely spreaded over 1 MeV range. Therefore, the effect is considered to be small in the analysis.

The energy deviation by the pile-up of small signals (region 1.) is not time dependent. But, the deviation of the energy spectrum is a problem in calculating the  $2\gamma$  and  $3\gamma$  efficiencies. Therefore, the deviation is measured with the events around the 511 keV peak and incorporated into the response function of the Monte Carlo simulation.

### B.3.2 The Case of YAP Scintillator

suppression factor  $S(t)$

The suppression factor for YAP scintillator is rather complicated by the fast timing characteristics. For YAP scintillator,  $t_b$  is about 200 ns and  $t_{nw}$  is 500 ns. Then, the kink of the suppression factor comes in the delayed region around 100 ns as

$$S(t) \propto \begin{cases} \exp(R_{\text{without}} \cdot t) & \text{when } t < \text{about } 100 \text{ ns} \\ \exp((R_{\text{with}} + R_{\text{without}}) \cdot t) & \text{when } t > \text{about } 100 \text{ ns} \end{cases} \quad (\text{B.18})$$

Practically, the kink is smeared by the energy dependence of  $t_b$  and the sensitivity of the point is less than 10 ppm.

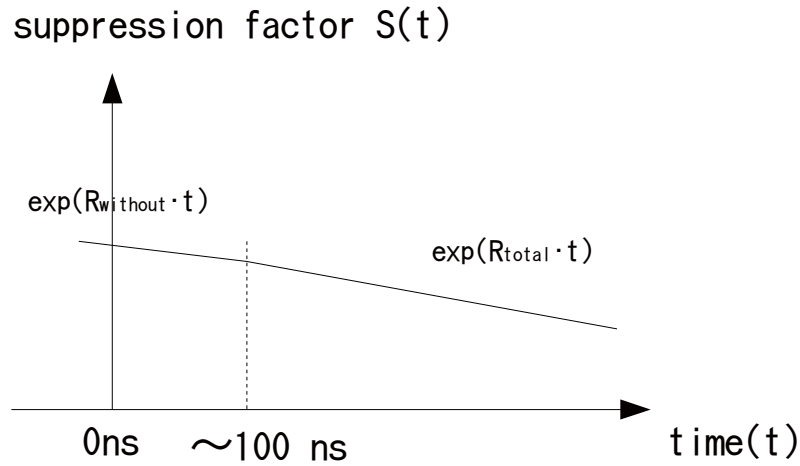


Figure B.6: Suppression factor  $S(t)$  for YAP scintillator. The events in the later region are suppressed by the first hit condition.

#### other factors

The YAP scintillators have fast timing characteristics. Then, the accidental events near the prompt remain if **A** hits the detector after 500 ns or later (special case of **XC**). Otherwise, the events are rejected by the pile-up cuts. The probability that **A** hit the detector after 500 ns is less than 0.1 %. The 0.1 % excess of the accidental events near the prompt does not contribute to the decay rate.

The activities of the prompt events affect the time spectrum near the prompt peak through the Base cut. About 1 % of the accidental events have the prompt hit under the energy threshold. Even for the delayed o-Ps events, the prompt hits under the threshold exist with the probability of about 0.1 %. Most of the contribution is bremsstrahlung of the positron and the contribution of 1077 keV nuclei- $\gamma$  is small due to its tiny emission ratio of 1 %.

To avoid the distortion of the time spectrum, the Base cut condition is set to  $140 \sigma$ , which correspond to the threshold value. Instead of that, the energies of these events are getting larger near the prompt by the energy of the prompt hit. The effect of this energy deviation is roughly estimated as follows. The energy deviation is less than the energy threshold of about 70 keV and the mean value is considered to be around 30 keV. If the energy is increased by 30 keV, the efficiency above the energy boundary 150 keV is increased by about 10 %. Then, the efficiency is considered to shift exponentially with the time constant of about 30 ns, which is the signal shape of YAP scintillator. The Wide gate will cover the whole signal of the prompt hit at  $t = 30 \text{ ns}$ , which is the margin of Wide gate. Finally, It is found that the increase of the events near the prompt contributes to the decay rate by +6 ppm.

The contamination of the completely overlapped event (region 2.) is not so much due to the narrow ADC gates. The probability is less than  $10^{-4}$  of the o-Ps delayed events and about 1 % of the accidental events near the prompt. In addition, the time dependence is considered to be corresponding to the decay rate. Then, these effects do not contribute to the decay rate.

# Bibliography

- [1] G. S. Adkins and F. R. Brown, *Phys. Rev. A* **28**, 1164 (1983).
- [2] T. Matsumoto, M. Chiba, R. Hamatsu, and T. Hirose, *Phys. Rev. A* **54**, 1947 (1996).
- [3] A. H. Al-Ramadhan and D. W. Gidley, *Phys. Rev. Lett.* **72**, 1632 (1994).
- [4] A. Öre and J. L. Powell, *Phys. Rev.* **75**, 1696 (1949).
- [5] W. E. Caswell, G. P. Lepage, and J. Sapirstein, *Phys. Rev. Lett.* **38**, 488 (1977).
- [6] G. S. Adkins, *Ann. Phys. (NY)* **146**, 78 (1983).
- [7] G. S. Adkins, *Phys. Rev. Lett.* **76**, 4903 (1996).
- [8] W. E. Caswell and G. P. Lepage, *Phys. Rev. A* **20**, 36 (1979).
- [9] I. B. Khriplovich and A. S. Yelkhovskiy, *Phys. Lett. B* **246**, 520 (1990).
- [10] A. I. Milstein and I. B. Khriplovich, *JTEP* **79**, 379 (1994).
- [11] S. G. Karshenboim, *JTEP* **76**, 541 (1993).
- [12] S. G. Karshenboim, *Phys. At. Nucl.* **1710**, 1993 (1993).
- [13] B. A. Kniehl and A. A. Penin, hep-ph/0004267, 2000.
- [14] K. Melnikov and A. Yelkhovskiy, hep-ph/0008099, 2000.
- [15] A. P. Burichenko, *Phys. At. Nucl.* **56**, 640 (1993).
- [16] P. Labelle, G. P. Lepage, and U. Magnea, *Phys. Rev. Lett.* **72**, 2006 (1994).
- [17] R. N. Faustov, A. P. Martynenko, and V. A. Saleev, *Phys. Rev. A* **51**, 4520 (1995).

- 
- [18] G. S. Adkins, R. N. Fell, and J. Sapirstein, *Phys. Rev. Lett.* **84**, 5086 (2000).
- [19] G. S. Adkins, R. N. Fell, and J. Sapirstein, *Ann. Phys. (N.Y.)* **295**, 136 (2002).
- [20] S. Asai, S. Orito, and N. Shinohara, *Phys. Lett.* **B357**, 475 (1995).
- [21] S. Asai, *New Measurement of Orthopositronium Lifetime*, Doctoral thesis, 1995, University of Tokyo.
- [22] R. H. Beers and V. W. Hughes, *Am. Phys. Soc.* **13**, 633 (1968).
- [23] D. W. Gidley, K. A. Marko, and A. Rich, *Phys. Rev. Lett.* **36**, 395 (1976).
- [24] D. W. Gidley, P. W. Zitzewitz, K. A. Marko, and A. Rich, *Phys. Rev. Lett.* **37**, 729 (1976).
- [25] D. W. Gidley, A. Rich, P. W. Zitzewitz, and D. A. L. Paul, *Phys. Rev. Lett.* **40**, 737 (1978).
- [26] D. W. Gidley and P. W. Zitzewitz, *Phys. Lett. A* **69**, 97 (1978).
- [27] K. F. Canter et al., *Phys. Lett. A* **65**, 301 (1978).
- [28] T. C. Griffith, G. R. Heyland, K. S. Lines, and T. R. Twomey, *J. Phys. B* **11**, 743 (1978).
- [29] D. W. Gidley, A. Rich, E. Sweetman, and D. West, *Phys. Rev. Lett.* **49**, 525 (1982).
- [30] P. Hashbach, G. Hilbert, E. Klempt, and G. Werth, *Nuovo Cimento* **97A**, 419 (1987).
- [31] C. I. Westbrook, D. W. Gidley, R. S. Conti, and A. Rich, *Phys. Rev. Lett.* **58**, 1328 (1987).
- [32] C. I. Westbrook, *Precision Measurement of the Decay Rate of Orthopositronium*, Ph. D. thesis, 1987, University of Michigan.
- [33] C. I. Westbrook, D. W. Gidley, R. S. Conti, and A. Rich, *Phys. Rev.* **A40**, 5489 (1989).
- [34] J. S. Nico, D. W. Gidley, A. Rich, and P. W. Zitzewitz, *Phys. Rev. Lett.* **65**, 1344 (1990).
- [35] J. S. Nico, *Precision measurement of the orthopositronium decay rate using the vacuum technique*, Ph. D. thesis, 1991, University of Michigan.

- [36] R. S. Vallery, P. W. Zitzewitz, and D. W. Gidley, *Phys. Lett. B* **572**, 117 (2003).
- [37] O. Jinnouchi, S. Asai, and T. Kobayashi, *Phys. Lett. B* **572**, 117 (2003).
- [38] O. Jinnouchi, *Study of Bound State QED : Precision Measurement of the Orthopositronium Decay Rate*, Doctoral thesis, 2001, University of Tokyo.
- [39] W. E. Caswell, G. P. Lepage, and J. Sapirstein, *Phys. Rev. Lett.* **38**, 488 (1977).
- [40] A. Rubbia, *Int. J. Mod. Phys. A* **19**, 3961 (2004).
- [41] Y. Nagashima, T. Hyodo, K. Fujiwara, and A. Ichimura, *J. Phys. B* **31**, 329 (1998).
- [42] Y. Nagashima, M. Kakimoto, T. Hyodo, K. Fujiwara, A. Ichimura, T. Chang, J. Deng, T. Akahane, T. Chiba, K. Suzuki, B. T. A. McKee, and A. T. Stewart, *Phys. Rev. A* **52**, 258 (1995).
- [43] J. Allison et al., *IEEE Transactions on Nuclear Science* **53 No.1**, 270 (2006).
- [44] M. Charlton, *Rep. Prog. Phys.* **48**, 737 (1985).
- [45] F. W. Bell Inc., *BELL 610 GAUSSMETER User's Manual*.
- [46] S. Berko and H.N. Pendleton, *Ann. Rev. Nucl. Part. Sci.* **30**, 543 (1980).
- [47] Nippon Aerosil Co. Ltd., The basic characteristics of AEROSIL, Aerosil technical report No.17.
- [48] R. B. Firestone and V. S. Shirley, *Table of Isotopes [8th Edition]*, John Wiley & Sons, Inc., 1999.
- [49] S. Baccaro, A. Cecilia, M. Montecchi, T. Malatesta, F. de Notaristefani, S. Torrioli, F. Vittori, *Nucl. Instr. and Meth. A* **406**, 479 (1998).
- [50] N. Tsuchida, M. Ikeda, T. Kamae, M. Kokubun, *Nucl. Instr. and Meth. A* **385**, 290 (1997).
- [51] Rene Brun and Fons Rademakers, ROOT - An Object Oriented Data Analysis Framework, Proceedings AIHENP'96 Workshop, Lausanne, Sep. 1996, *Nucl. Inst. Meth. in Phys. Res. A* **389** (1997) 81-86. See also <http://root.cern.ch/> .
- [52] S. Agostinelli et al., *Nuclear Instruments and Methods A* **506**, 250 (2003).

- 
- [53] R. M. Kippen, *New Astronomy Reviews* **48**, 221 (2004).
- [54] S. Y. F. Chu, L. P. Ekström, R. B. Firestone, WWW Table of Radioactive Isotopes.
- [55] J. Mantel, *Int. J. appl. Radiat. Isotopes* **23**, 407 (1972).
- [56] IT/ASD CERN, *CERN Program Library Short writeups*, (1996).
- [57] IT/ASD CERN, *MINUIT Function Minimization and Error Analysis, version 94.1*, (1998), D506 CERN Program Library.
- [58] S. Hatamian, R. S. Conti, and A. Rich, *Phys. Rev. Lett.* **58**, 1833 (1987).
- [59] D. C. Schoepf, S. Berko, K. F. Canter, and P. Sferlazzo, *Phys. Rev. A* **45**, 1407 (1992).
- [60] L. I. Schiff, *Quantum Mechanics*, McGraw-Hill, New York, 1949.
- [61] Keyence Corp., *SK-030, SK-200*.
- [62] Arthur Rich, *Phys. Rev. Lett.* **34**, 127 (1975).
- [63] E. M. Purcell, *Electricity and Magnetism 2nd edition, Berkley Physics Course. Volume 2*, McGraw-Hill, Inc. New York.